

Abstract

Measurement of (π^- -Ar) and (K^+ -Ar) total hadronic cross sections in the LArIAT experiment

Elena Gramellini

2018

6 Abstract goes here. Limit 750 words.

7 **Measurement of (π^- -Ar) and (K^+ -Ar)**

8 **total hadronic cross sections in the**

9 **LArIAT experiment**

10 A Dissertation
11 Presented to the Faculty of the Graduate School
12 of
13 Yale University
14 in Candidacy for the Degree of
15 Doctor of Philosophy

16 by
17 Elena Gramellini

18 Dissertation Director: Bonnie T. Fleming

19 Date you'll receive your degree

²⁰

Copyright © 2018 by Elena Gramellini

²¹

All rights reserved.

22

A mia mamma e mio babbo,

23

grazie per le radici e grazie per le ali.

24

To my mom and dad,

25

thank you for the roots and thank you for the wings.

²⁶ Contents

²⁷	Acknowledgements	viii
²⁸	Introduction	ix
²⁹	1 The theoretical framework	1
³⁰	1.1 The Standard Model	1
³¹	1.2 Neutrinos: tiny cracks in the Standard Model	4
³²	1.2.1 Neutrinos in the Standard Model	4
³³	1.2.2 Neutrino Oscillations	6
³⁴	1.2.3 Make up of Neutrino Interactions	7
³⁵	1.3 Beyond the Standard Model	9
³⁶	1.3.1 Open Questions in Neutrino Physics	11
³⁷	1.3.2 Towards a more fundamental theory: GUTs	15
³⁸	1.4 Motivations for Hadronic Cross Sections in Argon	18
³⁹	1.4.1 Pion-Argon Total Hadronic Cross Section	18
⁴⁰	1.4.2 Kaon-Argon Total Hadronic Cross Section	29
⁴¹	2 Liquid Argon Detectors at the Intensity Frontier	34
⁴²	2.1 The Liquid Argon Time Projection Chamber Technology	34
⁴³	2.1.1 TPCs, Neutrinos & Argon	35
⁴⁴	2.1.2 LArTPC: Principles of Operation	37

45	2.1.3	Liquid Argon: Ionization Charge	40
46	2.1.4	Liquid Argon: Scintillation Light	45
47	2.1.5	Signal Processing and Event Reconstruction	49
48	2.2	The Intensity Frontier Program	53
49	2.2.1	Prospects for LArTPCs in Neutrino Physics: SBN and DUNE	54
50	2.2.2	Prospects for LArTPCs in GUT Physics: DUNE	55
51	2.2.3	Enabling the next generation of discoveries: LArIAT	57
52	3	LArIAT: Liquid Argon In A Testbeam	60
53	3.1	The Particles' Path to LArIAT	60
54	3.2	LArIAT Tertiary Beam Instrumentation	62
55	3.2.1	Bending Magnets	63
56	3.2.2	Multi-Wire Proportional Chambers	65
57	3.2.3	Time-of-Flight System	67
58	3.2.4	Punch-Through and Muon Range Stack Instruments	68
59	3.2.5	LArIAT Cosmic Ray Paddle Detectors	70
60	3.3	In the Cryostat	71
61	3.3.1	Cryogenics and Argon Purity	71
62	3.3.2	LArTPC: Charge Collection	74
63	3.3.3	LArTPC: Light Collection System	77
64	3.4	Trigger and DAQ	80
65	3.5	Control Systems	81
66	4	Total Hadronic Cross Section Measurement Methodology	87
67	4.1	Event Selection	88
68	4.1.1	Selection of Beamline Events	88
69	4.1.2	Particle Identification in the Beamline	89
70	4.1.3	TPC Selection: Halo Mitigation	89

71	4.1.4	TPC Selection: Shower Removal	90
72	4.2	Beamline and TPC Handshake: the Wire Chamber to TPC Match . .	91
73	4.3	The Thin Slice Method	93
74	4.3.1	Cross Sections on Thin Target	93
75	4.3.2	Not-so-Thin Target: Slicing the Argon	94
76	4.3.3	Corrections to the Raw Cross Section	96
77	4.4	Procedure testing with truth quantities	97
78	5	Data and MC preparation for the Cross Section Measurements	100
79	5.1	Cross Section Analyses Data Sets	100
80	5.2	Construction of a Monte Carlo Simulation for LArIAT	102
81	5.2.1	G4Beamline	102
82	5.2.2	Data Driven MC	107
83	5.3	Estimate of Backgrounds in the Pion Cross Section	110
84	5.3.1	Background from Pion Capture and Decay	110
85	5.3.2	Contributions from the Beamline Background	113
86	5.4	Estimate of Energy Loss before the TPC	116
87	5.5	Tracking Studies	120
88	5.5.1	Angular Resolution	120
89	5.6	Calorimetry Studies	126
90	5.6.1	Kinetic Energy Measurement	126
91	6	Negative Pion Cross Section Measurement	129
92	6.1	Raw Cross Section	129
93	6.1.1	Statistical Uncertainty	131
94	6.1.2	Treatment of Systematics	133
95	6.2	Corrections to the Raw Cross Section	134
96	6.2.1	Background subtraction	134

97	6.2.2 Efficiency Correction	137
98	6.3 Results	141
99	7 Positive Kaon Cross Section Measurement	143
100	7.1 Raw Cross Section	143
101	7.2 Corrections to the Raw Cross Section	145
102	7.3 Results	147
103	8 Conclusions	150
104	A Measurement of LArIAT Electric Field	152
105	B Additional Tracking Studies for LArIAT Cross Section Analyses	160
106	B.0.1 Study of WC to TPC Match	161
107	B.0.2 Tracking Optimization	163
108	C Energy Calibration	166

¹⁰⁹ Acknowledgements

¹¹⁰ “*Dunque io ringrazio tutti quanti.*

¹¹¹ *Specie la mia mamma che mi ha fatto così funky.”*

¹¹² – Articolo 31, Tanqi Funky, 1996 –

¹¹³ “*At last, I thank everyone.*

¹¹⁴ *Especiallly my mom who made me so funky.”*

¹¹⁵ – Articolo 31, Tanqi Funky, 1996 –

¹¹⁶ A lot of people are awesome, especially you, since you probably agreed to read
¹¹⁷ this when it was a draft.

¹¹⁸ ‘

¹¹⁹ Introduction

¹²⁰ This thesis work concerns the first measurement of the (π^- -Ar) total hadronic cross
¹²¹ section in the 100-1000 MeV kinetic energy range and the first measurement of the
¹²² (K^+ -Ar) total hadronic cross section in the 100-650 MeV kinetic energy range. We
¹²³ performed these measurements at the LArIAT experiment, a small (0.25 ton) Liquid
¹²⁴ Argon Time Projection Chamber (LArTPC) on a beam of charged particles at the
¹²⁵ Fermilab Test Beam Facility. Albeit particle and nuclear physics have a long history
¹²⁶ of hadronic cross section measurements, the work outlined in this thesis presents a
¹²⁷ new methodology – the “thin slice method” – for cross section measurements in argon,
¹²⁸ possible only thanks to the detection capabilities of the LArTPC technology. The
¹²⁹ combination of fine-grained tracking and excellent calorimetric information provided
¹³⁰ by the LArTPC technology allows to see unprecedented details of particle interactions
¹³¹ in argon and, in LArIAT, to measure the kinetic energy of a hadron at each step
¹³² of the tracking. A renewed interest for precision measurements of hadronic cross
¹³³ sections, particularly in argon, arises from the current panorama of experimental
¹³⁴ particle physics at the intensity frontier.

¹³⁵ The discovery of the Higgs boson in 2012 marked the triumph of the Standard
¹³⁶ Model of Particle Physics; exploring what lays beyond is the real challenge in our field
¹³⁷ today. Since their formulation in 1930, neutrinos have been a source of surprises (and
¹³⁸ Nobel Prizes) for particle physicists, tiny cracks in our understanding of Nature. In
¹³⁹ particular, the discovery of neutrino oscillation represents the first evidence of physics

140 Beyond the Standard Model (BSM). From a theoretical point of view, the field is
141 developing new theories to account for the small but non-zero mass of neutrinos,
142 while trying to remain consistent with the rest of the Standard Model. From an
143 experimental point of view, we are developing technologies and huge collaborations
144 to probe these theories. As we enter the era of precision measurements of neutrino
145 interaction, neutrinos might hold the key to the next generation of discoveries in
146 particle physics.

147 Experimentally, precision measurements can be achieved only if the detector tech-
148 nology is able to resolve the fine details of a neutrino interaction and to record a
149 statistically relevant number of neutrinos. With “fine details” here we mean the abil-
150 ity to distinguish the many products of the neutrino interaction, such as protons,
151 pions, muons and electrons, and to measure their energy. Historically, bubble cham-
152 ber neutrino detectors were the first revolution in neutrino detection: for example,
153 the spatial resolution of Gargamelle allowed the discovery of neutrino neutral current
154 interaction. Despite the high precision of bubble chambers images, this technology
155 is hard to scale to massive size, making statistical analyses on neutrino interactions
156 almost impossible to perform. To make up for the small neutrino interaction cross
157 section, neutrino experiments moved to very large size, at the expenses of spatial
158 precision. This is the case for the detectors which discovered neutrino oscillation:
159 both Super-Kamiokande and SNO are massive Cherenkov detectors. With LArT-
160 PCs, the field is gaining again bubble-chamber like precision but at massive scales.
161 Following the recommendations of the latest Particle Physics Project Prioritization
162 Panel [106], the US particle physics panorama is directing a substantial effort to-
163 wards the exploration of the intensity frontier through the construction of massive
164 LArTPCs. In particular, the near future will see the development of a Short Baseline
165 Neutrino Program (SBN) and long baseline neutrino program (DUNE), both based
166 on the LArTPC detector technology. The US liquid argon program has the potential

167 to answer many of the fundamental open questions in particle physics today, such
168 as: is there a fourth generation neutrino? is CP violated in the lepton sector? are
169 there any additional symmetries? and, can we find an indication of Grand Unified
170 Theories?

171 The SBN program at Fermilab is tasked with conclusively addressing the existence
172 of a fourth neutrino generation in the $\Delta m^2 = \Delta m_{14}^2 \sim [0.1 - 10] \text{ eV}^2$ parameter space.
173 The SBN program entails three surface LArTPCs positioned on the Booster Neutrino
174 Beam at different distances from the neutrino production in oder to fully exploit the
175 L/E dependence of the oscillation pattern: SBND (100 m from the decay pipe),
176 MicroBooNE (450 m), and ICARUS (600 m). SBN will also perform an extensive
177 program of neutrino cross section measurements, fundamental to abate systematics
178 in the oscillation analyses in both SBN and DUNE.

179 DUNE has a vast neutrino and non-accelerator physics reach. For what it concerns
180 neutrino physics, oscillation analyses in DUNE have the capability of solving the mass
181 hierarchy and octant problem, and discovering CP violation in the neutrino sector.
182 Besides its neutrino program, DUNE can open an experimental window on Grand
183 Unified Theories (GUTs). GUTs could potentially answer fundamental questions
184 such as the existence of non-zero neutrino masses and matter-antimatter asymmetry,
185 explaining some “accidents” in the Standard Models, such as the exact cancellation of
186 the proton and the electron charge. Directly probing GUTs at the unification energy
187 scale is impossible by any foreseeable collider experiment. We then need an indirect
188 proof such as baryon number violation, which is predicted by almost every GUT in the
189 form of proton decay, bounded nucleon decay or $n - \bar{n}$ oscillations on long time-scales.
190 Historically, the main technology used in these searches has been water Cherenkov
191 detectors, with Super-Kamiokande setting all the current experimental limits on the
192 decay lifetimes at the order of $\sim 10^{34}$ years. The DUNE far detector and its non-
193 accelerator physics program is a interesting new actor on this stage. LArTPCs can in

194 fact complement nucleon decay searches in modes where water Cherenkov detectors
195 are less sensitive, especially $p \rightarrow K^+ \bar{\nu}$ [11].

196 Such a diverse physics program speaks to the versatility of the LArTPC technol-
197 ogy. LArTPCs provide excellent electron/photon separation [9] lacking in Cherenkov
198 detectors which can be leveraged to abate the photon background from neutral cur-
199 rent interactions in ν_e searches. LArTPCs also share superb tracking capability with
200 bubble chamber detectors, with several additional benefits. They are electronically
201 read out and self triggered detectors; they provide full 3D-imaging with millimeter
202 resolution, precise calorimetric reconstruction and excellent particle identification.

203 The amount of information a LArTPC can provide makes these detectors rather
204 complex: a series of dedicated measurements is necessary to obtain meaningful physics
205 results from a LArTPC. The complexity of the LArTPC technology for neutrino
206 detection is due to several reasons. Argon is a fairly heavy element, which means that
207 nuclear effects play an important role in the looks of the interaction topology. For
208 example, pions are one of the main products of neutrino interactions; yet, since data
209 on charged particle interaction in argon is scarce, neutrino event generators have big
210 uncertainties in the re-scattering simulation of pion in argon. The amount of details
211 in an LArTPC event is easily parsed by human eye, but can make automatic event
212 reconstruction rather challenging. Thus, reconstruction algorithms in LArTPC need
213 to be tune to recognize the different topologies of the neutrino interaction products in
214 argon. This is particularly true for pions, since they are an abundant product of the
215 neutrino interactions: the occurrence of a pion interaction in argon can modify the
216 topology of the neutrino event, causing a misidentification of the neutrino interaction.

217 The LArIAT [38] experiment is performing precise cross section measurements of
218 charged particles in argon to bridge this gap of knowledge. The LArIAT LArTPC sits
219 on a beam of charged particles at the Fermilab Test Beam Facility which provides
220 charge particles of the type and energy range relevant for neutrino interaction of

221 both SBN and DUNE. The (π^- -Ar) hadronic cross section is a fundamental input for
222 neutrino detectors in liquid argon, as pion interactions can modify the topology and
223 energy reconstruction of neutrino events in the GeV range, where pion production
224 is abundant. The (K^+ -Ar) total hadronic differential cross section in LArIAT is
225 particularly relevant for a high identification efficiency in the context of proton decay
226 searches in DUNE in the $p \rightarrow K^+ \bar{\nu}$ channel. In fact, the kaon-argon cross section
227 affects the kaon topology by modifying the kaon tracking and energy reconstruction,
228 impacting the basis for kaon identification in a LArTPC.

229 The cross section analyses exploit the totality of LArIAT’s experimental handles;
230 they rely on beam line detector information as well as both calorimetry and tracking
231 in the TPC. These analyses are LArIAT’s first physics results. In order to measure
232 total hadronic argon cross sections, several steps are necessary. The analyses start by
233 identifying a sample of the hadron of interest in the beam line and assessing the beam
234 line contaminations. It proceeds with tracking the hadron candidates in the TPC and
235 measuring their kinetic energy at each point in the tracking: the fine sampling of an
236 hadron in the TPC forms the set of “incident” hadrons. Then, the hadronic interac-
237 tion point is identified and the raw cross section is calculated. Two corrections are
238 then applied to the raw cross section – a background subtraction and a correction
239 for detector effects – to obtain the true cross section measurement.

240

241 This body of work is organized in 8 chapters. We provide a description of the
242 theoretical framework for the measurements in Chapter 1. Chapter 2 outlines the
243 LArTPC detector technology, while Chapter 3 describes LArIAT experimental setup.
244 We present the event selection for both the pion and kaon analyses, as well as the
245 “thin slice method” in Chapter 4. Chapter 5 describes the work done on the data
246 and Monte Carlo samples in preparation of the cross section analyses. Chapter 6
247 shows the results for the (π^- -Ar) total hadronic cross section measurement. Chapter

248 7 shows the results for the (K^+ -Ar) total hadronic cross section measurement. We
249 draw the final remarks on this work in Chapter 8

250 A series of additional studies and calibrations were necessary to perform the cross
251 section analyses. Appendix A shows a measurement of the LArIAT LArTPC electric
252 field using cosmic data. Appendix B shows an optimization of the tracking algorithms
253 geared towards maximizing the efficiency of finding the hadronic interaction point.
254 Appendix C shows the calorimetry calibration of the LArIAT LArTPC, which is a
255 pivotal measurement to enable any physics analysis with TPC data.

256 **Chapter 1**

257 **The theoretical framework**



258

– J. S. Bach, 1720 ca. –

259 In this chapter, we set the (π^- - Ar) and (K^+ - Ar) total hadronic cross section
260 measurements into the greater theoretical and phenomenological framework. We start
261 by briefly describing the Standard Model (Section 1.1), with particular attention to
262 neutrinos and neutrino interactions (Section 1.2). We then describe some of the
263 open questions in neutrino physics today and Beyond Standard Model theories (1.3)
264 setting the stage for the measurements reported in this work (Section 1.4).

265 **1.1 The Standard Model**

266 The Standard Model (SM) of particle physics is the most accurate theoretical descrip-
267 tion of the subatomic world and, in general, one of the most precisely tested theories
268 in the history of physics. The SM describes the strong, electromagnetic and weak
269 interactions among elementary particles in the framework of quantum field theory,

270 accounting for the unification of electromagnetic and weak interactions for energies
271 above the vacuum expectation value (VEV) of the Higgs field. The SM does not
272 describe gravity or general relativity.

273 The Standard Model is a gauge theory based on the local symmetry group

$$G_{SM} = SU(3)_C \otimes SU(2)_L \otimes U(1)_Y \quad (1.1)$$

274 where the subscripts C indicates the conserved strong charge (color), and the
275 subscripts Y indicates the conserved hypercharge. If we indicated with T the weak
276 isospin T and with T3 its third component, hypercharge can be related to the electric
277 charge Q through the Gell-Mann-Nishijima relation:

$$Q = \frac{Y}{2} + T_3. \quad (1.2)$$

278 In the quantum field framework, the SM fields correspond to the irreducible rep-
279 resentations of the G_{SM} symmetry group. In particular, the particles are divided in
280 two categories, fermions and bosons, according to their spin-statistics. Described by
281 the Fermi-Dirac statistics, fermions have half-integer spin and are sometimes called
282 “matter-particles”. Bosons or “force carriers” have integer spin, follow the Bose-
283 Einstein statistics and mediate the interaction between fermions. The fundamental
284 fermions and their quantum numbers are listed in Tab 1.1.

285 Quarks can interact via all three the fundamental forces; they are triplets of
286 $SU(3)_C$, that is they can exist in three different colors. If one chooses a base where
287 u , c and t quarks are simultaneously eigenstates of both the strong and the weak
288 interactions, the remaining eigenstates are usually written as d , s and b for the strong
289 interaction and d' , s' and b' for the weak interaction, because the latter ones are
290 the result of a CKM rotation on the first ones. Charged leptons interact via the
291 weak and the electromagnetic forces, while neutrinos only interact via the weak force.

Generation	I	II	III	T	Y	Q
Leptons	$\begin{pmatrix} \nu_e \\ e \end{pmatrix}_L$	$\begin{pmatrix} \nu_\mu \\ \mu \end{pmatrix}_L$	$\begin{pmatrix} \nu_\tau \\ \tau \end{pmatrix}_L$	1/2 -1/2	-1 -1	0 -1
	e_R	μ_R	τ_R	0	-2	1
Quarks	$\begin{pmatrix} u \\ d' \end{pmatrix}_L$	$\begin{pmatrix} c \\ s' \end{pmatrix}_L$	$\begin{pmatrix} t \\ b' \end{pmatrix}_L$	1/2 -1/2	1/3 1/3	2/3 -1/3
	u_R d'_R	c_R s'_R	t_R b'_R	0 0	4/3 -2/3	2/3 -1/3

Table 1.1: SM elementary fermionic fields. The subscripts L and R indicate respectively the negative chirality (left-handed) and the positive chirality (right-handed).

292 The gauge group univocally determines the number of gauge bosons that carry the
 293 interaction; the gauge bosons correspond to the generators of the group: eight gluons
 294 (g) for the strong interaction, one photon (γ) and three bosons (W^\pm , Z^0) for the
 295 electroweak interaction. A gauge theory by itself cannot provide a description of
 296 massive particles, but it is experimentally well known that most of the elementary
 297 particles have non-zero masses. The introduction of massive fields in the Standard
 298 Model lagrangian would make the theory not gauge invariant, resulting ill-defined.
 299 This problem is solved in the SM by the introduction of a scalar iso-doublet $\Phi(x)$, the
 300 Higgs field, which gives mass to W^\pm and Z^0 gauge bosons through the electroweak
 301 symmetry breaking mechanism and to the fermions through Yukawa coupling [75, 76].
 302 The discovery of the Higgs boson in 2012 by the LHC experiments [41, 42] marked
 303 the ultimate confirmation of a long history of successful predictions by the SM.

304 1.2 Neutrinos: tiny cracks in the Standard Model

305 To our current knowledge, neutrinos are the most abundant fermion in the Universe.
306 And yet, they are maybe the most mysterious particle in the SM: they generate
307 theoretical puzzles and experimental challenges. In this section, we treat neutrinos
308 within and beyond the SM and describe the make up of their interaction with matter.

309 1.2.1 Neutrinos in the Standard Model

310 Neutrino can be introduced in the SM as left-handed massless Weyl spinors. The
311 Dirac equation of motion for a free field

$$(i\gamma^\mu \partial_\mu - m)\psi = 0 \quad (1.3)$$

312 for a fermionic field

$$\psi = \psi_L + \psi_R \quad (1.4)$$

313 is equivalent to the equations

$$i\gamma^\mu \partial_\mu \psi_L = m\psi_R \quad (1.5)$$

314

$$i\gamma^\mu \partial_\mu \psi_R = m\psi_L \quad (1.6)$$

315 for the chiral fields ψ_R and ψ_L , whose evolution in space and time is coupled
316 through the mass m . If the fermion is massless, the chiral fields decouple and the
317 fermion can be described by a single Weyl spinor with two independent compo-
318 nents [116]. Pauli initially rejected the description of a physical particle through
319 a single Weyl spinor because of its implication of parity violation. In fact, since
320 the spatial inversion operator throws $\psi_R \leftrightarrow \psi_L$, parity is conserved only if both chi-
321 ral components exist at the same time. For the neutrino introduction in the SM,
322 experiments came in help of the theoretical description. The constraint of parity

³²³ conservation weakened after Wu's experiment in 1957 [119]. Additionally, there was
³²⁴ no experimental indication for massive neutrinos, nor evidence of interaction via the
³²⁵ neutrino right-handed component.

³²⁶ The symmetry group $SU(2)_L \otimes U(1)_Y$ is the only group relevant for neutrino
³²⁷ interactions. The SM electroweak lagrangian is the most general renormalizable la-
³²⁸ grangian invariant under the local symmetry group $SU(2)_L \otimes U(1)_Y$. The lagrangian
³²⁹ couples the weak isotopic spin doublets and singlets described in Table 1.1 with the
³³⁰ gauge bosons A_a^μ ($a = 1, 2, 3$) and B^μ , and Higgs doublet $\Phi(x)$:

$$\begin{aligned} \mathcal{L} = & i \sum_{\alpha=e,\mu,\tau} \bar{L}'_{\alpha L} \not{D} L'_{\alpha L} + i \sum_{\alpha=1,2,3} \bar{Q}'_{\alpha L} \not{D} Q'_{\alpha L} \\ & + i \sum_{\alpha=e,\mu,\tau} \bar{l}'_{\alpha R} \not{D} l'_{\alpha R} + i \sum_{\alpha=d,s,b} \bar{q}'^D_{\alpha R} \not{D} q'^D_{\alpha R} + i \sum_{\alpha=u,c,t} \bar{q}'^U_{\alpha R} \not{D} q'^U_{\alpha R} \\ & - \frac{1}{4} A_{\mu\nu} A^{\mu\nu} - \frac{1}{4} B_{\mu\nu} B^{\mu\nu} \\ & + (D_\rho \Phi)^\dagger (D^\rho \Phi) - \mu^2 \Phi^\dagger \Phi - \lambda (\Phi^\dagger \Phi)^2 \\ & - \sum_{\alpha,\beta=e,\mu,\tau} \left(Y_{\alpha\beta}^l \bar{L}'_{\alpha L} \Phi l'_{\beta R} + Y_{\alpha\beta}^{l*} \bar{l}'_{\beta R} \Phi^\dagger L'_{\alpha L} \right) \\ & - \sum_{\alpha=1,2,3} \sum_{\beta=d,s,b} \left(Y_{\alpha\beta}^D \bar{Q}'_{\alpha L} \Phi q'^D_{\beta R} + Y_{\alpha\beta}^{D*} \bar{q}'^D_{\beta R} \Phi^\dagger Q'_{\alpha L} \right) \\ & - \sum_{\alpha=1,2,3} \sum_{\beta=u,c,t} \left(Y_{\alpha\beta}^U \bar{Q}'_{\alpha L} \tilde{\Phi} q'^U_{\beta R} + Y_{\alpha\beta}^{U*} \bar{q}'^U_{\beta R} \tilde{\Phi}^\dagger Q'_{\alpha L} \right). \end{aligned} \quad (1.7)$$

³³¹ The first two lines of the lagrangian summarize the kinetic terms for the fermionic
³³² fields and their coupling to the gauge bosons $A_a^{\mu\nu}$, $B^{\mu\nu}$ ¹. The third line describes
³³³ the kinetic terms and the self-coupling terms of the gauge bosons. The forth line is
³³⁴ the Higgs lagrangian, which results in the spontaneous symmetry breaking. The last
³³⁵ three lines describe the Yukawa coupling between fermions and the Higgs field, origin
³³⁶ of the fermions' mass.

1. In gauge theories the ordinary derivative ∂_μ is substituted with the covariant derivative D_μ . Here $D_\mu = \partial_\mu + igA_\mu \cdot I + ig'B_\mu \frac{Y}{2}$, where I and Y are the $SU(2)_L$ and $U(1)_Y$ generators, respectively.

337 The coupling between left-handed and right-handed field generates the mass term
338 for fermions. The SM assumes only left-handed components for neutrinos, thus im-
339 plying zero neutrino mass. Since any linear combination of massless fields results in a
340 massless field, the flavor eigenstates are identical to the mass eigenstates in the SM.

341 1.2.2 Neutrino Oscillations

342 The determination of the flavor of a neutrino dynamically arises from the correspond-
343 ing charged lepton associated in a change current interaction; for example, a ν_e is a
344 neutrino which produces an e^- , a $\bar{\nu}_\mu$ is a neutrino which produces a μ^+ , etc. The
345 neutrino flavor eigenstates $|\nu_\alpha\rangle$, with $\alpha = e, \mu, \tau$, are orthogonal to each other and
346 form a base for the weak interaction matrix.

347 Overwhelming experimental data show that neutrinos change flavor during their
348 propagation [101]. This phenomenon, called “neutrino oscillations”, was predicted
349 first by Bruno Pontecorvo in 1957 [102]. Neutrino oscillations are possible only if
350 the neutrino flavor eigenstate are not identical to the mass eigenstates. Thus, the
351 observation of neutrino oscillation results in the first evidence of physics beyond the
352 Standard Model. A minimal extension of the SM introduces three mass eigenstates,
353 $|\nu_i\rangle$ ($i = 1, 2, 3$), whose mass m_i is well defined. The unitary Pontecorvo-Maki-
354 Nakagawa-Sakata matrix transforms the mass base into the flavor base as follows

$$|\nu_\alpha\rangle = U_{PMNS} |\nu_i\rangle, \quad (1.8)$$

355 with

$$U_{PMNS} = \begin{bmatrix} c_{12} & s_{12} & 0 \\ -s_{12} & c_{12} & 0 \\ 0 & 0 & 1 \end{bmatrix} \begin{bmatrix} c_{13} & 0 & s_{13}e^{-i\delta} \\ 0 & 1 & 0 \\ -s_{13}e^{-i\delta} & 0 & c_{13} \end{bmatrix} \begin{bmatrix} 1 & 0 & 0 \\ 0 & c_{23} & s_{23} \\ 0 & -s_{23} & c_{23} \end{bmatrix} \begin{bmatrix} e^{i\alpha_1} & 0 & 0 \\ 0 & e^{i\alpha_2} & 0 \\ 0 & 0 & 1 \end{bmatrix} \quad (1.9)$$

356 where c e s stand respectively for cosine and sine of the corresponding mixing
 357 angles (θ_{12} , θ_{23} and θ_{13}), δ is the Dirac CP violation phase, α_1 and α_2 are the eventual
 358 Majorana CP violation phases. Experimental results on neutrino oscillations are
 359 generally reported in terms of the mixing angles and of the squared mass splitting
 360 $\Delta m_{ab}^2 = m_a^2 - m_b^2$, where a and b represent the mass eigenstates. A summary of the
 361 current status of experimental results, albeit partial, is given in table 1.2.

Table 1.2: Summary of experimental results on neutrino oscillation parameters. **ADD CITATIONS**

	Value	Precision	Experiment
θ_{23}	45°	9.0%	Super Kamiokande, MINOS,
$-\Delta m_{32}^2$	$2.5 \cdot 10^{-3} \text{ eV}^2$	1.8%	Nova, MACRO
θ_{12}	34°	5.8%	SNO, Gallex,
$-\Delta m_{12}^2$	$7.4 \cdot 10^{-5} \text{ eV}^2$	2.8%	SAGE, KamLAND
θ_{13}	9°	4.7%	DAYA Bay,
$-\Delta m_{32}^2$	$2.5 \cdot 10^{-3} \text{ eV}^2$	1.8%	RENO

362 1.2.3 Make up of Neutrino Interactions

363 All neutrino experiments involving the detection of single neutrinos are concerned
 364 with neutrino interactions (and neutrino cross sections) on nuclei. Given the invis-
 365 ible nature of the neutrino, characterizing the products of its interaction is the only
 366 method to a) assess the neutrino presence, b) detect its flavor in case of a charge
 367 current interaction and c) eventually reconstruct its energy.

368 Historically, neutrino interactions with the nucleus in the GeV region are divided
 369 into three categories into three categories whose contributions change as a function

of increasing neutrino energy:: quasi elastic (QE), resonant (RES), and deep inelastic (DIS) scattering. All current and forthcoming oscillation experiments on neutrino beams live in the 0.1-10 GeV transition region, which encompasses the energy where the QE neutrino-nucleus interaction transitions into RES and then into DIS. For scattering off free nucleons, neutrino and antineutrino QE charge current scattering refers to the process $\nu_l n \rightarrow l^- p$ and $\bar{\nu}_l p \rightarrow l^+ n$ where a charged lepton and single nucleon are ejected in the elastic interaction. Resonant scattering refers to an inelastic collision producing a nucleon excited state (Δ, N^*) – the resonance – which then quickly decays, most often to a nucleon and single-pion final state. DIS refers to the head-on collision between the neutrino and a parton inside the nucleon, producing hadronization and subsequent abundant production of mesons and nucleons. In addition to such interactions between the neutrino and a single component of the nucleus, neutrinos can also interact with the nucleus as a whole, albeit more rarely, a well documented process called coherent meson production scattering [58]; the signature of such process is the production of a distinctly forward-scattered single meson final state, most often a pion. This simple picture of neutrino interactions works rather well for scattering off of light nuclear targets, such as the H₂ and D₂ of bubble chamber experiments [64], but the complexity of the nuclear structure for heavier nuclei such as argon complicates this model.

As we will discuss in Chapter 2, the properties of argon make it a good candidate for an interacting medium in neutrino experiments; in particular the density of its interaction centers increases the yield of neutrino interactions and allows for relatively compact detectors. Though, the choice of a relatively heavy nuclear target comes at the cost of enhancing nuclear effects which modify the kinematic and final state of the neutrino interaction products.

Nuclear effects can potentially affect neutrino event rates, final state particle emission, neutrino energy reconstruction, and the neutrino/antineutrino ratios, carrying

397 deep implications for oscillation experiments. Even in the case of “simple” QE scat-
398 tering, intra-nuclear hadron rescattering and correlation effects between the target
399 nucleons can cause the ejection of additional nucleons in the final state, modifying
400 the final state kinematics and topology. In the case of resonant and DIS scattering,
401 the hadronic interactions of meson and nucleons produced in the decay of the res-
402 onance or during hadronization complicate this picture even more. A large source
403 of uncertainty in modeling nuclear effects in neutrino interactions come from mesons
404 interactions (and re-interactions) in the nucleus, e.g., pion re-scattering, charge ex-
405 change, and absorption.

406 A renewed interest for neutrino cross section measurements surged in recent years,
407 along with a lively discussion on the data reporting; the historical method of reporting
408 the neutrino cross section as a function of the neutrino energy or momentum trans-
409 fered shakes under the weight of its dependency on the chosen nuclear model. On one
410 hand, correcting for nuclear effects in neutrino interaction can introduce unwanted
411 sources of uncertainty and model dependency especially due to the mis-modeling of
412 the meson interactions. On the other, avoiding this correction makes a comparison
413 between neutrino interactions on different target nuclei extremely difficult.

414 Data on neutrino scattering off many different nuclei are available for both charged
415 current (CC) and neutral current (NC) channels, as summarized in [64]. A summary
416 of the results on QE, resonant and DIS scattering for neutrinos and antineutrinos from
417 accelerators on different target is reported in Figure 1.1, where the (NUANCE) [37]
418 event generator is used as comparison with the theory.

419 1.3 Beyond the Standard Model

420 The discovery of neutrino oscillation and its implication of non-zero neutrino mass
421 mark the beginning of a new, exciting era in neutrino physics: the era of physics Be-

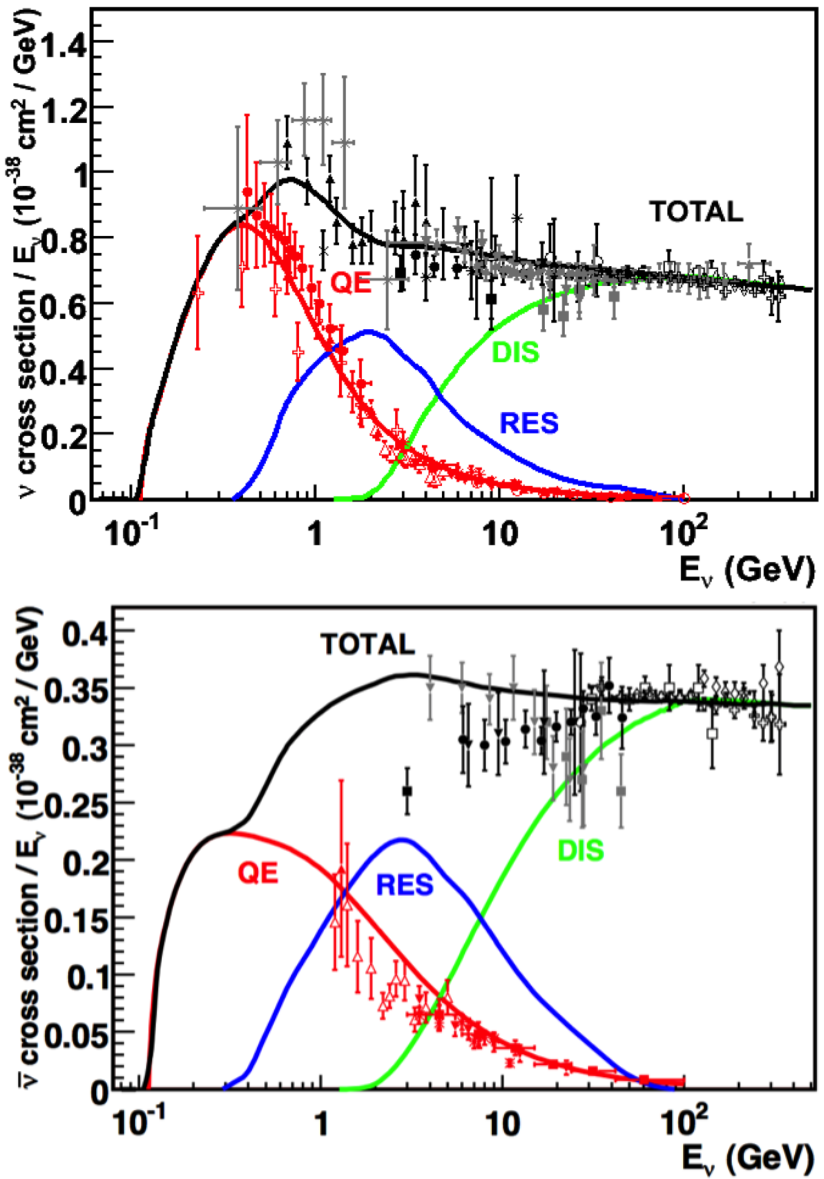


Figure 1.1: Total neutrino (top) and antineutrino (bottom) CC cross sections per nucleon divided by neutrino energy as a function of energy as reported in [64]. Predictions for the total (black), the QE (red), resonant (blue) and DIS (green) are provided by the NUANCE generator. The quasi-elastic scattering data and predictions have been averaged over neutron and proton targets (isoscalar target).

422 yond the Standard Model (BSM) at the intensity frontier. We are currently searching
423 for new, deeper theories that can accommodate neutrinos with tiny but non-zero
424 masses, while remaining consistent with the rest of the Standard Model.

425 **1.3.1 Open Questions in Neutrino Physics**

426 On one hand, the last three decades of experiments in neutrino oscillations brought
427 spectacular advancements in the understanding of the oscillations pattern, measuring
428 the neutrino mixing angles and mass splitting with a precision of less than 10%. On
429 the other, they opened the field for a series of questions needing experimental answers.

430 **Sterile neutrinos.** Hints to the existence of at least one additional neutrino,
431 in the form of various anomalies, have been puzzling physicists almost from the be-
432 ginning of neutrino oscillation searches. Originally designed to look for evidence of
433 neutrino oscillation, the Liquid Scintillator Neutrino Detector (LSND) [54] provided
434 a first conflicting result with the Standard Model expectation of only three neutrinos.

435 A second conflicting result has also been provided by the MiniBooNE experiment [50].
436 The LSND and MiniBooNE ν_e and $\bar{\nu}_e$ appearance results, known as the “LSND and
437 MiniBooNE anomalies” [14, 15, 23], may be interpreted under the assumption of a new
438 right-handed neutrino. The additional neutrino needs to be “sterile”, i.e needs not
439 to couple with the electroweak force carriers, in order to meet the constraint imposed
440 by the measurement of the width of the Z boson [2]. The new sterile neutrino would
441 mainly be composed of a heavy neutrino ν_4 with mass m_4 such that $m_1, m_2, m_3 \ll m_4$
442 and $\Delta m^2 = \Delta m_{14}^2 \sim [0.1 - 10]$ eV². The introduction of sterile neutrinos is an ap-
443 pealing line of thinking, since this renormalizable generalization of the SM has the
444 potential to impact long standing questions in high energy physics and cosmology:
445 light sterile neutrinos are candidates for dark matter particles and there are ideas
446 that the theory could be adjusted to explain the baryon asymmetry of the Universe
447 via leptogenesis [71].

448 **CP Violation In Lepton Sector.** The measurement of non-zero value for the
 449 oscillation parameter θ_{13} allows the exploration of low-energy CP violation in the lep-
 450 ton sector at neutrino long baseline oscillation experiments, enabling the possibility
 451 to measure the Dirac CP-violating phase δ . Exciting theoretical results tie δ directly
 452 to the generation of the baryon asymmetry of the Universe at the Grand Unified
 453 Theory scale **a couple of cit would be nice**. According to the theoretical model de-
 454 scribed in [100], for example, leptogenesis can be achieved if $|\sin \theta_{13} \sin \delta| > 0.11$, i.e.
 455 $\sin \delta > 0.7$.
 456 The asymmetry in the oscillation probability of neutrinos and antineutrinos is the ob-
 457 servable sensitive to the Dirac CP-violating phase δ leveraged in neutrino oscillation
 458 experiments. Using the parameterization of the PMNS matrix shown in Equation
 459 1.9, the difference between the probability of $\nu_e \rightarrow \nu_\mu$ oscillation and the probability
 460 of $\bar{\nu}_e \rightarrow \bar{\nu}_\mu$ oscillation can be parametrized as follows [39],

$$P_{\nu_e \rightarrow \nu_\mu} - P_{\bar{\nu}_e \rightarrow \bar{\nu}_\mu} = J \cos \left(\pm \delta - \frac{\Delta_{31} L}{2} \right) \sin \left(\frac{\Delta_{21} L}{2} \right) \sin \left(\frac{\Delta_{31} L}{2} \right) \quad (1.10)$$

461 where

$$J = \cos \theta_{13} \sin 2\theta_{13} \sin 2\theta_{12} \sin 2\theta_{23} \quad (1.11)$$

462 is the Jarlskog invariant [81], L the neutrino baseline, i.e. the distance between
 463 the neutrino production and detection points, and Δ_{ab} a factor proportional to the
 464 sign and magnitude of the mass splitting. From these equations, it is clear how the
 465 relative large value of θ_{13} is a happy accident necessary not to completely suppress
 466 the sensitivity to CP violation. The equations also show how the sensitivity to δ is
 467 tied to the measurement of the least precisely measured mixing angle, θ_{23} (via the
 468 $\sin 2\theta_{23}$ term) and to an other unknown quantity, the neutrino “mass hierarchy” (via
 469 the Δ_{ab} terms). The precise determination of θ_{23} is often referred as to “the octant
 470 problem”. Current experimental results [3, 12] are consistent with $\theta_{23} = 45^\circ$, which

471 would imply maximal mixing between ν_μ - ν_τ , hinting to an intriguing new symmetry.
472 Therefore, a precise measurement of θ_{23} is of great interest for theoretical models of
473 quark-lepton universality [74, 92, 105], whose quark and lepton mixing matrices are
474 proportional to the deviation of θ_{23} from 45°.

475 **Neutrino mass hierarchy.** The “mass hierarchy” problem refers to the unknown
476 ordering of the value of absolute mass of the neutrino mass eigenstates. Current
477 oscillation experiments are sensitive only to the magnitude of the mass splitting, and
478 not directly to its sign. In a framework where the lightest neutrino mass (arbitrarily)
479 corresponds to the first eigenstate m_1 , it is unknown whether $m_2 - m_1 < m_3 - m_1$
480 (Normal Hierarchy) or $m_2 - m_1 > m_3 - m_1$ (Inverted Hierarchy). The mass hierarchy
481 affects not only the sensitivity to CP violation searches in long baseline oscillation
482 experiments, but also the sensitivity to determine whether neutrinos are Majorana
483 particles in neutrinoless double beta decay experiments.

484 **Majorana or Dirac?** Evidence of neutrino oscillations demands the introduction
485 of a mechanism which can give mass to the neutrinos. This mechanism should possibly
486 also explain why neutrino masses are at least six orders of magnitude lower than the
487 electron mass (the second lightest SM fermion). In a description of neutrinos as Dirac
488 4-component spinors, the neutrino field acquires mass via the Higgs mechanism as
489 any other fermion of the SM. In this case, the neutrino mass is given by $m_a = \frac{y_a^\nu v}{\sqrt{2}}$,
490 where v is the Higgs VEV and y_a^ν is the Yukawa coupling between the Higgs and the
491 neutrino. The smallness of neutrino masses can only be pinned on a tiny Yukawa
492 coupling which is not justified by the theory.

493 In 1937, Majorana demonstrated that the introduction of a two components spinor is
494 sufficient to describe a massive fermion [91]. The Dirac equations of motion for the
495 chiral fields (equations 1.5 and 1.6) hold true in the case of two components spinor
496 under the assumption that the chiral components ψ_R and ψ_L are correlated through
497 the charge conjugation matrix \mathcal{C} , $\psi_R = \mathcal{C}\bar{\psi}_L$. Therefore the theory is applicable only

498 to neutral fermions. Neutrinos are the only neutral elementary particles in the SM
 499 – the only possible Majorana particle candidate. This theory constructs a neutrino
 500 Majorana mass term \mathcal{L}_5 of the following form in the Higgs unitary gauge

$$\mathcal{L}_5 = \frac{1}{2} \frac{gv^2}{\mathcal{M}} \nu_L^T \mathcal{C}^\dagger \nu_L, \quad (1.12)$$

501 where g is the coupling coefficient, v the Higgs VEV and \mathcal{M} a constant with the
 502 dimension of the mass proportional to the scale of new physics. The \mathcal{L}_5 term would
 503 introduce a non-renormalizable term in the lagrangian, since it has dimensions of
 504 energy to the fifth power. This is not allowed in the SM lagrangian; however, the
 505 existence of such terms is plausible if we consider the SM as an effective theory
 506 at low energy, manifestation of the symmetry breaking of a more general theory at
 507 higher energy, e.g. a Grand Unified Theory (GUT), and not the definitive theory.
 508 The mass term in eq 1.12 implies the neutrino mass to be $m = \frac{gv^2}{\mathcal{M}}$. The coupling
 509 coefficient can be of the order of any other fermion's coupling coefficient, since the
 510 smallness of neutrino masses is achieved by the big value of the new physics mass
 511 scale alone. This vanilla formulation is the conceptual basis for many flavors of *see-*
 512 *saw mechanism* [121], which we will not discuss here in any detail. However, it is
 513 fascinating how the puzzle of the neutrino mass hints to the existence of a deeper and
 514 more complete theory.

515 From a kinematic point of view, Dirac and Majorana neutrinos satisfy the same
 516 energy-momentum dispersion relationship. Thus, it is impossible to discern the neu-
 517 trino nature through kinematic effects such as neutrino oscillations. Neutrinoless
 518 double beta decay searches are the most promising way to understand the nature of
 519 the neutrino and are therefore subject of great theoretical and experimental interest.
 520 Observation of the lepton number violating process $0\nu\beta\beta$ would imply neutrinos have
 521 a Majorana component. Depending on the mass hierarchy, the theory also predicts

522 $0\nu\beta\beta$ exclusion regions and confirmation of the sole Dirac component for neutrinos [44].

524

525 1.3.2 Towards a more fundamental theory: GUTs

526 Despite its highly predictive power, a number of conceptual issues arise in the SM
527 which disfavor it to be a good candidate for a fundamental theory.

528 The SM does not include a suitable dark matter candidate and a mechanisms
529 that accounts for the baryon asymmetry of the universe. Additionally, up to a total
530 of 25 parameters remain seemingly arbitrary and need to be fitted to data: 3 gauge
531 couplings, 9 charged fermion masses, 3 mixing angles and one CP phase in the CKM
532 matrix, the Higgs mass and quartic coupling, θ_{QCD} , 3 neutrino mixing angles, 1 Dirac
533 phase and, eventually, 2 Majorana phases.

534 From a group theory perspective, the SM has a rather complex group structure,
535 where a gauge group is formed with the direct product of other three groups as shown
536 in eq. 1.1. Drawing a parallel with the electroweak symmetry breaking mechanism,
537 where the $SU(2)_L \otimes U(1)_Y$ is recovered from $U(1)_{EM}$, an interesting line of simplification
538 for the SM group structure would be to devise a similar mechanism where
539 $SU(3)_C \otimes SU(2)_L \otimes U(1)_Y$ is recovered from an hypothetical larger group. IS THIS
540 CORRECT? Just as the electroweak unification becomes evident at energies higher
541 than the Higgs VEV, a direct manifestation of Grand Unification Theories (GUTs)
542 would occur at even higher energies.

543 As the smallness of neutrino masses suggests the existence of a higher mass scale,
544 an other, even stronger, hint to Grand Unification comes from the slope of running
545 of the coupling constants. The coupling constants for the electromagnetic, weak and
546 strong interactions in the SM vary as a function of the interaction energy as shown
547 in figure 1.2; they do not exactly meet under the current experimental constraints,

⁵⁴⁸ but their trend is interesting enough to push for the construction of theories where
⁵⁴⁹ perfect unification is achieved through the addition of new particles.

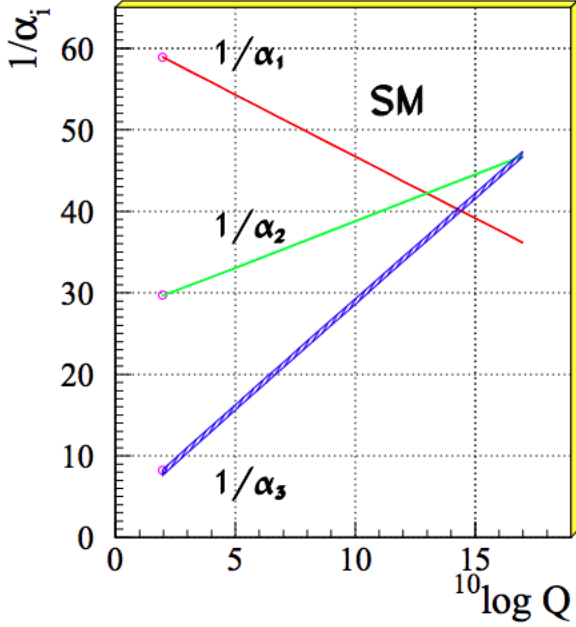


Figure 1.2: Evolution of the inverse of the three coupling constants in the Standard Model as a function of the momentum transferred, [85].

SU(5). The smallest simple group containing $SU(3)_C \otimes SU(2)_L \otimes U(1)_Y$ is $SU(5)$, as shown first by Georgi and Glashow in [68]. Quarks and leptons in this group fit the $\bar{5}$ and 10 representations. The representation for left-handed fermions are the following

$$\bar{5} = (\nu_e, e^-)_L + \bar{d}_L \quad (1.13)$$

$$10 = e_L^+ + \bar{u}_L + (u, d)_L, \quad (1.14)$$

⁵⁵⁰ while the boson structure gains a new couple of super heavy bosons (X,Y)

$$24 = \underbrace{(8, 1)}_{\text{gluons}} + \underbrace{(1, 3) + (1, 1)}_{W^\pm, Z, \gamma} + \underbrace{(3, 2) + (\bar{3}, 2)}_{X, Y \text{ bosons}}. \quad (1.15)$$

⁵⁵¹ Nice features such as charge quantization and the identity between the positron

and proton charge value come directly from the group structure. The new super heavy bosons are colored and form a weak doublet. Their are the mediator of the interaction that turns quarks into leptons, leading to predict the existence of processes that violate baryon number, such as $p \rightarrow \pi^0 + e^+$ (see fig 1.8, right). The prediction for proton decay lifetime, $\tau_p \sim \frac{M_X^4}{m_p^5} \sim 10^{30 \pm 1.5}$ years, is unfortunately experimentally disproved by IMB and Super-Kamiokande [4, 28].

SO(10). More complicated group structures, such as SO(10) are still viable candidates for GUT. SO(10) includes the same type of X and Y bosons as SU(5). Right-handed massive neutrinos are embedded in the construction of the irreducible representation of SO(10). Different patterns of SO(10) symmetry breaking to recover the SM are possible and lead to different predictions for the proton decay lifetime; some of these predictions are not excluded by the experiments [86].

SUSY GUTs. Supersymmetry theories allow for another family of GUTs. In SUSY, every fundamental particle in the SM has a “superpartner”, identical in each quantum number except for the spin-statistics: the fermion supersymmetric partners are bosons and vice versa. Collider experiments (mainly LHC) constrain the mass of the supersymmetric partners to be very heavy [?]. The SU(5), SU(10) groups with a SUSY twist are the basic groups for SUSY GUTs. From the phenomenology point of view, SUSY models tend to push the proton decay life time higher by a factor of four, they solve the “hierarchy problem”, and they also predict new channels for the proton decay. In particular they predict the presence of kaons in the final product, with a dominant mode of $p \rightarrow K^+ \bar{\nu}$. Predictions on the proton decay lifetime depend on the chosen SUSY model; again, some of the predictions are not excluded by the experiments [89, 90, 109].

576 **1.4 Motivations for Hadronic Cross Sections in Ar-**
577 **gon**

578 Critical challenges await the next decade of high energy physics at the intensity
579 frontier. Following the recommendation of the latest Particle Physics Project Priori-
580 tization Panel [106], the US is dedicating substantial resources to the development of
581 a short- and long- baseline neutrino program to address many of open questions in
582 neutrino physics today. This program pivots on the Liquid Argon Time Projection
583 Chamber (LArTPC) detector technology which will be described in Chapter 2.

584 The main goals of these research programs include:

- 585 - the assessment of the existence of right-handed sterile neutrinos via the study
586 of accelerator neutrinos on a short baseline (SBN),
- 587 - the determination of the sign of Δm_{13}^2 (or Δm_{23}^2), i.e., the neutrino mass hier-
588 archy via the study of accelerator neutrinos on a long baseline (DUNE),
- 589 - the determination of the octant, i.e. whether θ_{23} is maximal, via the study of
590 accelerator neutrinos on a long baseline (DUNE),
- 591 - the determination the status of CP symmetry in the lepton sector, via the study
592 of accelerator neutrinos on a long baseline (DUNE),
- 593 - the search for observables predicted by GUTs, such as proton decay via the
594 study of non accelerator physics in massive underground detectors (DUNE).

595 **1.4.1 Pion-Argon Total Hadronic Cross Section**

596 This section outlines the importance of the pion-argon total hadronic cross section in
597 the context of the current and upcoming liquid argon neutrino experiments, SBN and
598 DUNE. We describe the signal signature and historic measurements of pion-nucleus

599 cross section, as well as the implementation of these cross sections in the current
600 version of the simulation package used by LArIAT.

601 π^- Ar Cross Section in the Context of Neutrino Searches

602 As outlined in 1.2.3, neutrino experiments use the products of neutrino interactions
603 to identify the energy and flavor of the incoming neutrino. Pions are a common
604 product of neutrino interaction, especially in resonant scattering, DIS and coherent
605 pion production. For neutrino experiments in argon, there are two main reasons
606 why understanding pion hadronic interactions with argon is important: to model the
607 behavior of the pion inside the target nucleus and to model the behavior of the pion
608 during its propagation inside the detector medium.

609 Assumptions on the nuclear modeling and on the interaction of hadrons inside the
610 nucleus performed at the level of the neutrino event generator bridge the measure-
611 ment of the products of a neutrino interaction to the reconstruction of the neutrino
612 energy and flavor. Thus, understanding pion hadronic interactions with the nucleus is
613 particularly important to model correctly resonant, DIS and coherent pion production
614 in neutrino interactions. For example, in case of resonant scattering,

$$\nu_l + N \rightarrow l + \Delta/N^* \rightarrow l + \pi + N', \quad (1.16)$$

615 the Δ and N^* and excited states will decay hadronically in matters of $\sim 10^{-24}$ s
616 inside the nucleus producing pions which will have many chances to re-interact
617 as they exit the target medium. The decay modes for the lower mass Δ (1232) and
618 $N^*(1440)$ are listed in table 1.3.

619 The key elements of a neutrino event generators for resonance and DIS events
620 are the nuclear model and the hadron treatment (both production and transporta-
621 tion). We illustrate here the conceptual basis of the GENIE Neutrino Generator [18]

622 as an example, since GENIE is one the most popular event generators for liquid ar-
623 gon experiments. For example, the nuclear model used by GENIE for all processes
624 is a Relativistic Fermi Gas (RFG) model modified to incorporate nucleon-nucleon
625 correlations [30]. This means that the initial momentum and binding energy of the
626 struck nucleon is determined by assuming nucleons inside the nucleus are quasi-free,
627 acting independently in the mean field of the nucleus. For $A > 20$ such as argon, the
628 2-parameter Woods-Saxon shell model for density function is used. The GENIE mod-
629 ule INTRANUKE [84] is used to simulate final-state interactions (FSI) which model
630 hadron re-interactions inside the nucleus. This module places the outgoing parti-
631 cles in the nucleus and propagates them using the “hA model”. In the INTRANUKE
632 hA model, hadrons can undergo at most one FSI per event. When possible, external
633 hadron-nucleus scattering data are used to tune INTRANUKE. Since no data is avail-
634 able for Argon, GENIE uses an interpolation of data from heavier and lighter nuclei
635 for the pion-argon cross section leading to large (10?s of %) resultant uncertainties in
636 the INTRANUKE module.

637 Once the pion has left the target nucleus, the pion-argon hadronic cross section also
638 plays an important role in the pion transportation inside the argon medium: processes
639 such as pion absorption or pion charge exchange can greatly modify the topology of
640 a neutrino interactions in the detector and lead to significant modifications in the
641 event classification. Being able to reconstruct the details of pions inside the detector
642 is an imperative for modern liquid argon neutrino experiment to achieve the design
643 resolution for their key physics measurements.

644 π^- -Ar Hadronic Interaction: Signal Signatures

645 Strong hadronic interaction models [49,69] predict the pion interaction processes with
646 argon in the [100 - 1200] MeV energy range. The total hadronic π^- -Ar interaction
647 cross section is defined as the one related to the single process driven only by the

648 strong interaction which is dominant in the considered energy range. In measuring
649 the “total” cross section, we include both the elastic and reaction channels, regardless
650 of the final state,

$$\sigma_{Tot} = \sigma_{Elastic} + \sigma_{Reaction}; \quad (1.17)$$

651 the reaction channel is further characterized by several exclusive channels with defined
652 topologies,

$$\sigma_{Reaction} = \sigma_{Inelastic} + \sigma_{abs} + \sigma_{chex} + \sigma_{\pi prod}. \quad (1.18)$$

653 A summary of the pion final states in order of pion multiplicity for the reaction
654 channel is given in table 1.4. Pion capture and pion decay at rest dominate the
655 cross section under 100 MeV. We define pion capture as the process determining the
656 formation of a pionic atom and the subsequent pion’s end of life. Stopping negative
657 pions can form pionic argon, where the negative pion plays the role of an orbital
658 electron. Since the pion mass is two orders of magnitude greater than the electron
659 mass, the spatial wave form of the pion will overlap more with the nucleus compared
660 to the electron case. After the electromagnetic formation of the pionic atom, the
661 pion will get quickly absorbed by the nucleus, which is put in an excited state. The
662 nucleus then de-excites with the emission of low energy nucleons and photons. Pion
663 capture is dominant compared to pion decay, the other important process for very
664 low energy pions. The decay of a pion is governed by the weak force; the pion decay
665 life time is $\tau_\pi = 2.6 \times 10^{-8}$ s and the main decay mode is $\pi^- \rightarrow \mu^- + \bar{\nu}_\mu$ (BR 99.98%).
666 Since pion capture can be considered an electromagnetic process and pion decay is a
667 weak process, this energy region is purposely excluded from the hadronic cross section
668 measurement.

669 **Previous measurements: Lighter and Heavier Nuclei**

670 Many experiments with pion beams have studied the hadronic interaction of pions on
671 light and heavy materials, such as He, Li, C, Fe, Pb [36]. However, data on argon are
672 rare: the total differential hadronic cross section has never been measured before on
673 argon. Simulation packages such as Geant4 base their pion transportation for argon
674 on data from lighter and heavier nuclei: the goal of LArIAT’s dedicated measurement
675 on argon is to bridge this gap in data, thus reducing the uncertainties related to pion
676 interactions in argon in both neutrino event generators and in simulation packages of
677 pion transportation.

678 The shape of the pion-nucleus interaction cross section in the energy range con-
679 sidered shows the distinct features indicating the presence of a resonance. In fact, the
680 mean free path of a pion of kinetic energy between 100 and 400 MeV is much shorter
681 than the average distance between nucleons (which is of the order of 1 fm). There-
682 fore, the pion interacts with surface nucleons. A Δ resonance is often produced in
683 the interaction, which subsequently decays inside the nucleus. Experimental results
684 on several nuclei as reported in [36] are shown in Figure 1.3; it is interesting to notice
685 here how the shape of the Δ resonance becomes less pronounced as a function of the
686 mass number of the target nucleus. Pion interactions with heavier nuclei also shift the
687 peak of the resonance at lower energy; this effect is due to kinematic considerations
688 and to the difference in propagation of the Δ inside the nucleus. Multiple scattering
689 effect modify the resonance width, which is larger than the natural-decay width. As
690 an example of a fairly well studied target, Figure 1.4 reports the negative pion cross
691 section on Carbon for the elastic and reaction² channels, and their sum [55].

2. This paper calls “inelastic interaction” what we refer as to “reaction channel”.

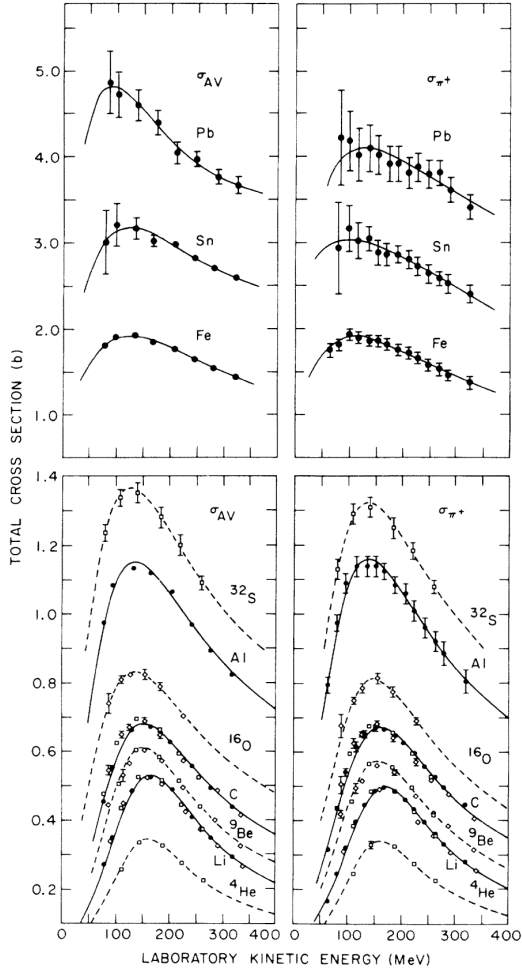


Figure 1.3: Pion-nucleus total cross sections: σ_{π^+} for positive pions (right) and σ_{AV} (left) for the average between positive and negative pions $\sigma_{AV} = \frac{\sigma_{\pi^+} + \sigma_{\pi^-}}{2}$ in the Δ resonance region. The error bars include estimates of systematic uncertainties. The curves are the results of fits to the data assuming a Breit-Wigner shape. This summary plot is reported in [36] and uses data from [52, 117].

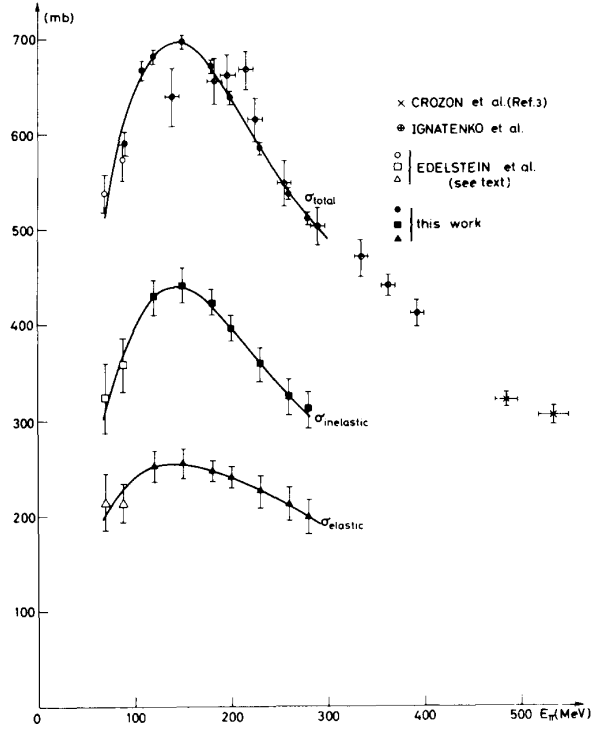


Figure 1.4: Negative pion nucleus total, elastic and reaction cross sections on ^{12}C as from [55].

692 Negative Pion Interaction Cross Section in Simulation Packages

693 LArIAT uses Geant4 as the default simulation package. In particular, pions (and
 694 kaons) transportation is achieved through the Geant4 FTFP_BERT physics list. In
 695 this physics list, Geant4 uses the Bertini cascade model [118] to simulate the products
 696 of the pion-nucleus interaction as well as secondary hadronic re-interactions inside
 697 the target nucleus (intra-nuclear cascade). The target nucleus is represented as a
 698 continuous gas where the nuclear potential follows concentrical shells whose depths
 699 approximate the Woods-Saxon shape. The CERN-HERA compilations [113, 114] of
 700 hadron-nucleon interaction data is the data base used for the decision making process
 701 after the cascade is invoked. The cross section model determines if the pion inter-
 702 acts, the eventual type of interaction and the interaction multiplicity. For hadron
 703 projectiles with energy less than 20 GeV, Geant4 reports the uncertainty on the cross

704 section model to be about the size of the error bars on the data used, or about 10%,
705 increasing to 20-30% in energy regions where data is sparse.

706 The relevance of the GENIE generator for neutrino physics and its basic working
707 principles have been outlined earlier in this section. Given GENIE’s modularity,
708 information on hadron-nucleus interactions can be extracted from the INTRANUKE
709 module and directly compared against the Geant4 predictions. The work in [97]
710 reviews the current status of negative and positive pion simulation in Geant4 and
711 GENIE for ^{12}C , ^{56}Fe , and ^{40}Ca . From that work, we report the results for ^{12}C in
712 Figure 1.5 as it allows a direct comparison between Geant4, GENIE and pion
713 re-scattering data. Geant4 predictions for π^- on Carbon are in good agreement with
714 data over the entire spectrum, while GENIE predictions seem to show some
715 features at around 500 MeV and 900 MeV, maybe due to higher resonances in the hA
716 model. From the same work, we also report the negative pion cross section on ^{40}Ca
717 in Figure 1.6, since this is the nuclear medium closest to argon. The predictions from
718 both Geant4 and GENIE agree with data in the high energy region; the Geant4 and
719 GENIE predictions diverge in the resonance region, where data is not available. These
720 few examples highlight how cross section data for the specific nucleus considered in
721 the neutrino experiments is fundamental to inform the Monte Carlo simulation.

722 For the LArIAT simulation of the MC sample used in the π^- argon total hadronic
723 cross section measurement we use the Geant4 Bertini Cascade model, whose predic-
724 tions for the total, elastic and reaction hadronic cross sections are show in Figure
725 1.7.

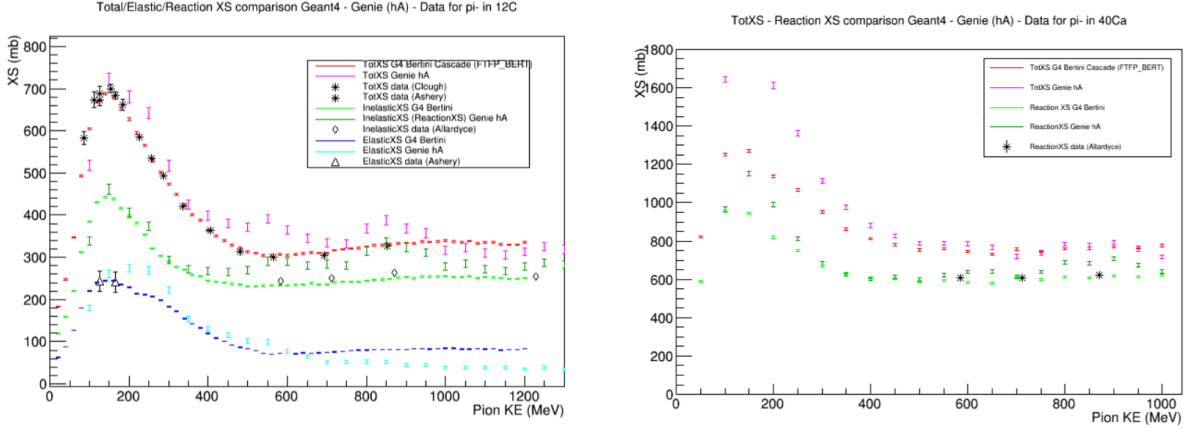


Figure 1.5: Total, elastic and reaction cross section for π^- on ^{12}C . Comparison between results from Geant4 simulation (Bertini cascade model), Genie simulation (hA model), and experimental data [22, 52, 53, 108].

Figure 1.6: Total, elastic and reaction cross section for π^- on ^{40}Ca . Comparison between results from Geant4 simulation (Bertini cascade model), Genie simulation (hA model), and experimental data [53].

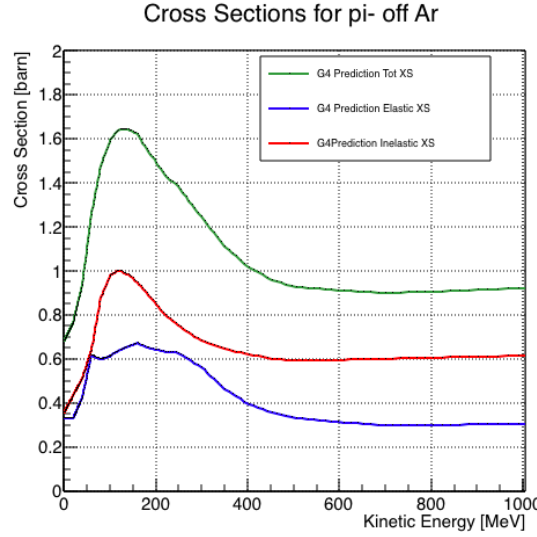


Figure 1.7: Total, elastic and reaction hadronic cross section for π^- -argon implemented in Geant4 10.01.p3.

Resonance	Decay Mode	Lifetime (s)
Δ (1232) $3/2^+$	$\Delta^{++}(\text{uuu}) \rightarrow p\pi^+$ $\Delta^+(\text{uud}) \rightarrow n\pi^+$ $\Delta^+(\text{uud}) \rightarrow p\pi^0$ $\Delta^0(\text{udd}) \rightarrow n\pi^0$ $\Delta^0(\text{udd}) \rightarrow p\pi^-$ $\Delta^-(\text{ddd}) \rightarrow n\pi^-$	$\sim 5.6 \times 10^{-24}$
N^* (1440) $1/2^+$	$N^* \rightarrow N\pi$ $N^* \rightarrow N\pi\pi$	$\sim 2.2 \times 10^{-24}$

Table 1.3: Main decay modes of the lightest Delta resonance and Nucleon excited state.

N π in FS	Channel Name	Reaction	Notes
0	Pion Absorption, σ_{abs}	$\pi^-(np) \rightarrow nn$ (2-body abs) $\pi^-(nnp) \rightarrow nnn$ (3-body abs) $\pi^-(npp) \rightarrow pnn$ (3-body abs) $\pi^-(nnpp) \rightarrow pmn$ (Multi-body abs)	Suppressed on single nucleon by energy conservation: the process occurs on at least two nucleons system.
1	Elastic Scattering, σ_{el}	$\pi^- + N \rightarrow \pi^- + N$	Scattering on nucleon or nucleus, the target is left in ground state
1	Charge Exchange, σ_{chea}	$\pi^- + p \rightarrow \Delta^0 \rightarrow \pi^0 + n$ $\pi^- + N \rightarrow \pi^+ +$ nucleons	Single charge exchange: charged pion converts into neutral pion Double charge exchange: charged pion converts into opposite charge pion
1	Inelastic Scattering, σ_{inel}	$\pi^- + p \rightarrow \Delta^0 \rightarrow \pi^- + p$ (knock-out) $\pi^- + n \rightarrow \Delta^- \rightarrow \pi^- + n$ (knock-out)	Other possible reactions: Pure Inelastic scattering: population of low energy bound excited states Nuclear break-up with nucleons or fragments knock-out
2+	Pion Production, $\sigma_{\pi prod}$	$\pi^- + N \rightarrow \geq 2\pi +$ nucleons	Possible if pion K.E ≥ 500 MeV/c

Table 1.4: Summary of negative pion hadronic interactions of the reaction channel as a function of the pion multiplicity in the final state in the energy range [100-1200] MeV.

726 **1.4.2 Kaon-Argon Total Hadronic Cross Section**

727 This section outlines the importance of the kaon-argon total hadronic cross section.
728 We start by discussing the measurement in the context of nucleon decay searches. We
729 then describe the signal signature and historical measurements of kaon-nucleus cross
730 section, as well as the implementation of this cross sections in the current version of
731 the simulation package used by LArIAT.

732 **K⁺Ar Cross section in the Context of Nucleon Decay Searches**

733 Baryon number is accidentally conserved in the Standard Model. Even though no
734 baryon number violation has been experimentally observed thus far, no underlying
735 symmetry in line with the Noether paradigm [96] explains its conservation. As shown
736 in section 1.3.2, almost all Grand Unified Theories predict at some level baryon num-
737 ber violation in the form of nucleon decay on long time-scales. Given the impossibil-
738 ity to reach grand unification energy scales with collider experiments (Energy Scale
739 > 10¹⁵ GeV), an indirect proof of GUTs is needed. The experimental observation of
740 nucleon decay may be the only viable way to explore these theories.

741 In case of nucleon decay discovery, the dominant decay mode may uncover addi-
742 tional information about the GUT type. Supersymmetric GUTs [24, 46] prefer the
743 presence of kaons in the products of the decay, e.g. $p \rightarrow K^+ \bar{\nu}$ (see fig 1.8, left).
744 Gauge mediated GUTs, in which new gauge bosons are introduced that allow for the
745 transformation of quarks into leptons, and vice versa, prefer the mode $p \rightarrow e^+ \pi^0$ (see
746 fig 1.8, right).

747 LArIAT tiny active volume makes it impossible for the experiment to place com-
748 petitive limits on nucleon decay searches. However, LArIAT provides excellent data
749 to characterize kaons in liquid argon for the “LAr golden mode”, $p \rightarrow K^+ \bar{\nu}$. The
750 result of these studies will affect future proton decay searches in LArTPCs. Previous
751 work has been done to assess the potential identification efficiency for different decay

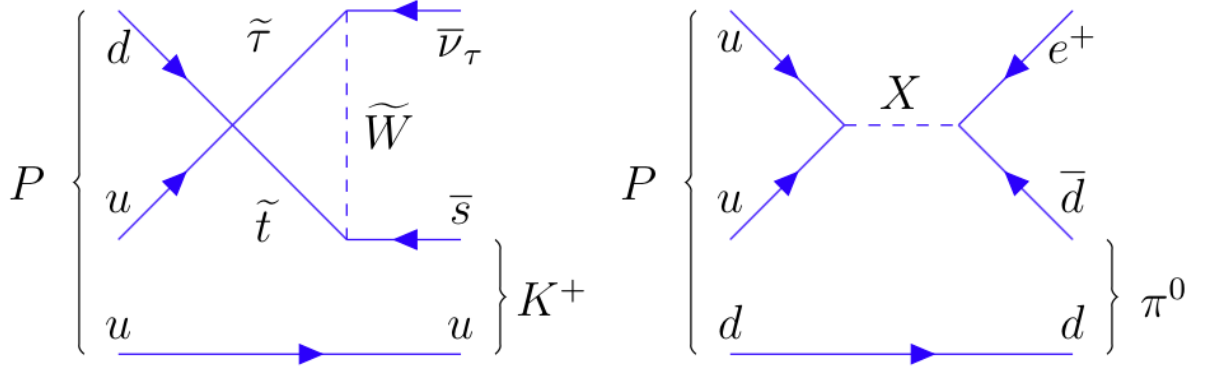


Figure 1.8: Feynman diagrams for proton decay “golden modes”: $p \rightarrow K^+\bar{\nu}$ for supersymmetric GUTs on the left and $p \rightarrow e^+\pi^0$ for gauge-mediated GUTs on the right.

752 modes in a LArTPC [51], but, as the time of this writing, no study of kaon selection
 753 efficiency in LArTPCs has been performed on data. The K^+ -Ar interaction cross
 754 section has never been measured before and can affect the possibility of detecting
 755 and measuring kaons when produced in a proton decay event. Kaon interactions with
 756 argon can distort the kaon energy spectrum as well as change the topology of single
 757 kaon events. In a LArTPC, non-interacting kaons appear as straight tracks with a
 758 high ionization depositions at the end (Bragg peak). The topology of interacting
 759 kaons can be quite different. In case of elastic scattering, a distinct kink will be
 760 present in the track. In case of inelastic scattering the Bragg peak will not be present
 761 and additional tracks will populate the event. Performing the total hadronic K^+ -Ar
 762 cross section measurement on data serves the double purpose of identifying the rate
 763 of “unusual” topologies (kinks and additional tracks) and of developing tools for kaon
 764 tracking in LAr.

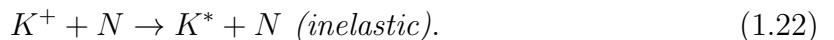
765 **K^+ Ar Hadronic Interaction: Signal Signatures**

The interaction of a mildly relativistic charged kaon with an argon nucleus is determined largely by the strong force. The total hadronic K^+ -Ar interaction cross section

is defined as the one related to the single (hadronic) process driven only by the strong interaction. In this case, “total” indicates all strong interactions regardless of the final state. This condition purposefully includes both elastic and inelastic (reaction) channels. Indeed, the total cross section section can be then decomposed into

$$\sigma_{Tot} = \sigma_{Elastic} + \sigma_{Reaction}.$$

766 For the LArIAT cross section analysis, the kaons considered span a momentum
767 inside the TPC from 100 MeV/c to 800 MeV/c. In this energy range, the relevant
768 K-Nucleon interactions are according to [63]:



769 **Previous Measurements: Lighter and Heavier Nuclei**

770 In general, measurements on kaon cross sections are extremely scarce. The mea-
771 surement of the kaon interaction cross section would bring the additional benefit
772 of reducing the uncertainties associated with hadron interaction models adopted in
773 MC simulations for argon targets, beneficial for both proton decay studies and kaon
774 production from neutrino interaction studies, where the uncertainties for final state
775 interaction models are big [47].

776 Figure 1.9 shows a 1997 measurement on several elements as performed by Fried-
777 mann et al. [65]. As a reference, this paper measures a σ_{Tot} for Si of 366.5 ± 4.8
778 mb and a σ_{Tot} for Ca of 494.6 ± 7.7 mb at 488 MeV/c. The cross section for argon

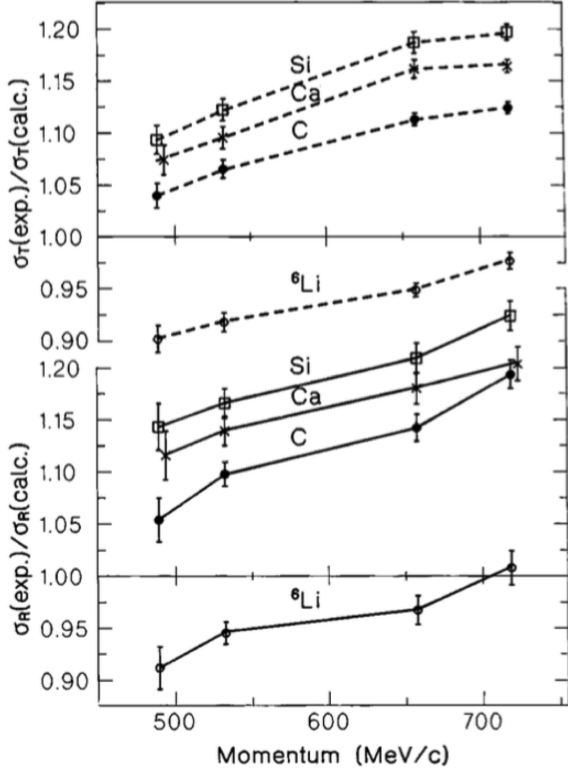


Figure 1.9: Ratios between experimental and calculated cross sections as from [65].
Top: Total cross sections.
Bottom: reaction cross sections.

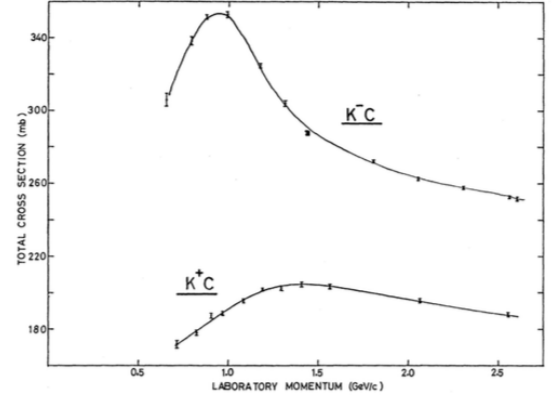


Figure 1.10: Total K^+ and K^- cross sections on carbon as from [32].

is expected to lie in between these two measurements. Additional data on the kaon cross section are provided by Bugg et al. [32]. Bugg performs a measurement of the total K^+ and K^- cross sections on protons and deuterons over the range of 0.6-2.65 GeV/c, as well as a measurement of the total K^+ and K^- cross sections on carbon for a number of momenta; the results of this paper on carbon are reported in Figure 1.10.

785 Kaon Interaction Cross Section for thin target in Geant4

Since the kaon cross section in argon has never been measured before, simulation packages tune kaon transportation in argon by extrapolation from lighter and heavier nuclei. LArIAT uses the Geant4 suite for particle transportation. Since kaon data on

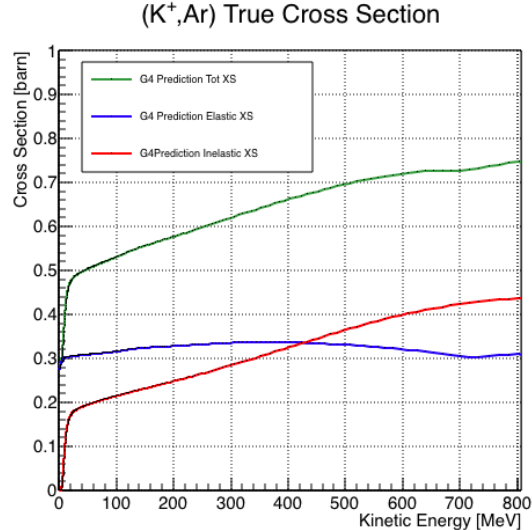
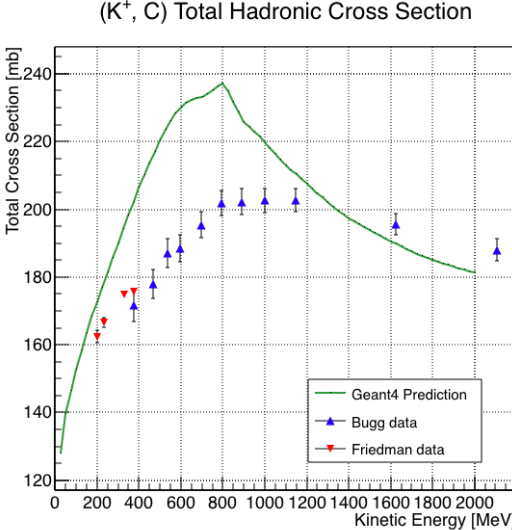


Figure 1.11: Total hadronic cross section for carbon implemented in Geant4 10.01.p3 with overlaid with the Bugg and Friedman data.

Figure 1.12: Total, elastic and reaction hadronic cross section for K^+ -argon implemented in Geant4 10.01.p3.

carbon are available, we used it as a metric to evaluate the Geant4 prediction performances. Figure 1.11 shows the total hadronic cross section for carbon implemented in Geant4 10.01.p3 overlaid with the Bugg and Friedman data. Unfortunately, version 10.01.p3³ of Geant4, which is the version used for the simulation in this work, does not reproduce the data for carbon closely. On one hand, this evidence makes us even more wary when using the Monte Carlo in simulating the kaon-argon interactions. On the other, it further highlights the importance of the kaon measurement. For the LArIAT simulation of the MC sample used in the K^+ argon total hadronic cross section measurement we use the Geant4 Bertini Cascade model, whose predictions for the total, elastic and reaction hadronic cross sections are shown in Figure 1.12.

3. It should be noted that the latest Geant4 version, 10.03.p3, uses a different parametrization for the kaon cross section and retrieves a better agreement with data.

799 **Chapter 2**

800 **Liquid Argon Detectors at the**
801 **Intensity Frontier**

802 “*Don’t you know, honey,*
803 *Ain’t nobody ever gonna love you, the way I try to do?*”
804 – Janis Joplin, 1971 –

805 In the next few years, LArTPCs will be the tools to answer some of the burning
806 questions in neutrino physics today. This chapter illustrates the operational principles
807 of this detector technology, as well as the scope of the key detectors in the US liquid
808 argon program – SBN, DUNE and LArIAT.

809 **2.1 The Liquid Argon Time Projection Chamber**
810 **Technology**

811 In this section, we outline an extremely brief history of Time Projection Chambers
812 as particle detectors, focusing on their incarnation as Argon detectors for neutrino
813 physics. We further describe the working principles of Liquid Argon Time Projection

814 Chambers, leading to the description of the event reconstruction in LArTPC.

815 2.1.1 TPCs, Neutrinos & Argon

816 David Nygren designed the first Time Projection Chamber (TPC) in the late 1970s [98]
817 for the PEP-4 experiment, a detector apt to study electron-positron collisions at the
818 PEP storage ring at the SLAC National Accelerator Laboratory. From the original
819 design in the seventies – a cylindrical chamber filled with methane gas – the TPC
820 detector concept has seen many incarnations, the employment of several different
821 active media and a variety of different particle physics applications, including, but
822 not limited to the study of electron/positron storage rings (e.g. PEP4, TOPAZ,
823 ALEPH and DELPHI), heavy ions collisions in fixed target and collider experiments
824 (e.g. EOS/HISSL and ALICE), dark matter (ArDM), rare decays and capture (e.g.
825 TRIUMF, MuCap), neutrino detectors and nucleon decay (ICARUS, SBN, DUNE),
826 and neutrino less double beta decay (Next). A nice review of the history of TPCs
827 and working principles is provided in [77].

828 Several features of the TPC technology make these detectors a more versatile tool
829 compared to other ionization detectors and explain such a wide popularity. TPCs are
830 the only electronically read detector which deliver simultaneous three-dimensional
831 track information and a measurement of the particle energy loss. Leveraging on both
832 tracking and calorimetry, particle identification (PID) capabilities are enhanced over
833 a wide momentum range.

834 Historically, the active medium in ionization detectors has been in the gaseous
835 form. Carlo Rubbia first proposed the use of a Liquid Argon TPC for a neutrino
836 experiment, ICARUS [107], in 1977. Using nobles elements in the liquid form for
837 neutrino detectors is advantageous for several reasons. The density of liquids is \sim 1000
838 times greater than gases, augmenting the number of targets for neutrino's interaction
839 in the same volume, in a effort to balance the smallness of neutrino cross section. Since

Element	LAr	LXe
Atomic Number	18	54
Atomic weight A	40	131
Boiling Point Tb at 1 atm	87.3 K	165.0 K
Density	1.4 g/cm ³	3.0 g/cm ³
Radiation length	14.0 cm	2.8 cm
Moliere Radius	10.0 cm	5.7 cm
Work function	23.6 eV	15.6 eV
Electron Mobility at $E_{field} = 10^4$ V/m	0.047 m ² /Vs	0.22 m ² /Vs
Average dE/dx MIP	2.1 MeV/cm	3.8 MeV/cm
Average Scintillation Light Yield	40000 γ /MeV	42000 γ /MeV
Scintillation λ	128 nm	175 nm

Table 2.1: LAr, LXe summary of properties relevant for neutrino detectors.

the energy loss of charged particle is proportional to the target material density, as shown in the Bethe-Block equation (eq. 2.1), the increased density reflects into a proportionally higher energy loss, enhancing the calorimetry capability of detectors with a liquid active medium. Additionally, the ionization energy of liquids is smaller than gasses by the order of tens of eV. Thus, at the passage of charged particles, liquids generally produce more ionization electrons than gases for the same deposited energy, forcing the particles to deposit more energy in a shorter range. The downside of using noble liquid elements in experiments is that they require expensive cryogenic systems to cool the gas until it transitions to its the liquid form. The properties of liquid argon in comparison liquid xenon – a popular choice for dark matter and neutrinoless double beta decay detectors – are summarized in table 2.1. Albeit xenon would be more desirable than argon given some superior properties such as lower ionization energy and higher density and light yield, argon relative abundance abates the cost of argon compared to xenon, making argon a more viable choice for the construction of ton (and kilo-ton) scale neutrino detectors.

LArTPCs are some times referred as to “electronic” bubble-chambers, for the similarity in the tracking and energy resolution which is coupled with an electronic readout of the imaging information in LArTPCs. Compared to these historic detectors

858 however, LArTPC bestow tridimensional tracking and a self triggering mechanism
859 provided by the scintillation light in the liquid argon. An event display of a ν_μ CC
860 interaction candidate in the MicroBooNE detector is shown in picture 2.1 to display
861 the level of spatial details these detectors are capable of; the color scale of the image
862 is proportional to the energy deposited, hinting to these calorimetry capabilities of
the detectors.

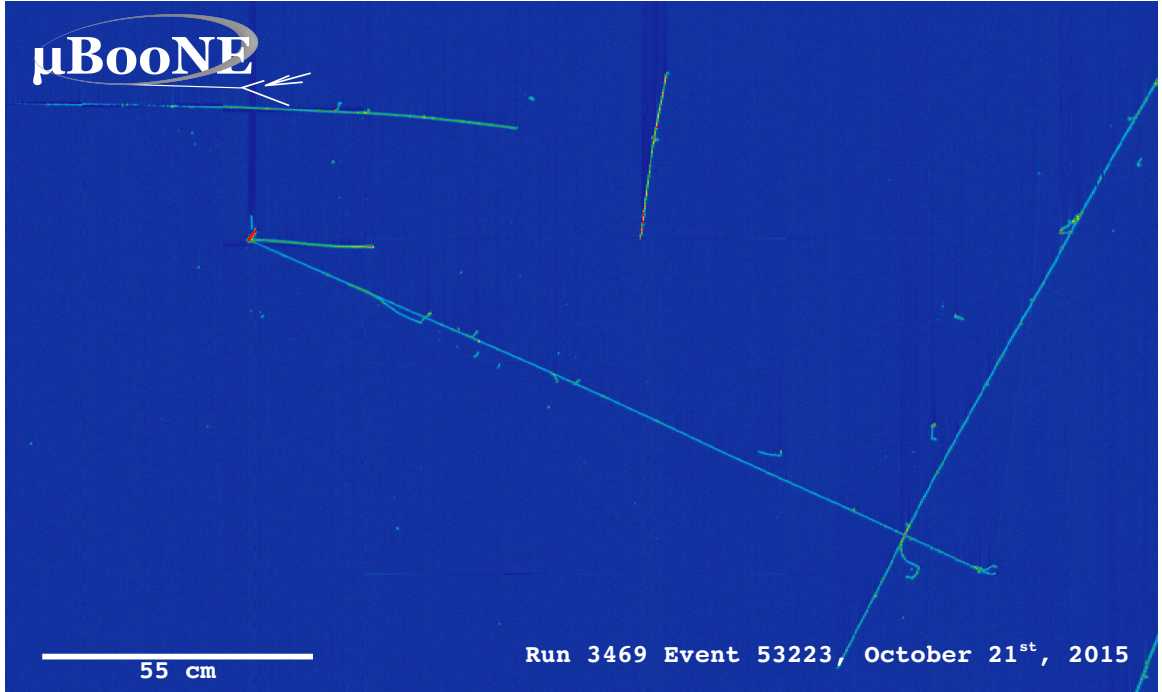


Figure 2.1: Event display of a ν_μ CC interaction candidate in the MicroBooNE detector.

863

864 2.1.2 LArTPC: Principles of Operation

865 To the bare bones, a LArTPC is a bulk of liquid argon sandwiched in a flat capacitor,
866 equipped with a light collection system, as the cartoon in 2.2 shows. A uniform
867 electric field of the order of 500 V/cm is maintained constant between the faces of the
868 capacitor. The anode is sensitive to ionization charge and it is usually made of two
869 or more planes segmented into several hundreds parallel sense wires a few millimeters
870 apart; different geometries for the anode segmentation are under study [48].

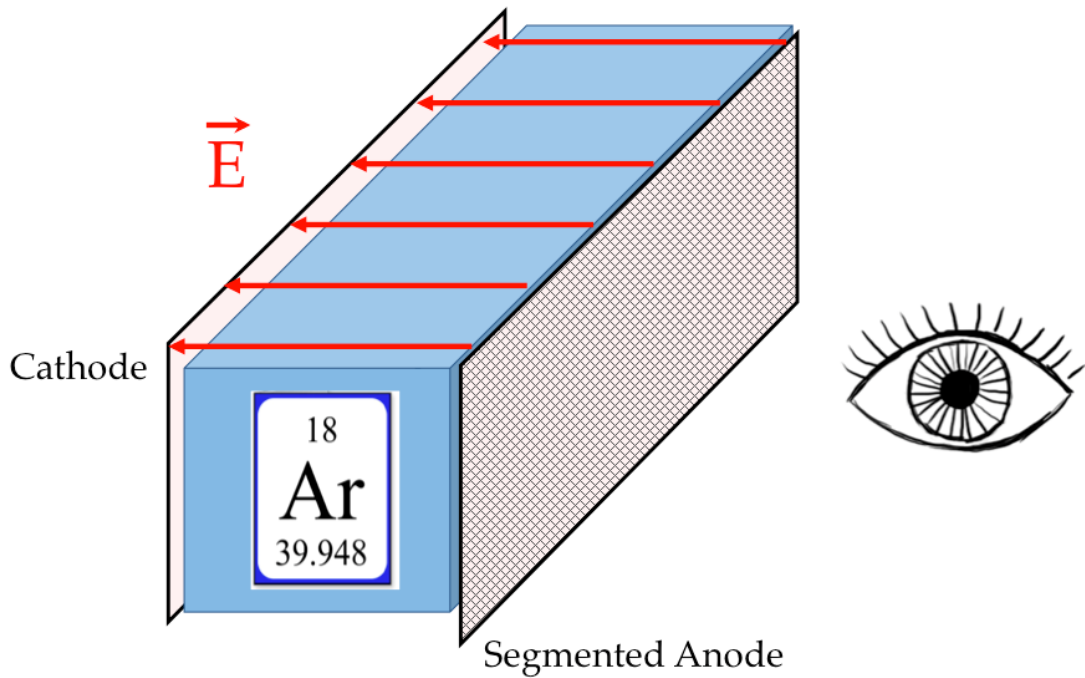


Figure 2.2: A cartoonish sketch of a LArTPC.

Argon ionization and scintillation are the processes leveraged to detect particles in the LArTPC active volume. When a ionizing radiation traverses the argon active volume it leaves a trail of ionization electrons along its trajectory and it excites the argon producing scintillation light – details on the production and detection of ionization charge and scintillation light are provided in 2.1.4 and 2.1.4 respectively. The optical detector sees the argon scintillation light in matters of nanoseconds. This flash of light determines the start time of an event in the chamber, t_0 . The uniform electric field drifts the ionization electrons from the production point towards the anode in order of hundreds of microseconds or more depending on the chamber dimensions¹. The anode sense wires see either an induced current by the drifting ionization charge (on induction planes) or an injection of such charge (collection

1. The ionized argon also drifts, but in the opposite directions compared to the electrons. Since the drift time is proportional to the particle mass, the ions' drift time is much longer than the electrons'. Ionized argon is collected on the cathode which is not instrumented, so it is not used to infer information about the interactions in the chamber.

882 plane). An appropriate choice of the voltage bias on each wire plane assures ideal
883 charge transparency, so that all the ionization charge is collected on the collection
884 plane and none on the induction planes.

885 The arrival time of the charge on the anode sense wires is used to measure the
886 position of the original ionizing radiation in the drift direction. In fact, since the
887 constant electric field implies that the drift velocity is also constant, the position of
888 the original ionization is simply given by the multiplication of the drift velocity by the
889 drift time, where the “drift time” is the difference between t_0 and the charge arrival
890 time on the wire planes. The spacial resolution on this dimension is limited by the
891 time resolution of the electronics or by longitudinal diffusion of the electrons. The
892 spatial information on the different wire planes maps a bi-dimensional projection of
893 the interaction pattern in the plane perpendicular to the drift direction. The spacial
894 resolution on this dimension is limited by the transverse electron diffusion in argon
895 and by the grain of the anode segmentation, i.e. the spacing between the wires in
896 the sense planes [45]. The off-line combination of the 2-D information on the wire
897 planes with the timing information allows for the 3D reconstruction of the event in
898 the chamber.

899 Since the charge deposited by the ionizing radiation is proportional to the de-
900 posited energy and the charge collected on the sense plane is a function of the de-
901 posited charge, LArTPCs allow the measurement of the energy deposit in the active
902 volume. Effects due to the presence of free charge and impurities in the active vol-
903 ume, such as a finite electron lifetime, recombination and space charge, complicate
904 the relationship between deposited and collected charge affecting the measurement of
905 the particle’s energy, as described in the next section.

906 **2.1.3 Liquid Argon: Ionization Charge**

907 The mean rate of energy loss by moderately relativistic elementary charge particles
 908 heavier than electrons is well described by the modified Bethe-Bloch [101] equation

$$-\frac{dE}{dx} = K z^2 \frac{Z}{A} \varrho \frac{1}{\beta^2} \left[\frac{1}{2} \ln \frac{2m_e c^2 \beta^2 \gamma^2 T_{max}}{I^2} - \beta^2 - \frac{\delta}{2} \right], \quad (2.1)$$

909 where z is the number of unit charge of the ionizing radiation, Z , A and ϱ are the
 910 atomic number, mass number and density of the medium, m_e is the electron mass,
 911 $\gamma = \frac{\beta}{\sqrt{1-\beta^2}}$ is the Lorentz factor of the ionizing radiation, T_{max} is the maximum kinetic
 912 energy which can be imparted to a free electron in a single collision, I is the mean
 913 excitation energy on eV, δ is the density correction and $K = 0.307075 \text{ MeV g}^{-1} \text{ cm}^2$ is
 914 a numerical conversion factor. The Bethe-Bloch treats the energy loss by an ionizing
 915 radiation via quantum-mechanical collisions producing ionization or an excitation in
 916 the medium as an uniform and continuous process. The density correction terms
 917 becomes relevant for incident particle with high energy, where screening effects due
 918 to the polarization of the medium by high energy particles occur.

919 Excitation and ionization of the detector medium occur in similar amounts. Since
 920 the ionizing collisions occur randomly, we can parametrize their number k in a segment
 921 of length s along the track with a Poissonian function

$$P(k) = \frac{s^k}{k! \lambda^k} e^{-s/\lambda}, \quad (2.2)$$

922 where $\lambda = 1/N_e \sigma_i$, with N_e being the electron density of σ_i the ionization cross-
 923 section per electron. About 66% of the ionizing collisions in Argon produce only
 924 a single electron/ion pair [77]; in the other cases, the transferred kinetic energy is
 925 enough for the primary electron to liberate one or more secondary electrons, which
 926 usually stay close to the original pair. Occasionally, electrons can receive enough

927 energy to be ejected with high energy, forming a so-called “ δ -ray”: a detectable short
928 track off the particle trajectory, as shown in figure 2.3. The average number of δ -ray
929 with energy $E > E_0$ per cm follows the empirical form

$$P(E > E_0) \sim \frac{y}{\beta^2 E_0}, \quad (2.3)$$

930 where y is an empirical factor depending on the medium (0.114 for gaseous Ar), and
931 β is v/c .

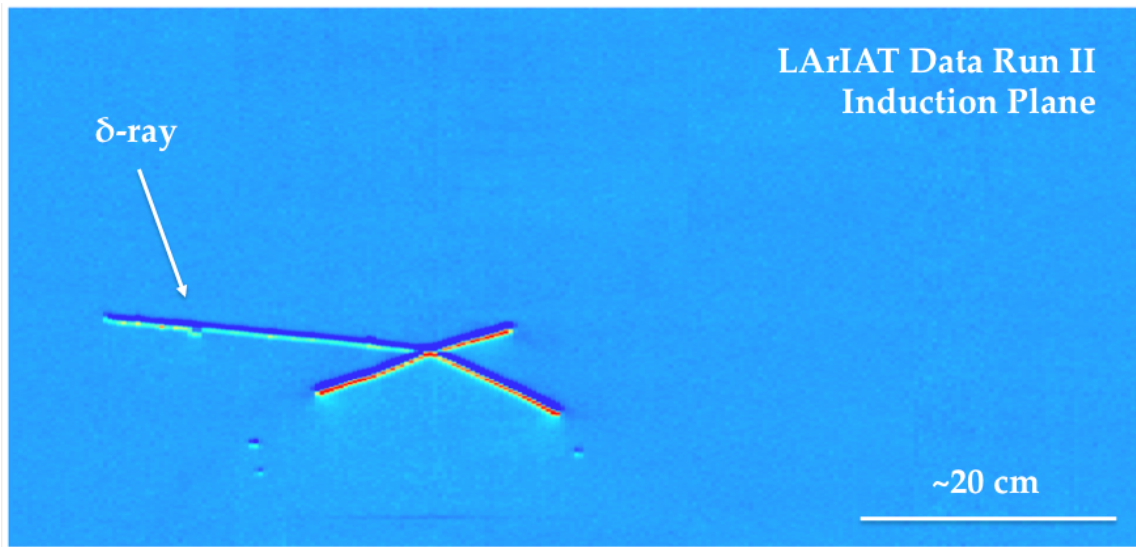


Figure 2.3: Events display for a LArIAT pion absorption candidate on the induction plane, with highlighted delta ray.

932 Purity & Electron Life Time

933 The presence of electronegative contaminants in liquid argon, such as oxygen O_2
934 and water H_2O , is particularly pernicious, since these molecules quench the charge
935 produced by the ionizing radiation. Thus, amount of charge per unit of length dQ/dx
936 collected on the collection plane depends on the charge's production point in the
937 detector: ionization produced close to the cathode will see more impurities along its
938 journey to the collection plane than ionization produced close to the anode, resulting

939 in greater attenuation of its charge. As a result, the amount of charge collected on
 940 the sense wires as a function of the traveled distance follows an exponential decay
 941 trend. The traveled distance is generally measured in terms of drift time and the
 942 characteristic time constant of the exponential decay is called electron lifetime τ_e .
 943 Figure 2.4 shows the typical life time for LArIAT data. The procedure to measure
 944 the electron lifetime in LArIAT is outlined in [104]. LArIAT small drift distance (47
 945 cm) allows for a relatively short electron life time. The life time for bigger detectors
 946 such as MicroBooNE, whose drift distance is 2.6 m, needs to be of the order of
 947 tens of milliseconds to allow a charge collection usable for physics analyses. Energy
 948 reconstruction in LArTPC applies a correction for the finite lifetime to calibrate the
 949 detector calorimetric response; details for LArIAT are provided in Section C.

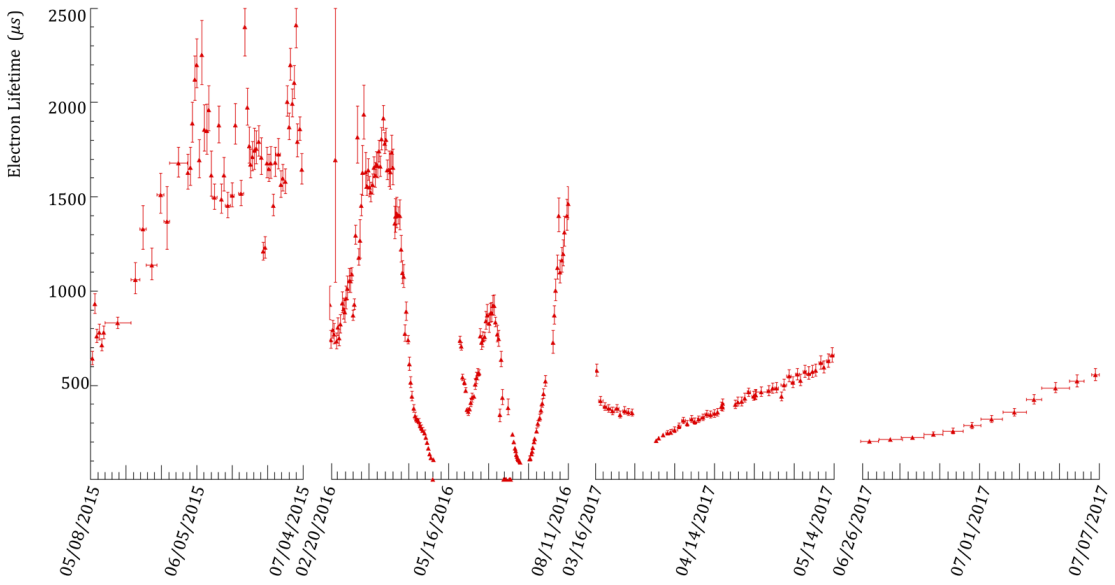


Figure 2.4: Electron lifetime during the LArIAT run period [43].

950 LArTPCs use hermetically sealed and leak-checked vessels to abate the leakage
951 and diffusion of contaminants into the system. The liquid argon filling of the volume
952 occurs after the vessel is evacuated or purged with gaseous argon [10] to reduce re-
953 maining gases in the volume. Even so, the construction of a pure tank of argon is
954 unviable, as several sources of impurity remain. In particular, impurities can come
955 from the raw argon supply, the argon filtration system and from the outgassing from
956 internal surfaces. Outgassing is a continuous diffusive process producing contami-
957 nants, especially water, even after the vessel is sealed, particularly from materials in
958 the ullage region². Since research-grade argon comes from the industrial distillation
959 of air, the impurities with the highest concentration are nitrogen, oxygen and water,
960 generally maintained under the 1 part per million level by the vendor. Even so, a
961 higher level of purity is necessary to achieve a free electron life time usable in meter
962 scale detectors. Thus, argon is constantly filtered in the cryogenic system, which
963 reduce the oxygen and water contamination to less than 100 parts per trillion. The
964 filtration system depends on the size and drift distance of the experiment and, for
965 experiments on several meters scale, it includes an argon recirculation system.

966 Recombination Effect

967 After production, ionization electrons thermalize with the surrounding medium and
968 may recombine with nearby ions. Recombination might occur either between the
969 electron and the parent ion through Coulomb attraction, as described in the geminate
970 theory [99], or thanks to the collective charge density of electrons and ions from
971 multiple ionizations in a cylindrical volume surrounding the particle trajectory, as
972 described in the columnar model [80]. Consideration on the average electron-ion
973 distance and the average ion-ion distance for argon show that the probability of

2. While the liquid argon low temperature reduces outgassing in the liquid, this process remains significant for absorptive material (such as plastic) above the surface of the liquid phase.

974 geminate recombination is low; thus recombination in argon is mainly due to collective
975 effects [5]. Since protons, kaons and stopping particles present a higher ionization
976 compared to MIPs, recombination effects are more prominent when considering the
977 reconstruction of energy deposited by these particles.

978 Theoretical descriptions of recombination based on the Birks model and the Box
979 model are provided in [29] and [112], respectively. The Birks model assumes a gaus-
980 sian spatial distribution around the particle trajectory during the entire recombina-
981 tion phase and identical charge mobility for ions and electrons. The Box model also
982 assumes that electron diffusion and ion mobility are negligible in liquid argon during
983 recombination. In these models, the fraction of ionization electrons surviving recom-
984 bination is a function of the number of ion-electron pairs per unit length, the electric
985 field, the average ion-electron separation distance after thermalization and the angle
986 of the particle with respect to the direction of the electric field – plus the diffusion
987 coefficient in the Birks model. Given the stringent assumptions, it is perhaps not sur-
988 prising that these models are in accordance to data only in specific regimes: the Birks
989 model is generally used to describe recombination for low dE/dx , the Box model for
990 high dE/dX . In LArTPC, the ICARUS and ArgoNeut experiments have measured
991 recombination in [16] and [5] respectively. Since LArIAT uses the refurbished Ar-
992 goNeut TPC and cryostat at the same electric field, LArIAT currently corrects for
993 recombination using the ArgoNeut measured recombination parameters in [5].

994 Space Charge Effect

995 Slow-moving positive argon ions created during ionization can build-up in LArTPC,
996 causing the distortion of the electric field within the detector. This effect, called
997 “space charge effect” leads to a displacement in the reconstructed position of the
998 signal ionization electrons. In surface LArTPCs the space charge effect is primarily
999 due to the rate of ionization produced by cosmic rays which is slowly drifting in the

1000 chamber at all times. Surface LArTPC of the size of several meters are expected
1001 to be modestly impacted from the space charge effect, where charge build-up create
1002 anisotropy of the electric field magnitude of the order of 5% at a drift field of 500
1003 V/cm [93]. The smallness of the LArIAT drift volume and its relatively high electric
1004 field are such that the effect of space charge is expected to be negligible.

1005 2.1.4 Liquid Argon: Scintillation Light

1006 Liquid argon emits scintillation light at the passage of charged particles. LArTPCs
1007 leverage this property to determine when the ionization charge begins to drift towards
1008 the anode plane.

1009 Scintillation Process

1010 Scintillation light in argon peaks in the ultraviolet at a 128 nm, shown in comparison
1011 to Xenon and Kypton in Figure 2.5, from [94]. The light yield collected by the optical
1012 detector depends on the argon purity, the electric field, the dE/dx and particle type,
1013 averaging at the tens of thousands of photons per MeV.

1014 The de-excitation of Rydberg dimers in the argon is responsible for the scintillation
1015 light. Rydberg dimers exist in two states: singlets and a triplets. The time constant
1016 for the singlet radiative decay is 6 ns, resulting in a prompt component for the scin-
1017 tillation light. The decay of the triplet is delayed by intersystem crossing, producing
1018 a slow component with a time constant of \sim 1500 ns. “Self-trapped exciton lumines-
1019 cence” and “recombination luminescence” are the two processes responsible for the
1020 creation of the Rydberg dimers [83]. In the first process, a charged particle excites an
1021 argon atom which becomes self-trapped in the surrounding bulk of argon, forming a
1022 dimer; the dimer is in the singlet state 65% of the times and in the triplet state 35%
1023 of the times. In case of recombination luminescence, the charged particle transfers
1024 enough energy to ionize the argon. The argon ion forms a charged argon dimer state,

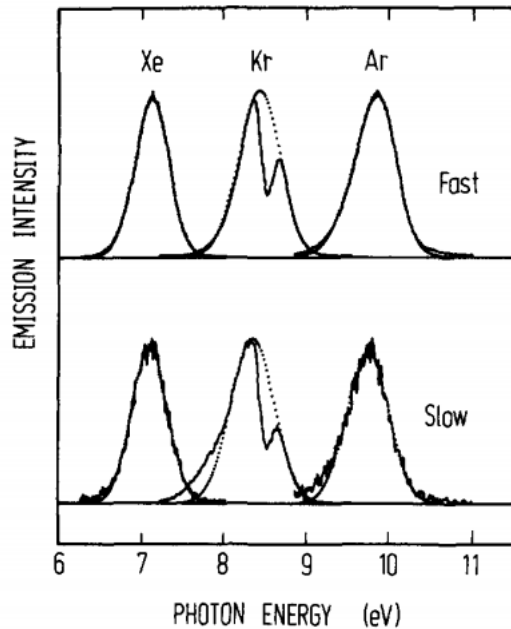


Figure 2.5: Emission spectra of the fast and slow emission components in Xenon, Krypton and Argon according to [94]. The dotted lines correspond to the Gaussian fits.

which quickly recombines with the thermalized free electron cloud. Excimer states are produced in the recombination, roughly half in the singlet and half in the triplet state. The light yield dependency on the electric field, on the dE/dx and particle type derives from the role of free charge in the recombination luminescence process. The spacial separation between the argon ions and the free electron cloud depends on the electric field. On one hand, a strong electric field diminishes the recombination probability, leading to a smaller light yield; on the other, it increases the free charge drifting towards the anode plane. Hence, the amount of measurable charge and light anti-correlates as a function of the electric field. Ionizing particles in the argon modify the local density of both free electrons and ions depending on their dE/dx . Since the recombination rate is proportional to the square of the local ionization density, highly ionizing particles boost recombination and the subsequent light yield compared to MIPs. The possibility to leverage this dependency for pulseshape-based particle identification has been shown in [31, 88].

1039 **Effects Modifying the Light Yield**

1040 The production mechanism through emission from bound excimer states implies that
1041 argon is transparent to its own scintillation light. In fact, the photons emitted from
1042 these metastable states are not energetic enough to re-excite the argon bulk, greatly
1043 suppressing absorption mechanisms. In a LArTPC however, several processes modify
1044 the light yield in between the location where light is produced and the optical detector.
1045 In a hypothetical pure tank of argon, Rayleigh scattering would be the most important
1046 processes modifying the light yield. Rayleigh scattering changes the path of light
1047 propagation in argon, prolonging the time between light production and detection.
1048 The scattering length has been measured to be 66 cm [78] , shorter than the theoretical
1049 prediction of ~ 90 cm [111]; this value is short enough to be relevant for the current
1050 size of LArTPCs detectors. In fact, Rayleigh scattering worsen the resolution on t_0 ,
1051 the start time for charge drifting, and alters the light directionality, complicating the
1052 matching between light and charge coming from the same object in case of multiple
1053 charged particles in the detector.

1054 Traces of impurities in argon such as oxygen, water and nitrogen also affect the
1055 light yield, mainly via absorption and quenching mechanisms. Absorption occurs as
1056 the interaction of a 128 nm photon directly with the impurity dissolved in the liquid
1057 argon. Differently, quenching occurs as the interaction of an argon excimer and an
1058 impurity, where the excimer transfers its excitation to the impurity and dissociates
1059 non-radiatively. Given this mechanism, it is evident how quenching is both a function
1060 of the impurity concentrations and the excimer lifetime. Since the triplet states
1061 live much longer than the singlet states, quenching occurs mainly on triplet states,
1062 affecting primarily the slow component of the light, reducing the scintillation yield
1063 and a shortening of the scintillation time constants.

1064 The stringent constraints for the electron life time limit the presence of oxygen and
1065 water to such a low level that both absorption and quenching on these impurity is not

1066 expected to be significant. Contrarily, the nitrogen level is not bound by the electron
1067 life time constraints – nitrogen being an inert gas, expensive to filter. Thus, nitrogen
1068 is often present at the level provided by the vendor. The effects of nitrogen on argon
1069 scintillation light have been studied in the WArP R&D program and at several test
1070 stands. The quenching process induced by nitrogen in liquid Ar has been measured
1071 to be proportional to the nitrogen concentration, with a rate constant of ~ 0.11
1072 μs^{-1} ppm $^{-1}$; appreciable decreasing in lifetime and relative amplitude of the slow
1073 component have been shown for contamination as high as a few ppm of nitrogen [6].
1074 For a nitrogen concentration of 2 parts per million, typical of the current generation
1075 of LArTPC, the attenuation length due to nitrogen has been measured to be ~ 30
1076 meters [82].

1077 **Wavelength Shifting of LAr Scintillation Light**

1078 Liquid argon scintillation light is invisible for most optical detectors deployed in a
1079 LArTPC, such as cryogenic PMTs and SiPMs, since a wavelength of 128 nm is gen-
1080 erally too short to be absorbed from most in glasses, polymers and semiconductor
1081 materials. Research on prototype SiPMs absorbing directly VUV light and their
1082 deployment in noble gasses experiment is ongoing but not mature [120]. Thus, ex-
1083 periments need to shift the wavelength of scintillation light to be able to detect it.
1084 Albeit deployed in different ways, neutrinos and dark matter experiments commonly
1085 use 1,1,4,4-tetraphenyl-butadiene (TPB) to shift the scintillation light. TPB absorbs
1086 the vacuum ultraviolet (VUV) light and emits in the visible at ~ 425 nm [33], with
1087 a ratio of visible photon emitted per VUV photon absorbed of $\sim 1.2:1$ [66].

1088 Neutrino experiments typically coat their optical detector system evaporating a
1089 layer of TPB either directly on the PMTs glass surface or on acrylic plates mounted in
1090 front of the PMTs [60]; this technique allows the fast detection light coming directly
1091 from the neutrino interaction. Dark matter experiments typically evaporate TPB on

reflective foils mounted on the inside walls of the sensitive volume and detect the light after it has been reflected; this technique leads to a higher and more uniform light yield, though scattering effects for both the visible and VUV light augment the propagation time and hinder directionality information [61]. In order to take advantage of both these techniques, hybrid systems with PMT coating and foils are being considered for the next generation of large neutrino detectors.

2.1.5 Signal Processing and Event Reconstruction

In this section we illustrate the processing and reconstruction chain of the TPC signals, from the pulses on the sense wire to the construction of three dimensional objects with associated calorimetry. Different experiments can chose different software packages for their off line signal processing and event reconstruction, but a popular choice for US based LArTPCs is LArSoft [40]. Based on the Art framework [72], LArSoft is an event-based toolkit to perform simulation, analysis and reconstruction of LArTPCs events.

1106

LArTPC signal processing develops in several consecutive stages that we summarize here in the following categories: *Deconvolution*, *Hit Reconstruction*, *2D Clustering*, *3D Tracking*, *Calorimetry Reconstruction*. A visualization of the signal processing workflow is shown in figure 2.6.

1111

Deconvolution. Induction and collection planes have different field responses, given the different nature of the signals on these planes: the wires on the induction planes see the inductive signal of the drifting charge, while the wires on the collection planes see the current derived from the charge entering the conductor. Thus, signals on the induction plane are bi-polar pulse and signal on the collection plane are unipolar pulses, see Figure 2.6 panel a). The first step in signal processing is deconvolution,

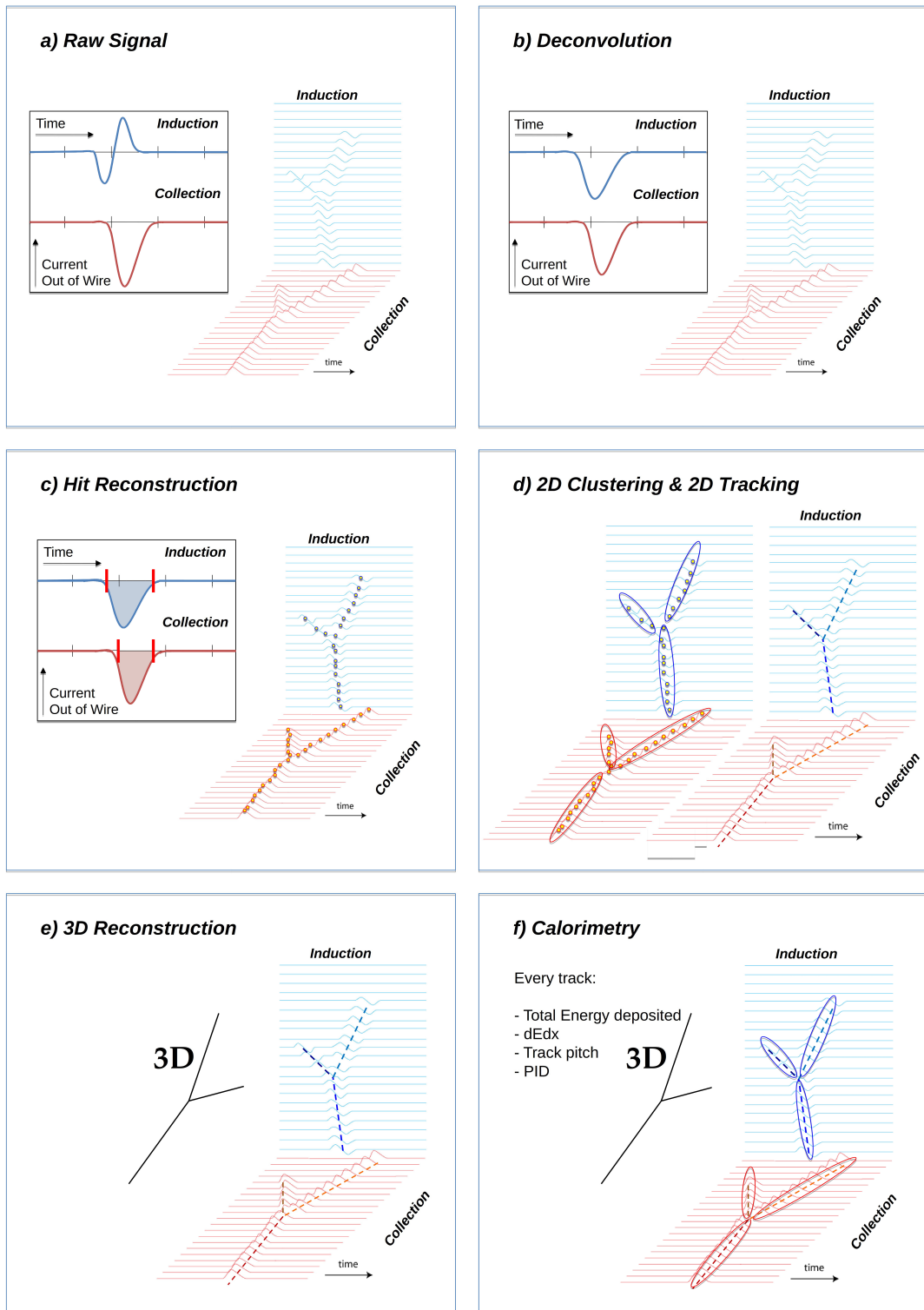


Figure 2.6: A scheme of a typical signal processing workflow in LArSoft.

1118 that is a series of off-line algorithms geared towards undoing the detector effects. The
1119 result of the deconvolution step is the production of a comparable set waveforms on
1120 all planes presenting unipolar, approximately gaussian-like pulses (Figure 2.6 panel
1121 b). Signal from all planes are treated on equal footage beyond this point. Some
1122 LArTPC apply noise filtering in the frequency domain just after the deconvolution
1123 to clean up wire cross talk. Since signals from the LArIAT TPC are extremely clean,
1124 noise filtering is not necessary.

1125

1126 **Hit Reconstruction.** The second stage of the signal processing is the recon-
1127 struction of hits, indicating an energy deposition in the detector. A peak finder scans
1128 the deconvolved TPC waveforms for each wire on the whole readout time looking for
1129 spikes above the waveform’s baseline. It then fits these peaks with gaussian shapes
1130 and stores the fit parameters such as the quality of the fit, the peak time, height and
1131 area under the gaussian fit. The information resulting from this process on a single
1132 spike form a single reconstructed “hit”, see Figure 2.6 panel c). The next steps in
1133 the event reconstruction chain will then decide if rejecting hits with poor fits. It is
1134 important to notice how the height and width of the hit depend on the topology of
1135 the event: for example, a particle running parallel to the wire planes will leave a series
1136 of sharp hits on many consecutive wires, while a particle traveling towards the planes
1137 will leave a long, wide hit on very few wires. The height of the hits and their integral
1138 is proportional to the charge collected on the wire, so it depends on the particle type.

1139

1140 The event reconstruction chain uses collection of hits to form more complex objects
1141 associated with the particles in the detector. The development of different approaches
1142 to accomplish this task is an extremely hot topic in LArTPC event reconstruction
1143 which spans from more traditional approaches such as line-clustering [26] to the use of
1144 machine learning tools [59]. Generally speaking, the scope of hit clustering and event

1145 reconstruction to provide shower-like or track like-objects with an associated energy
1146 reconstruction. This is because different particles have different topology in the de-
1147 tector – electrons and photon create electromagnetic showers, resulting in shower-like
1148 topologies, while muons and hadrons leave track-like signals. For the scope of these
1149 thesis, we will describe only LArIAT’s approach to track reconstruction even if we
1150 recognize the breath of LArTPC event reconstruction is much wider. We are inter-
1151 ested in the reconstruction of pions and kaons in the active volume, whose topology
1152 is track-like.

1153

1154 **2D Clustering Reconstruction.** The LArIAT reconstruction of track-like ob-
1155 jects starts by clustering hits on the collection and induction planes separately with
1156 the use of the TrajCluster clustering package [25]. TrajCluster looks for a collection
1157 of hits in the wire-time 2D space which can be described with a line-like 2D trajec-
1158 tory. TrajCluster reconstructs trajectories by adding trajectory points to the leading
1159 edge of the trajectory while stepping through the 2D space of hits. Several factors
1160 determine whether a hit is added to the trajectory, including but not limited to

- 1161 1. the goodness of the fit of the single hit,
- 1162 2. the charge of the hit compared to the average charge and RMS of the hits
1163 already forming the trajectory,
- 1164 3. the goodness of trajectory fit with and without the hit addition,
- 1165 4. the angle between the two lines formed by the collection of hits before and after
1166 the considered hit in the trajectory.

1167 The final product of this reconstruction stage is the collection of bidimensional clusters
1168 on each wire plane, see Figure 2.6 panel d).

1169 **3D Tracking.** The 3D tracking set of algorithms uses clusters close in time on
1170 the induction and collection planes as starting point to form a 3D track. Firstly, it

1171 construct a tentative 3D trajectory using the edges of the clusters. Then, it projected
1172 back the tentative trajectory on to the planes and adjusts the parameters of the 3D
1173 track fit such that they minimize the distance between the fit projections and the
1174 track hits in all wire planes simultaneously. Tridimensional tracking can use multiple
1175 clusters in one plane, but it can never break them in smaller groups of hits. This
1176 algorithm was first developed for the ICARUS collaboration [20]. The final product
1177 of this reconstruction stage is the formation of tridimensional objects in the TPC
1178 active volume, see Figure 2.6 panel e).

1179

1180 **Calorimetry.** The last step in the event reconstruction chain is to assign calorimetric
1181 information to the track (or shower) objects. Calorimetry is performed separately
1182 on the different planes. A multi-step procedure is needed to retrieve the energy
1183 deposited in the TPC from the charge seen by the wires. For each hit associated with
1184 the track object, the calorimetry algorithms calculate the charge seen on every wire
1185 using the area underneath the gaussian fit; then, they correct this raw charge by the
1186 electron life time, the electronic noise on the considered wire and the recombination
1187 effect. Lastly an overall calibration of the energy, explained in detail in section C,
1188 is applied and the calorimetric information for the given track is assigned. Even if
1189 calorimetry is done in 2D, it benefits from the 3D tracking information; typical information
1190 available after the calorimetric reconstruction are the total energy deposited
1191 by the particle and its stopping power dE/dx at each “track pitch”, i.e. at each 2D
1192 projection on the wire plane of the 3D trajectory.

1193 2.2 The Intensity Frontier Program

1194 This section highlights the role of Liquid Argon Time Projection Chambers at the
1195 Intensity frontier. In particular, we show the prospects for the exploration of neutrino

1196 physics (Section 2.2.1) and GUT models (Section 2.2.2) in current and forthcoming
1197 LAr experiments. In Section , we introduce LArIAT and its role in the Intensity
1198 Frontier panorama.

1199 **2.2.1 Prospects for LArTPCs in Neutrino Physics: SBN and**
1200 **DUNE**

1201 The ArgoNeut experiment [17] together the LAr R&D experiments TallBo and the
1202 Yale TPC initiated the US LArTPC neutrino program. Following the success of the
1203 ArgoNeut small TPC on the NuMI beam, a wide program of LArTPCs on neutrino
1204 beams has flourished. The construction of LArTPCs as near and far detectors at
1205 different baseline allows for the exploration of some of the fundamental questions in
1206 neutrino physics today illustrated in section 1.3.1.

1207 The Short-Baseline Neutrino (SBN) [21] program at Fermilab is tasked with con-
1208 clusively assess the nature of the “LSND and MiniBooNE anomalies” [14, 15, 23],
1209 resolving the mystery of sterile neutrinos at the eV² scale. The SBN program entails
1210 three surface LArTPCs positioned on the Booster Neutrino Beam at different dis-
1211 tances from the neutrino production in oder to fully exploit the L/E dependence of
1212 the oscillation pattern: SBND (100 m from the decay pipe), MicroBooNE (450 m),
1213 and ICARUS (600 m). Within the oscillation context, the choice of the LArTPC tech-
1214 nology for the SBN detectors changes the set of systematics with respect to LSND
1215 and MiniBooNE, whose detection techniques were both based on Cherenkov light.
1216 In particular, LArTPCs provide excellent electron/photon separation [9] lacking in
1217 Cherenkov detectors which can be leveraged to abate the photon background from
1218 neutral current interactions in ν_e searches. MicroBooNE [8], the first detector of the
1219 SBN program to be fully operational, started its first neutrino run in October 2015.
1220 MicroBooNE is a 89 ton active volume LArTPC, single drift chamber with TPC di-
1221 mensions of 2.6 m (drift) x 2.3 m (heigh) x 10.4 m (depth). MicroBooNE is positioned

at a very similar L/E on the Booster neutrino beam as MiniBooNE has the scope to directly cross check the MiniBooNE oscillation measurement. In case MicroBooNE confirms the presence of the “low energy excess” anomaly, SBND and ICARUS will provide the full measurement of the oscillation parameters. SBND and ICARUS are both dual drift chambers, whose active volume is respectively 112 ton and 600 ton. ICARUS is scheduled to become operational by the end of 2018 and SBND shortly after. Besides the oscillation analysis, the second main goals of SBN is to perform an extensive campaign of neutrino cross section measurements in argon. Given the importance of nuclear effects in (relatively) heavy materials, as discussed in section 1.2.3, both the oscillation analysis of the SBN program and the measurements of neutrino properties in DUNE will benefit from such a campaign.

On a different neutrino beam and baseline, the DUNE experiment, née LBNE [11], is the flagship experiment on the medium-long term of US-based neutrino physics, scheduled to start data taking in 2026. Shooting neutrinos from Fermilab for 800 miles to the SURF laboratory in South Dakota, DUNE is tasked with performing conclusive measurements of CP violation in the lepton sector, the neutrino mass ordering and the θ_{23} octant. The DUNE far detector will count four 10 kton LArTPCs, roughly of dimensions of 19 m (horizontally) x 18 m (vertically) x 66 m (depth).

2.2.2 Prospects for LArTPCs in GUT Physics: DUNE

The experimental exploration of a manifestation of Grand Unified Theory is possible in DUNE thanks to its sheer mass. In particular, proton decay searches are a capital topic of DUNE’s wide non-accelerator physics program. The key elements for a rare decay experiment are: massive active volume, long exposure, high identification efficiency and low background. Figure 2.7 shows the current best experimental limits on nucleon decay lifetime over branching ratio (dots). Historically, the dominant technology used in these searches has been water Cherenkov detectors: all the best

1248 experimental limits on every decay mode are indeed set by Super-Kamiokande [?, ?].
 1249 As shown in section 1.3.2, different family of GUTs predict the proton to decay in
 1250 different modes. In particular, SUSY flavored GUTs prefer the presence of kaons
 1251 in the decay products, e.g. $p \rightarrow K^+ \bar{\nu}$. It is particularly important to notice that
 1252 the kaon energy for the proton decay mode $p \rightarrow K^+ \bar{\nu}$ is under Cherenkov threshold
 1253 in water. Thus, Super-Kamiokande set the limit on the lifetime for the $p \rightarrow K^+ \bar{\nu}$
 1254 mode by relying on photons from nuclear de-excitation and on the muon tagging in
 1255 the kaon decay leptonic mode. For this reason, an attractive alternative approach to
 1256 identifying nucleon decay is the use of a LArTPCs, where the kaon is directly visible
 1257 in the detector. According to [11], DUNE will have an active volume large enough,
 1258 have sufficient shielding from the surface, and will run for lengths of time sufficient
 1259 to compete with Hyper-K, opening up the opportunity for the discovery of nucleon
 1260 decay.

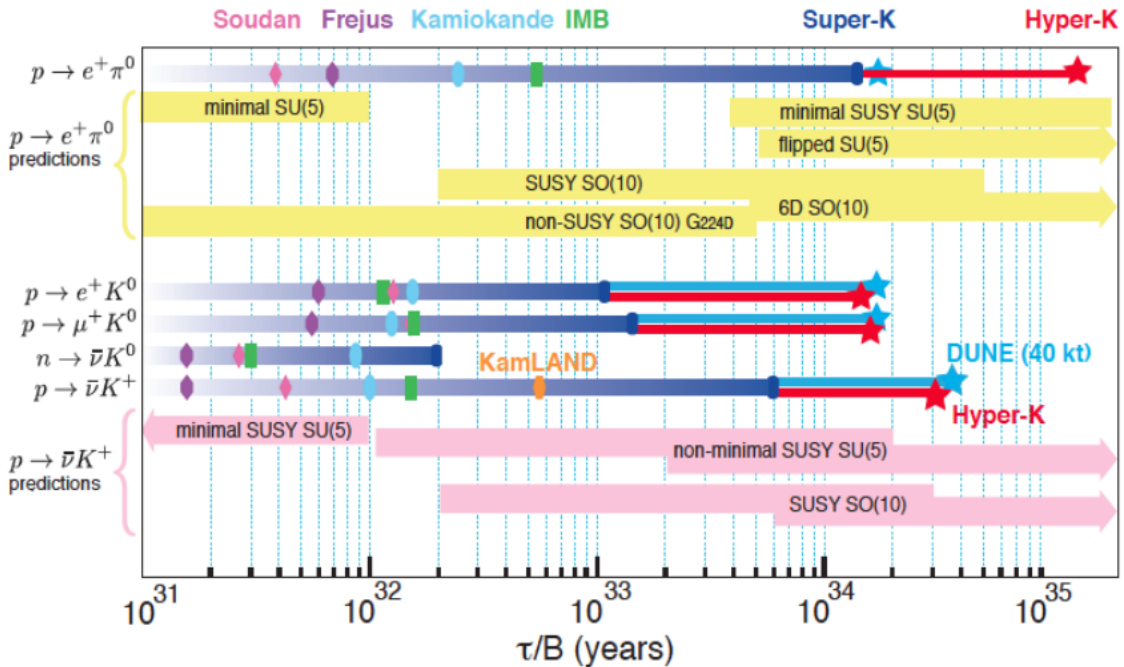


Figure 2.7: Proton decay lifetime limits from passed and future experiments.

1261 2.2.3 Enabling the next generation of discoveries: LArIAT

1262 LArIAT, a small LArTPC in a test beam, is designed to perform an extensive physics
1263 campaign centered on charged particle cross section measurements while characteriz-
1264 ing the detector performance for future LArTPCs. Since LArTPCs represent the most
1265 advanced experiments for physics at the Intensity Frontier, their complex technology
1266 needs a thorough calibration and dedicated measurements of some key quantities to
1267 achieve the precision required for the next generation of discoveries. LArIAT’s goal
1268 is to provide such calibration and dedicated measurements. The LArIAT LArTPC is
1269 deployed in a dedicated calibration test beamline at Fermilab. We use the LArIAT
1270 beamline to characterize the charge particles before they enter the TPC: the particle
1271 type and initial momentum is known from beamline information. The precise calori-
1272 metric energy reconstruction of the LArTPC technology enables the measurement of
1273 the total differential cross section for tagged hadrons. The Pion-Nucleus and Kaon-
1274 Nucleus total hadronic interaction cross section have never been measured before in
1275 argon and they are a fundamental step to shed light on light meson interaction in nu-
1276 clei per se, while providing a key input to neutrino physics and proton decay studies
1277 in future LArTPC experiments like SBN and DUNE.

1278 In order to showcase LArIAT’s utility to SBN and DUNE, we illustrate briefly
1279 two comparisons as examples: one regarding neutrino interactions and the second
1280 regarding proton decay studies.

1281 The left side of figure 2.8 shows the distribution of products in momentum spectrum
1282 and particle type as simulated in a ν_e CC interaction in DUNE (according to [87]);
1283 the range of these distribution is to compare with the momentum distribution of
1284 light particles in the LArIAT beamline – shown on the right side of figure 2.8. The
1285 momentum spectrum in the LArIAT beamline for electrons, muons and pions – the
1286 most abundant particles produced in a ν_e CC interaction – covers a wide range of the
1287 expected momentum distribution in a neutrino event.

1288 The signature of a proton decay event in the “LAr golden mode” is the presence of
 1289 a single kaon of about 400 MeV in the detector; the momentum spectrum of the kaon
 1290 pre and post FSI in such an event as simulated by GENIE is shown on the left side
 1291 of figure 2.9. The right side of figure 2.9 shows the momentum spectrum of kaons in
 1292 the LArIAT beamline. Kaons arriving to the LArIAT TPC are ideal for proton decay
 1293 studies, since their momentum in the beamline is just above the typical momentum
 1294 for kaons in a proton decay event: the majority of LArIAT kaons slow down in the
 1295 TPC enough to enter the desired momentum window.

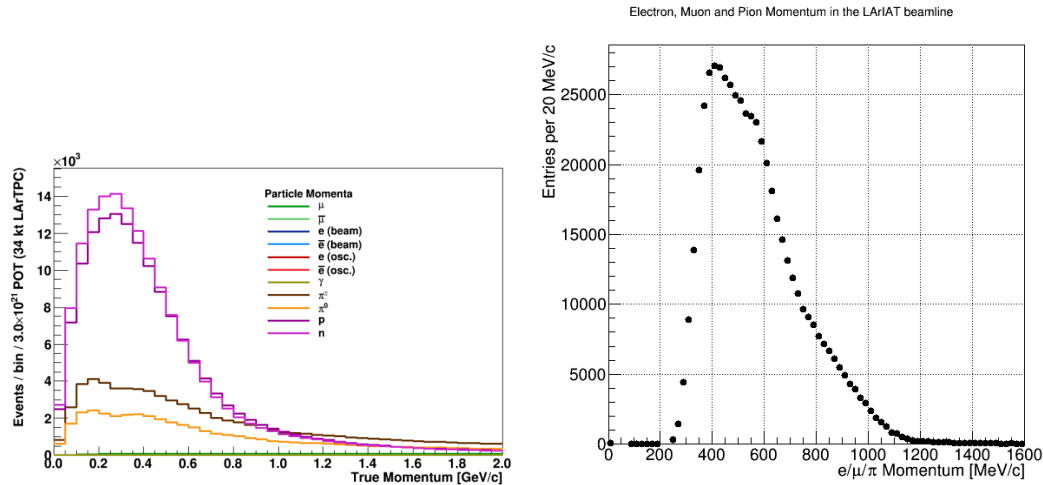


Figure 2.8: *Left.* Simulation of the products of a ν_e CC interaction in DUNE, both in particles type and momentum.
Right. Momentum spectrum for low mass particles (e, μ, π) in the LArIAT beamline, negative tune, Run II, Picky Tracks see section 3.2.2.

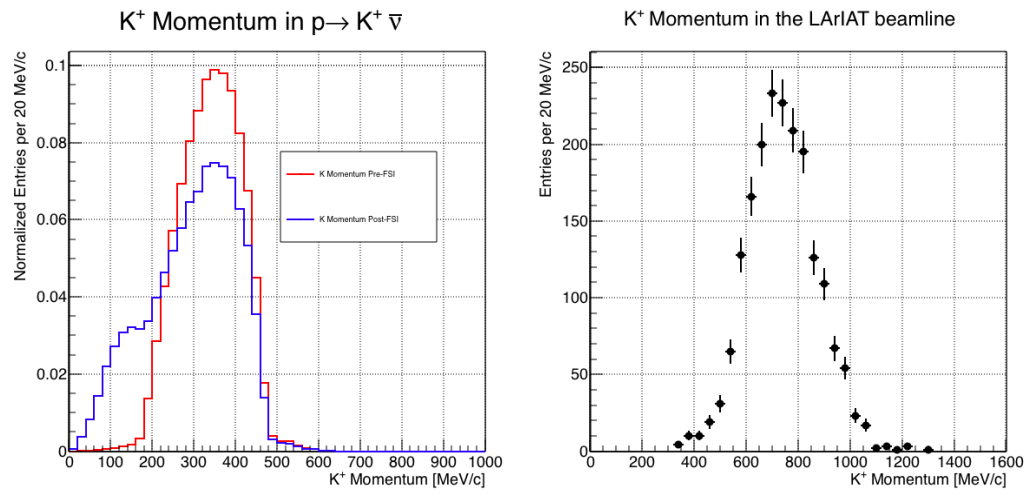


Figure 2.9: *Left.* Momentum of the kaon outgoing a proton decay $p \rightarrow K^+ \bar{\nu}$ event as simulated by the Genie 2.8.10 event generator in argon. The red line represents the kaon momentum distribution before undergoing the simulated final state interaction inside the argon nucleus, while the blue line represents the momentum distribution after FSI.

Right. Positive Kaon momentum spectrum in the LArIAT beamline, positive tune, Run II, Picky Tracks see section 3.2.2.

₁₂₉₆ **Chapter 3**

₁₂₉₇ **LArIAT: Liquid Argon In A
₁₂₉₈ Testbeam**

₁₂₉₉ “*But, hey we need to be somewhat foolish...*”
₁₃₀₀ – Agnes Obel, 2010 –

₁₃₀₁ In this chapter, we describe the LArIAT experimental setup. We start by illus-
₁₃₀₂ trating the journey of the charged particles in the Fermilab accelerator complex, from
₁₃₀₃ the gaseous thermal hydrogen at the Fermilab ion source to the delivery of the LAr-
₁₃₀₄ IAT tertiary beam at MC7. We then describe the LArIAT beamline detectors, the
₁₃₀₅ LArTPC, the DAQ and the monitoring system.

₁₃₀₆ **3.1 The Particles’ Path to LArIAT**

₁₃₀₇ LArIAT’s particle history begins in the Fermilab accelerator complex with a beam of
₁₃₀₈ protons. The process of proton acceleration develops in gradual stages (see picture
₁₃₀₉ 3.1): gaseous hydrogen is ionized in order to form H^- ions; these ions are boosted
₁₃₁₀ to 750 keV by a Cockcroft-Walton accelerator and injected into the linear accelerator
₁₃₁₁ (Linac) that increases their energy up to 400 MeV; then, H^- ions pass through a

1312 carbon foil and lose the two electrons; the resulting protons are then injected into a
1313 rapid cycling synchrotron, called the Booster; at this stage, protons reach 8 GeV of
1314 energy and are compacted into bunches; the next stage of acceleration is the Main
1315 Injector, a synchrotron which accelerates the bunches up to 120 GeV; in the Main
1316 Injector, several bunches are merged into one and are ready for delivery.

1317 The Fermilab accelerator complex works in supercycles of 60 seconds in duration.
1318 A 120 GeV primary proton beam with variable intensity is extracted in four-second
1319 “spills” and sent to the Meson Center beam line.

1320 LArIAT’s home at Fermilab is the Fermilab Test Beam Facility (FTBF), where
1321 the experiment characterizes a beam of charged particles in the Meson Center beam
1322 line. At FTBF, the primary beam is focused onto a tungsten target to create LAr-
1323 IAT’s secondary beam. The secondary beamline is set such that the composition of
1324 the secondary particle beam is mainly positive pions. The momentum peak of the
1325 secondary beam was fixed at 64 GeV/c for the LArIAT data considered in this work,
1326 although the beam is tunable in momentum between 8-80 GeV/c; this configuration
1327 of the secondary beamline assured a stable beam delivery at the LArIAT experimental
1328 hall.

1329 The secondary beam impinges then on a copper target within a steel collimator
1330 inside the LArIAT experimental hall (MC7) to create the LArIAT tertiary beam,
1331 (shown in Fig. 3.2). The steel collimator selects particles produced with a 13° pro-
1332 duction angle. The particles are then bent by roughly 10° through a pair of dipole
1333 magnets. By configuring the field intensity of the magnets we allow the particles of
1334 LArIAT’s tertiary beam to span a momentum range from 0.2 to 1.4 GeV/c. The
1335 polarity of the magnet is also configurable and determines the sign of the beamline
1336 particles which are focused on the LArTPC. If the magnet polarity is positive the
1337 tertiary beam composition is mostly pions and protons with a small fraction of elec-
1338 trons, muons, and kaons. It is the job of the LArIAT beamline equipment to select the

Fermilab Accelerator Complex

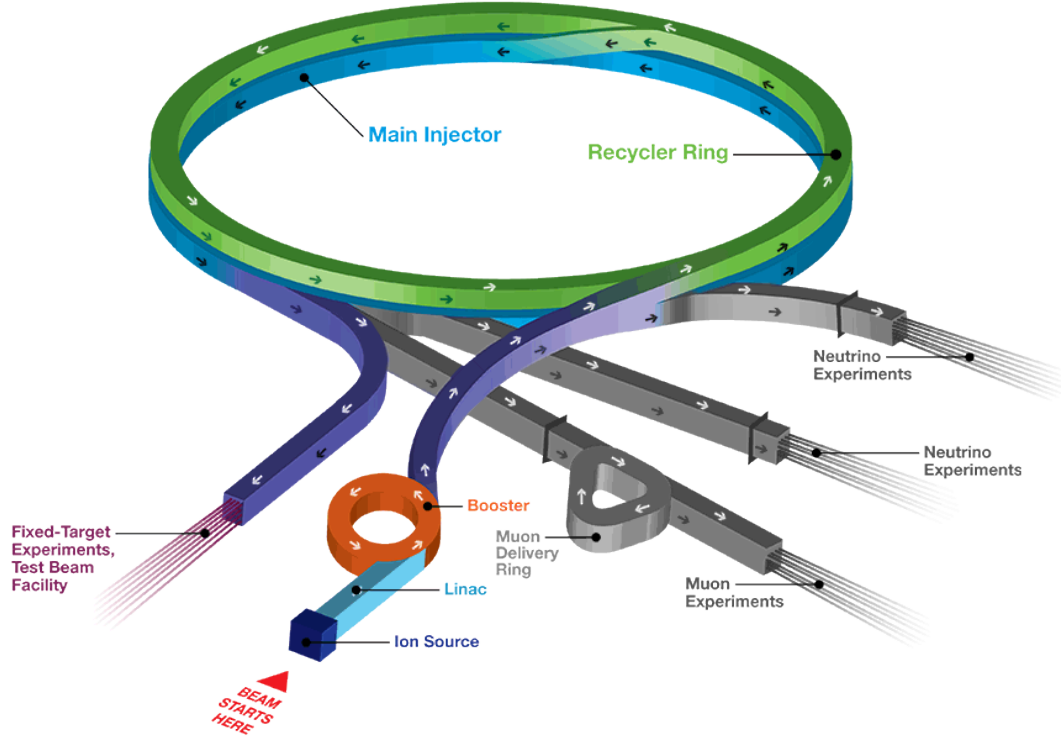


Figure 3.1: Layout of Fermilab Accelerator complex.

1339 particles polarity, to perform particle identification in the beamline and to measure
1340 the momentum of the tertiary beam particles before they get to the LArTPC. The
1341 LArIAT detectors are described in the following paragraphs.

1342 3.2 LArIAT Tertiary Beam Instrumentation

1343 The instrumentation of LArIAT tertiary beam and the TPC components have changed
1344 several times during the three years of LArIAT data taking. The following paragraphs
1345 describe the components operational during “Run II”, the data taking period relevant
1346 to the hadron cross section measurements considered in this thesis.

1347 The key components of the tertiary beamline instrumentation for the hadron cross
1348 section analyses are the two bending magnets, a set of four wire chambers (WCs)

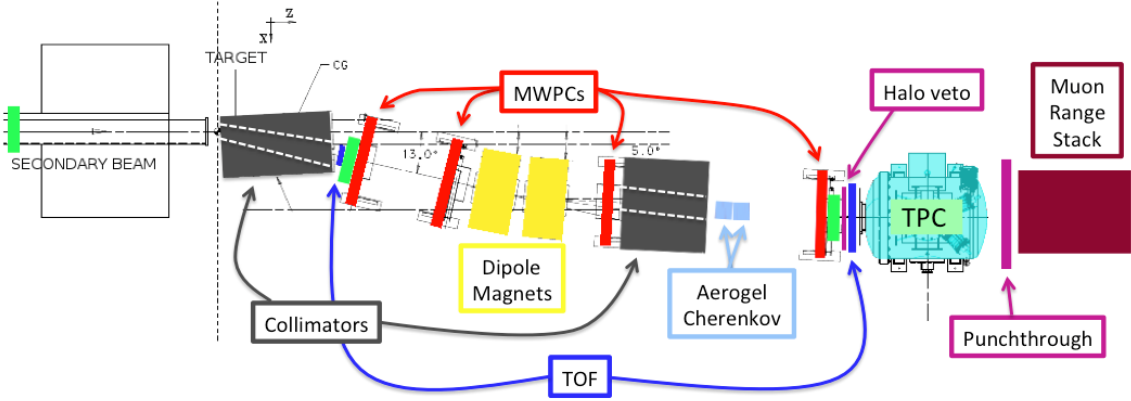


Figure 3.2: Bird’s eye view of the LArIAT tertiary beamline. In grey: upstream and downstream collimators; in yellow: bending magnets; in red: multi wire proportional chambers; in blue: time of flight; in green: liquid argon TPC volume; in maroon: muon range stack.

and two time-of-flight scintillating paddles (TOF) and, of course, the LArTPC. The magnets determine the polarity of the particles in the tertiary beam; the combination of magnets and wire chambers determines the particles’ momenta, which is used to determine the particle species in conjunction with the TOF. A muon range stack downstream from the TPC and two sets of cosmic paddles configured as a telescope surrounding the TPC are also used for calibration purposes. A couple of Aerogel Cherenkov counters, which we will not describe here as they are not used in the hadron cross section measurements, completes the beamline instrumentation.

3.2.1 Bending Magnets

LArIAT uses a pair of identical Fermilab type “NDB” electromagnets, recycled from the Tevatron’s anti-proton ring, in a similar configuration used for the MINERvA T-977 test beam calibration [56]. The magnets are a fundamental piece of the LArIAT beamline equipment, as they are used for the selection of the particle polarity and for the momentum measurement before the LArTPC. The sign of the current in the magnets allows us to select either positively or negatively charged particles; the value

1364 of the magnetic field is used in the momentum determination and in the subsequent
1365 particle identification.

1366 We describe here the characteristics and response of one magnet, as the second one
1367 has a similar response, given its identical shape and history. Each magnet is a box with
1368 a rectangular aperture gap in the center to allow for the particle passage. The magnet
1369 aperture measures 14.22 cm in height, 31.75 cm in width, and 46.67 cm in length.
1370 Since the wire chambers aperture ($\sim 12.8 \text{ cm}^2$) is smaller than the magnet aperture,
1371 only the central part of the magnet gap is utilized. The field is extremely uniform
1372 over this limited aperture and was measured with two hall probes, both calibrated
1373 with nuclear magnetic resonance probes. The probes measured the excitation curve
1374 shown in Figure 3.3.

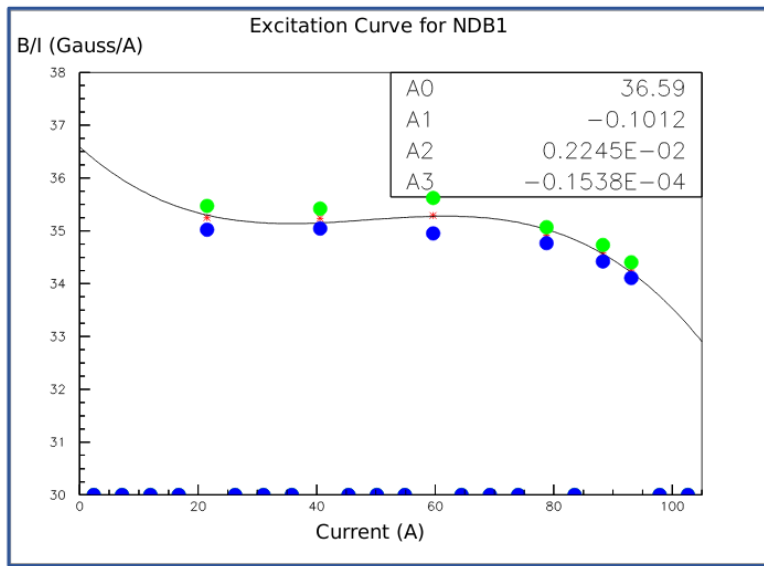


Figure 3.3: Magnetic field over current as a function of the current, for one NDB magnet (excitation curve). The data was collected using two hall probes (blue and green). We fit the readings with a cubic function (black) to average of measurements (red) given in the legend [43].

1375 The current through the magnets at a given time is identical in both magnets.
1376 For the Run II data taking period, the current settings explored were 60A ($B \sim 0.21$
1377 T) and 100A ($B \sim 0.35$ T) in both polarities. Albeit advantageous to enrich the
1378 tertiary beam composition with high mass particles such as kaons, we never pushed

1379 the magnets current over 100 A, not to incur in overheating. During operation, we
1380 operated an air and water cooling system on the magnets and we remotely monitored
1381 the magnet temperatures.

1382 **3.2.2 Multi-Wire Proportional Chambers**



Figure 3.4: One of the four Multi Wire Proportional Chambers (WC) used in the LArIAT tertiary beamline and related read-out electronics.

1383 LArIAT uses four multi-wire proportional chambers, or wire chambers (WC) for
1384 short, two upstream and two downstream from the bending magnets. The geometry of
1385 one chamber is shown in Figure 3.4: the WC effective aperture is a square of 12.8 cm
1386 perpendicular to the beam direction. Inside the chamber, the 128 horizontal and 128
1387 vertical wires strung at a distance of 1 mm from each other in a mixture of 85% Argon
1388 and 15% isobutane gas. The WC operating voltage is between 2400 V and 2500 V.
1389 The LArIAT wire chambers are an upgraded version of the Fenker Chambers [62],
1390 where an extra grounding improves the signal to noise ratio of the electronic readout.

1391 Two ASDQ chips [95] mounted on a mother board plugged into the chamber serve
1392 as front end amplifier/discriminator. The chips are connected to a multi-hit TDC [73]
1393 which provides a fast OR output used as first level trigger. The TDC time resolution
1394 is 1.18 ns/bin and can accept 2 edges per 9 ns. The maximum event rate acceptable
1395 by the chamber system is 1 MHz: this rate is not a limiting factor considering that

1396 the rate of the tertiary particle beam at the first wire chamber is estimated to be less
1397 than 15 kHz. A full spill of data occurring once per supercycle is stored on the TDC
1398 board memory at once and read out by a specially designed controller. We use LVDS
1399 cables to carry both power and data between the controller and the TDCs and from
1400 the controller to the rest of the DAQ.

1401 Multi-Wire Proportional Chambers functionality

1402 We use the wire chamber system together with the bending magnets to measure the
1403 particle's momentum.

1404 In the simplest scenario, only one hit on each and every of the four wire chambers
1405 is recorded during a single readout of the detector systems. Thus, we use the hit
1406 positions in the two wire chambers upstream of the magnets to form a trajectory
1407 before the bend, and the hit positions in the two wire chambers downstream of the
1408 magnets to form a trajectory after the bend. We use the angles in the XZ plane
1409 between the upstream and downstream trajectories to calculate the Z component of
1410 the momentum as follows:

$$P_z = \frac{B_{eff}L_{eff}}{3.3(\sin(\theta_{DS}) - \sin(\theta_{US}))}, \quad (3.1)$$

1411 where B_{eff} is the effective maximum field in a square field approximation, L_{eff}
1412 is the effective length of both magnets (twice the effective length of one magnet),
1413 θ_{US} is the angle off the z axis of the upstream trajectory, θ_{DS} is the angle off the
1414 z axis of the downstream trajectory and $3.3 c^{-1}$ is the conversion factor from [T·m]
1415 to [MeV/c]. By using the hit positions on the third and fourth wire chamber, we
1416 estimate the azimuthal and polar angles of the particle trajectory, and we are able to
1417 calculate the other components of the momentum.

1418 The presence of multiple hits in a single wire chamber or the absence of hits in one
1419 (or more) wire chambers can complicate this simple scenario. The first complication

is due to beam pile up, while the latter is due to wire chamber inefficiency. In the case of multiple hits on a single WC, at most one wire chamber track is reconstructed per event. Since the magnets bend particles only in the X direction, we assume the particle trajectory to be roughly constant in the YZ plane, thus we keep the combination of hits which fit best with a straight line. It is still possible to reconstruct the particle’s momentum even if the information is missing in either of the two middle wire chambers (WC2 or WC3), by constraining the particle trajectory to cross the plane in between the magnets.

Events satisfying the simplest scenario of one single hit in each of the four wire chambers form the “Picky Track” sample. We construct another, higher statistics sample, where we loosen the requirements on single hit and wire chamber efficiency: the “High Yield” sample. For LArIAT Run II, the High Yield sample is about three times the Picky Tracks statistics. We assume an uncertainty of 2% for four-point WC track, momentum uncertainty as reported for the same beamline in [56].

3.2.3 Time-of-Flight System

Two scintillator paddles, one upstream of the first set of WCs and one downstream of the second set of WCs form LArIAT time-of-flight (TOF) detector system.

The upstream paddle is made of a 10 x 6 x 1 cm scintillator piece, read out by two PMTs mounted on the beam left side which collect the light from light guides mounted on all four edges of the scintillator. The downstream paddle is a 14 x 14 x 1 cm scintillator piece read out by two PMTs on the opposite ends of the scintillator, as shown in figure 3.5. The relatively thin width in the beamline direction minimizes energy loss of beam particles traveling through the scintillator material.

The CAEN 1751 digitizer is used to digitize the TOF PMTs signals at a sampling rate of 1 GHz. The 12 bit samples are stored in a circular memory buffer. At trigger time, data from the TOF PMTs are recorded to output in a 28.7 μ s windows starting

1446 approximately 8.4 μ s before the trigger time.

1447 **TOF functionality**

1448 The TOF signals rise time (10-90%) is 4 ns and a full width, half-maximum of 9 ns
1449 consistent in time. The signal amplitudes from the upstream TOF and downstream
1450 TOF are slightly different: 200 mV for the upstream PMTs but only 50 mV for
1451 downstream PMTs. The time of the pulses was calculated utilizing an oversampled
1452 template derived from the data itself. We take the pulse pedestal from samples
1453 far from the pulse and subtract it from the pulse amplitude. We then vertically
1454 stretch a template to match the pedestal-subtracted pulse amplitude and we move
1455 it horizontally to find the time. With this technique, we find a pulse time-pickoff
1456 resolution better than 100 ps. The pulse pile up is not a significant problem given
1457 the TOF timing resolution and the rate of the particle beam. Leveraging on the
1458 pulses width uniformity of any given PMT, we flag events where two pulses overlap
1459 as closely in time as 4 ns with a 90% efficiency according to simulation.

1460 We combine the pulses from the two PMTs on each paddle to determine the
1461 particles' arrival time by averaging the time measured from the single PMT, so to
1462 minimize errors due to optical path differences in the scintillator. However, a time
1463 spread of approximately 300 ps is present in both the upstream and downstream
1464 detectors, likely due to transit time jitter in the PMTs themselves.

1465 **3.2.4 Punch-Through and Muon Range Stack Instruments**

1466 The punch-through and the muon range stack (MuRS) detectors are located down-
1467 stream of the TPC. These detectors provide a sample of TPC crossing tracks without
1468 relying on TPC information and can be used to improve particle ID for muons and
1469 pions with momentum higher than 450 MeV/c.

1470 The punch-through is simple sheet of scintillator material, read out by two PMTs.



Figure 3.5: Image of the down stream time of flight paddle, PMTs and relative support structure before mounting.

1471 The MuRS is a segmented block of steel with four slots instrumented with scintillation
1472 bars. The four steel layers in front of each instrumented slot are 2 cm, 2 cm, 14 cm
1473 and 16 cm deep in the beam direction. Each instrumented slot is equipped with
1474 four scintillation bars each, positioned horizontally in the direction orthogonal to the
1475 beam. Each scintillator bar measures $\textcolor{red}{? \times ? \times 2}$ cm and it is read out by one PMT.

1476 The signals from both the punch-thorough and the MuRS PMTs are sent to a
1477 NIM discriminator. If the signal crosses the discriminator threshold, it is digitized in
1478 the CAEN V1740, same as the TPC. The sampling time of the CAEN V1740 is slow
1479 (of the order of 128 ns) and that the pulse shape information from the PMT is lost.
1480 A Punch-thorough and MuRS signal will then be simply a “hit” at a given time in
1481 the beamline event.

1482 It is worth mentioning here the presence of an additional scintillation paddle
1483 between WC4 and the downstream paddle of the TOF system, called halo. The
1484 halo is a $39 \times 38 \times 1$ cm 3 paddle with a 6.5 cm radius hole in the center, whose original
1485 function was to reject beam particles slightly offset from the beamline center. Data

1486 from this paddle turned out to be unusable, so our data events include both particle
1487 going through the halo scintillation material or through the halo hole.

1488 3.2.5 LArIAT Cosmic Ray Paddle Detectors

1489 LArIAT triggers both on beam events and on cosmic rays events. We perform this
1490 latter trigger by using two sets of cosmic ray paddle detectors (a.k.a. “cosmic towers”.)
1491 The cosmic towers frame the LArIAT cryostat, as one sits in the downstream left
1492 corner and the other sits in the upstream right corner of the cryostat. Two paddle
1493 sets of four scintillators pieces each make up each cosmic tower, an upper set and a
1494 lower set per tower. Of the four paddles, a couple of two matched paddles stands
1495 upright while the a second matched pair lies across the top of the assembly in the top
1496 sets (or across the bottom of the assembly in the bottom sets). The horizontal couple
1497 is used as a veto for particles traveling from inside the TPC out. The four signals
1498 from the vertical paddles along one of the body diagonals of the TPC are combined
1499 in a logical “AND”. This allows to select track due to cosmic muons at the ground
1500 level crossing the TPC along one of its diagonals. Cosmic ray muons whose average
1501 energy is in the few GeV range crossing both anode and cathode populate the events
1502 triggered this way. This particularly useful sample of tracks is associated can be used
1503 for many tasks; for example, we use anode-cathode piercing tracks to cross check
1504 the TPC electric field on data (see Appendix A), to calibrate the charge response of
1505 the TPC wires for the full TPC volume and to measure the electron lifetime in the
1506 chamber [104].

1507 We retrieved the scintillation paddles from the decommissioning of the CDF de-
1508 tector at Fermilab and we used only the paddles with a counting efficiency greater
1509 than 95% and low noise at working voltage. The measured trigger rate of the whole
1510 system is 0.032 Hz, corresponding to ~ 2 muons per minute.



Figure 3.6: Photograph of one of the scintillation counters used in the cosmic towers.

1511 3.3 In the Cryostat

1512 The heart of the LArIAT experiment lives in the LArIAT cryostat. In this section,
1513 we describe the cryogenic system and the argon purity (Section 3.3.1), the LArIAT
1514 TPC (Section 3.3.2) and light collection system (3.3.3).

1515 3.3.1 Cryogenics and Argon Purity

1516 LArIAT repurposed the ArgoNeuT cryostat [17] in order to use it in a beam of charged
1517 particles, and added a new process piping and a new liquid argon filtration system in
1518 FTBF. Inside the LArIAT experimental hall, the cryostat sits in the beam of charged
1519 particles with its horizontal main axis oriented parallel to the secondary beam, 3°
1520 off axis from the tertiary beam

1521 Two volumes make up LArIAT cryostat, shown in Figure 3.7: the inner vessel and
1522 the outer vessel. Purified liquid argon fills the inner vessel, while the outer volume
1523 provides insulation through a vacuum jacket equipped with layers of aluminized mylar
1524 superinsulation. The inner vessel is a cylinder of 130 cm length and 76.2 cm diameter,
1525 containing about 550 L of LAr, corresponding to a mass of 0.77 ton. We run the signal
1526 cables for the LArTPC and the high voltage feedthrough through a “chimney” at the
1527 top and mid-length of the cryostat.

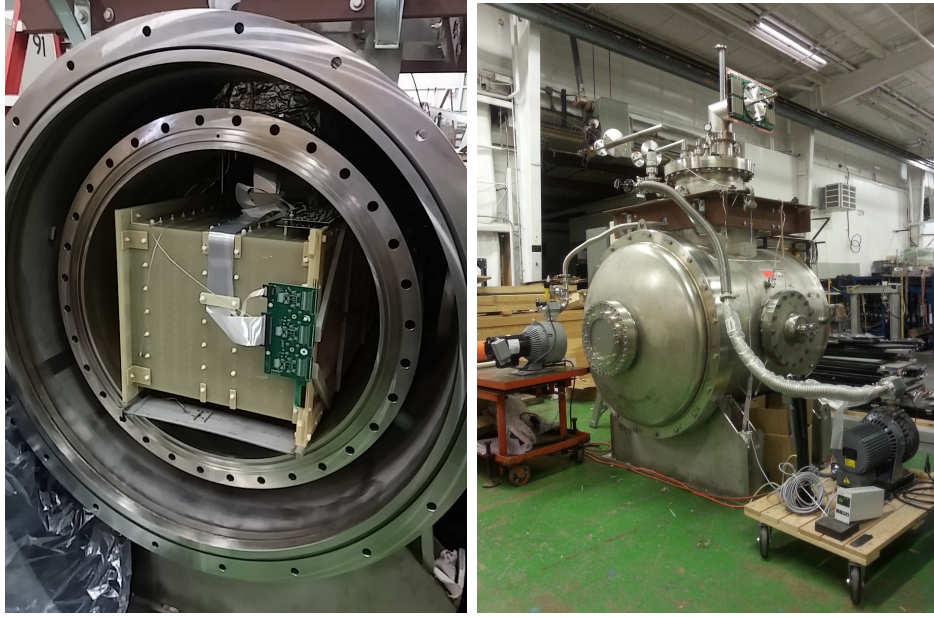


Figure 3.7: Left: the LArIAT TPC in the inner volume of the open cryostat. Right: cryostat fully sealed ready to be transported to FTBF.

Given the different scopes of the ArgoNeuT and LArIAT detectors, we made several modifications to the ArgoNeuT cryostat in order to use it in LArIAT. In particular, the modifications shown in Figure 3.8 were necessary to account for the beam of charged particles entering the TPC and to employ the new FTBF liquid argon purification system. We added a “beam window” on the front outer end cap and an “excluder” on the inner endcap, with the purpose of minimizing the amount of non-instrumented material upstream of the TPC’s active volume. The amount of non-instrumented material in front of the TPC for LArIAT corresponds to ~ 0.3 electron radiation lengths (X_0), to compare against the $\sim 1.6X_0$ of ArgoNeuT. To allow studies of the scintillation light, we added a side port feedthrough which enables the mounting of the light collection system, as well as the connections for the corresponding signal and high-voltage cables (see Section 3.3.3). We modified the bottom of the cryostat adding Conflat and ISO flange sealing to connect the liquid argon transfer line to the new argon cooling and purification system.

As in any other LArTPC, argon purity is a crucial parameter for LArIAT. Indeed,



Figure 3.8: Main modifications to the ArgoNeuT cryostat: 1) outlet for connection to the purification system at the bottom of the cryostat; 2) the “beam-window” on the outer endcap and “excluder” which reduces the amount of non-instrumented material before the TPC; 3) the side port to host the light collection system.

1543 the presence of contaminants affects both the basic working principles of a LArTPC,
 1544 as shown in section 2.1.2: electronegative contaminants such as oxygen and water de-
 1545 crease the number of ionization electrons collected on the wires after drifting through
 1546 the volume. In addition, contaminants such as Nitrogen decrease the light yield
 1547 from scintillation light, especially in its slow component. In LArIAT, contaminations
 1548 should not exceed the level of 0.2 parts per billion (ppb). We achieve this level of
 1549 purity in several stages. The specifics required for the commercial argon bought for
 1550 LArIAT are 2 parts per million (ppm) oxygen, 3.5 ppm water, and 10 ppm nitrogen.
 1551 This argon is monitored with the use of commercial gas analyzer. Argon is stored in
 1552 a dewar external to LArIAT hall and filtered before filling the TPC. LArIAT uses a
 1553 filtration system designed for the Liquid Argon Purity Demonstrator (LAPD) [57]:
 1554 half of a 77 liter filter contains a 4A molecular sieve (Sigma-Aldrich [110]) able to re-
 1555 move mainly water, while the other half contains BASF CU-0226 S, a highly dispersed
 1556 copper oxide impregnated on a high surface area alumina, apt to remove mainly oxy-

1557 gen [27]. A single pass of argon in the filter is sufficient to achieve the necessary
1558 purity, unless the filter is saturated. In case the filter saturates, the media needs to
1559 be regenerated by using heated gas; this happened twice during the Run II period¹.
1560 The electron lifetime during the full LArIAT data taking are shown in Figure 2.4.
1561 The filtered argon reaches the inner vessel via a liquid feedthrough which is routed to
1562 the bottom of the cryostat. Argon is not recirculated in the system; rather, it boils
1563 off and vents to the atmosphere. During data taking, we replenish the argon in the
1564 cryostat every 6 hours to keep the TPC high voltage feedthrough and cold electronics
1565 always submerged. In fact, we constantly monitor the level, temperature, and pres-
1566 sure of the argon both in the commercial dewar and inside the cryostat during data
1567 taking.

1568 **3.3.2 LArTPC: Charge Collection**

1569 The LArIAT Liquid Argon Time Projection Chamber is a rectangular box of dimen-
1570 sions 47 cm (drift) x 40 cm (height) x 90 cm (length), containing 170 liters of Liquid
1571 Argon. The LArTPC three major subcomponents are

- 1572 1) the cathode and field cage,
- 1573 2) the wire planes,
- 1574 3) the read-out electronics.

1575 **Cathode and field cage**

1576 A G10 plain sheet with copper metallization on one of the 40 x 90 cm inner surfaces
1577 forms the cathode. A high-voltage feedthrough on the top of the LArIAT cryostat
1578 delivers the high voltage to the cathode; the purpose of the high voltage system

1. We deemed the filter regeneration necessary every time the electron lifetime dropped under 100 μ s.

1579 (Figure 3.9) is to drift ionization electrons from the interaction of charged particles
 1580 in the liquid argon to the wire planes. The power supply used in this system is a
 1581 Glassman LX125N16 [70] capable of generating up to -125 kV and 16 mA of current,
 1582 but operated at -23.5kV during LArIAT Run-II. The power supply is connected via
 1583 high voltage cables to a series of filter pots before finally reaching the cathode.

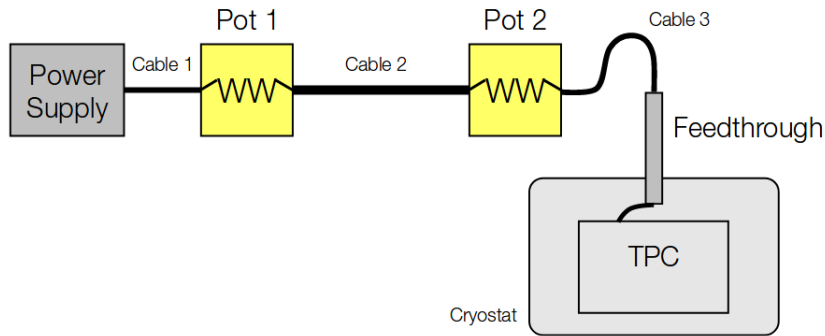


Figure 3.9: Schematic of the LArIAT high voltage system.

1584 The field cage is made of twenty-three parallel copper rings framing the inner walls
 1585 of the G10 TPC structure. A network of voltage-dividing resistors connected to the
 1586 field cage rings steps down the high voltage from the cathode to form a uniform electric
 1587 field. The electric field over the entire TPC drift volume is 486 V/cm, as measured
 1588 in appendix A. The maximum drift length, i.e. the distance between cathode and
 1589 anode planes, is 47 cm.

1590 Wire planes

1591 LArIAT Run-II has three wire planes separated by 4 mm spaces: in order of increasing
 1592 distance from the cathode, they are the shield, the induction and the collection plane.
 1593 The “wire pitch”, i.e., the distance between two adjacent wires in a given plane, is
 1594 4 mm. The shield plane counts 225 parallel wires of equal length oriented vertically.
 1595 This plane is not connected with the read-out electronics; rather it shields the outer
 1596 planes from extremely long induction signals due to the ionization in the whole drift

volume. As the shield plane acts almost like a Faraday cage, the resulting shape of signals in the first instrumented plane (induction) is easier to reconstruct. Both the induction and collection planes count 240 parallel wires of different length oriented at 60° from the vertical with opposite signs. Electrons moving past the induction plane will induce a bipolar pulse on its wires; the drifting electrons will be then collected on the collection plane's wires, forming a unipolar pulse.

The three wire planes and the cathode form three drift volumes, as shown in Figure 3.10. The main drift volume is defined as the region between the cathode plane and the shield plane (C-S). The other two drift regions are those between the shield plane and the induction plane (S-I), and between the induction plane and the collection plane (I-C). The electric field in these regions is chosen to satisfy the charge transparency condition and allow for 100% transmission of the drifting electrons through the shield and the induction planes.

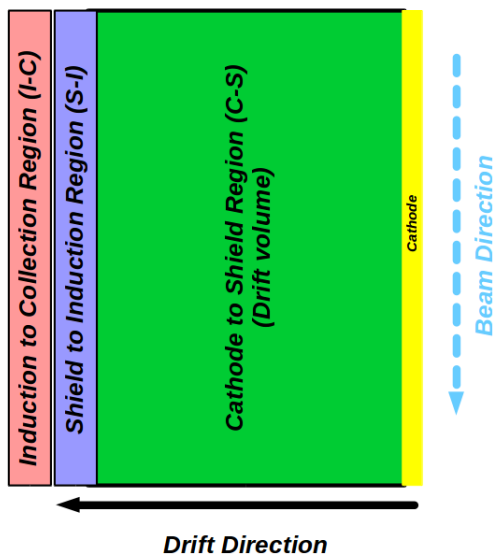


Figure 3.10: Schematic of the three drift regions inside the LArIAT TPC: the main drift volume between the cathode and the shield plane (C-S) in green, the region between the shield plane and the induction plane (S-I) in purple, and the region between the induction plane and the collection plane (I-C) in pink.

Table 3.1 provides the default voltages applied to the cathode and the shield,

1611 induction, and collection plane.

Table 3.1: Cathode and anode planes default voltages

Cathode	Shield	Induction	Collection
-23.17 kV	-298.8 V	-18.5 V	338.5 V

1612 Electronics

1613 Dedicated electronics read the induction and collection plane wires, for a total of
1614 480-channel analog signal path from the TPC wires to the signal digitizers. A digital
1615 control system for the TPC-mounted electronics, a power supply, and a distribution
1616 system complete the front-end system. Figure 3.11 shows a block diagram of the
1617 overall system. The direct readout of the ionization electrons in liquid argon forms
1618 typically small signals on the wires, which need amplification in oder to be processed.
1619 LArIAT performs the amplification stage directly in cold with amplifiers mounted
1620 on the TPC frame inside the liquid argon. The BNL ASICs adopted in LArIAT are
1621 designated as LArASIC, version 4-star and are the same used by the MicroBooNE
1622 experiment [60]. The signal from the ASICs are driven to the other end of the readout
1623 chain, to the CAEN V1740 digitizers [35]. The CAEN V1740 has a 12 bit resolution
1624 and a maximum input range of 2 VDC, resulting in about 180 ADC count for a
1625 crossing MIP.

1626 3.3.3 LArTPC: Light Collection System

1627 The collection of scintillation photons is the second mechanism of particle detection
1628 in argon other than the ionization electrons. Over the course of LArIAT's three years
1629 of data taking, the light collection system changed several times. We describe here
1630 the light collection system for Run II. Two PMTs, a 3-inch diameter Hamamatsu
1631 R-11065 and 2-inch diameter ETL D757KFL [7], as well as three SiPMs arrays (two
1632 Hamamatsu S11828-3344M 4x4 arrays and one single-channel SensL MicroFB-60035)

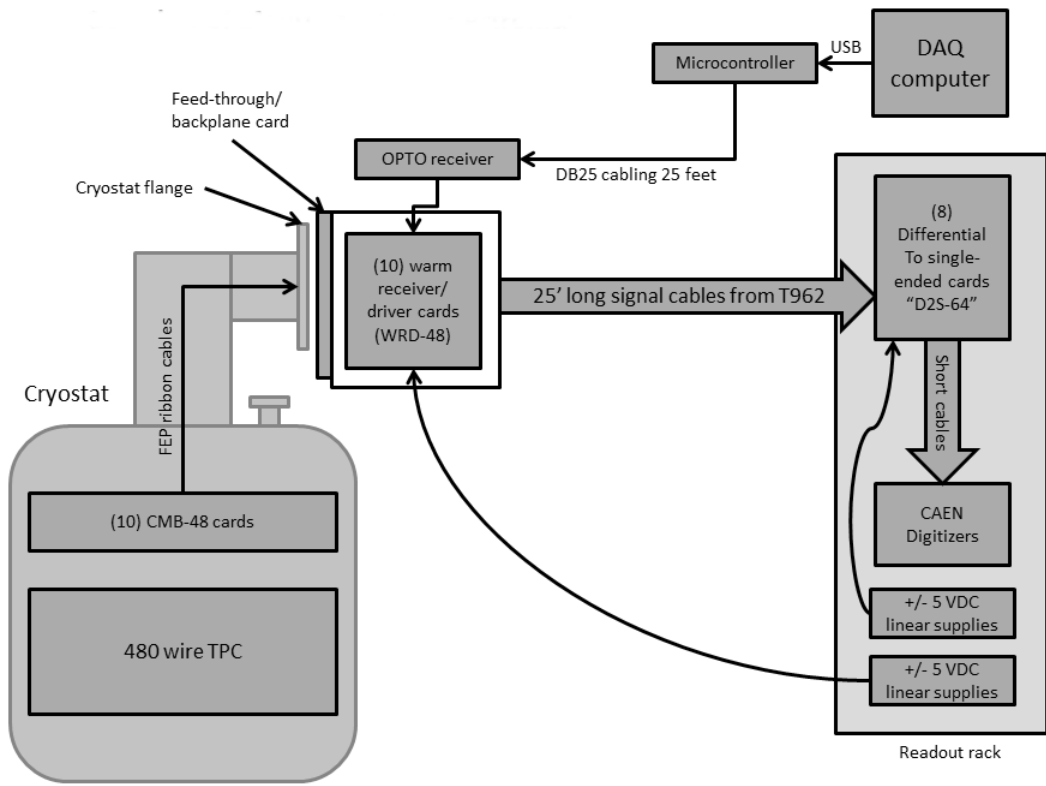


Figure 3.11: Overview of LArIAT Front End electronics.

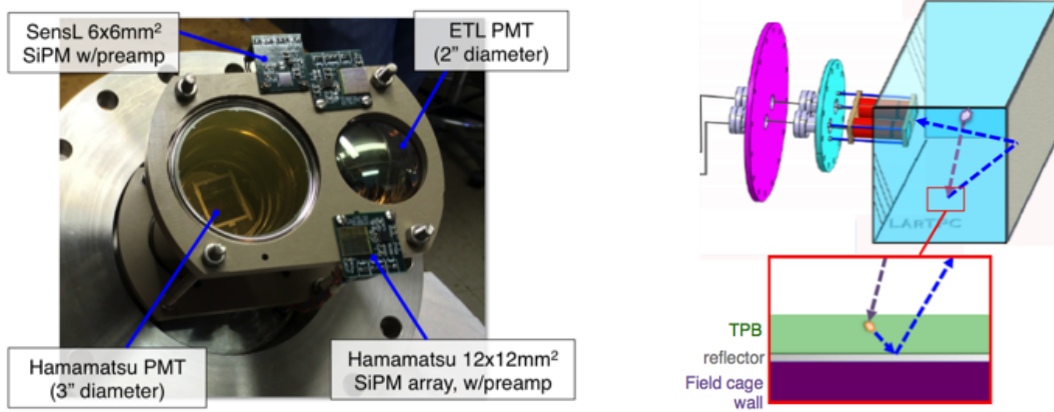


Figure 3.12: LArIAT’s photodetector system for observing LAr scintillation light inside the TPC (left), and a simplified schematic of VUV light being wavelength-shifting along the TPB-coated reflecting foils (right).

1633 are mounted on the PEEK support structure. PEEK screws into an access flange
 1634 as shown in Figure 3.12, on the anode side, leaving approximately 5 cm of clearance
 1635 from the collection plane.

1636 Liquid argon scintillates in vacuum-ultraviolet (VUV) range at 128 nm; since
 1637 cryogenic PMTs are not sensitive to VUV wavelengths, we need to shift the light to a
 1638 range that is visible to the PMTs. In LArIAT, the wavelength shifting is achieved by
 1639 installing highly-reflective 3M VIKUITI dielectric substrate foils coated with a thin
 1640 layer of tetraphenyl-butadiene (TPB) on the four unbiased walls of the TPC. The
 1641 scintillation light interaction with the TPB emits one or more visible photons, which
 1642 are then reflected into the chamber. Thus, the light yield increases and results in
 1643 higher uniformity of light across the TPC active volume, allowing the possibility of
 1644 light-based calorimetry, currently under study.

1645 For Run II, we coated the windows of the ETL PMT and the SensL SiPM with
 1646 a thin layer of TPB. In doing so, some of the VUV scintillation light converts into
 1647 visible right at the sensor faces, keeping information on the direction of the light
 1648 source. Information about the light directionality is hindered for the light reflected
 1649 on foils, as the reflection is uniform in angle.

1650 3.4 Trigger and DAQ

1651 The LArIAT DAQ and trigger system governs the read out of all the many subsystems
1652 forming LArIAT. The CAEN V1495 module [34] and its user-programmable FPGA
1653 are the core of this system. Every 10 ns, this module checks for matches between
1654 sixteen logical inputs and user-defined patterns in the trigger menu; if it finds a match
1655 for two consecutive clock ticks, that trigger fires.

1656 LArIAT receives three logic signals from the Fermilab accelerator complex related
1657 to the beam timing which we use as input triggers: a pulse just before the beam, a
1658 pulse indicating beam-on, and a beam-off pulse.

1659 The beam instruments, the cosmic ray taggers, and the light collection system
1660 provide the other NIM-standard logic pulse inputs to the trigger decision. We auto-
1661 matically log the trigger inputs configuration with the rest of the DAQ configuration
1662 at the beginning of each run.

1663 Fundamental inputs to the trigger card come from the TOF (see section 3.2.3)
1664 and the wire chambers (see section 3.2.2), as activity in these systems points to the
1665 presence of a charged particle in tertiary beam line. In particular, the discriminated
1666 pulses from the TOF PMTs form a NIM logic pulse for the trigger logic. We ask
1667 for a coincidence within a 20 ns window for all the pulses from the PMTs looking at
1668 the same scintillator block and use a delayed coincidence between the upstream and
1669 downstream paddle to inform the trigger decision. In order to form a coincidence
1670 between the upstream and downstream paddles, we delay the upstream paddle coin-
1671 cidence by 20 ns and widen it by 100 ns. The delay and widening are necessary to
1672 account for both lightspeed particles and slower particles (high-mass) to travel the
1673 6.5 m between the upstream and the downstream paddles. For the read out of the
1674 wire chambers, we use a total of sixteen multi-hit TDCs [73], four per chamber: two
1675 TDC per plane (horizontal and vertical), sixty-four wires per TDC. In each TDC, we
1676 keep the logical “OR” for any signal over threshold from the sixty-four wires. We

1677 then require a coincidence between the “OR” for the horizontal TDCs and the “OR”
1678 for the vertical TDCs: with this logic we make sure that at least one horizontal wire
1679 and one vertical wire saw significant signal in one wire chamber. The single logical
1680 pulse from each of the four wire chambers feeds into the first four inputs to the V1495
1681 trigger card. We require a coincidence within 20 ns of at least three logical inputs to
1682 form a trigger.

1683 The cosmic towers (see Section 3.2.5) provide another primary input to the trigger,
1684 in order to capture long tracks from cosmic muons crossing the TPC. We use NIM
1685 modules to require coincidences between one upper and one lower paddle set of any
1686 opposite cosmic towers. The OR all the opposite towers’ coincidences is fed as an
1687 input to the trigger card.

1688 We use the signal from the cryogenic PMTs (see Section 3.3.3) to form several
1689 interesting triggers. The coincidence of signals from all the PMT pulses within \sim 20 ns
1690 is an indication of ionizing radiation in the TPC and forms a trigger input. The
1691 coincidence of two subsequent scintillation logic pulses delayed by a maximum of $7 \mu\text{s}$
1692 forms the Michel electron trigger.

1693 3.5 Control Systems

1694 LArIAT is a complex ensemble of systems which needed to be monitored simultane-
1695 ously during data taking. We performed the monitoring of the systems operations
1696 with a slow control system, a DAQ monitoring system and a low level data quality
1697 monitoring described in the following sections.

1698 Slow Control

1699 We used the Synoptic Java Web Start framework [19] as a real-time display of subsys-
1700 tem conditions. Synoptic provides a Graphical User Interface that talks to the Fer-

milab Accelerator Control System via the ACNET protocol. Its simple GUI allowed us to change the operating parameters and to graph the trends of several variables of interest for all of the tertiary beam detectors. Among the most important quantities monitored by Synoptic there are the level of argon in both the inner vessel and the external dewar, the operating voltages of cathode and wire planes, of the PMTs and SiPMs, and of the four wire chambers, as well as the magnet temperatures. Figure 3.13 shows an example of the monitoring system. LArIAT uses the Accelerator Control NETwork system (ACNET) to monitor the beam conditions of the MCcenter beamline. For example, the horizontal and vertical position of the beam at the first two wire chambers (WC1 and WC2) are shown in 3.14 as seen by the shifter during data taking.

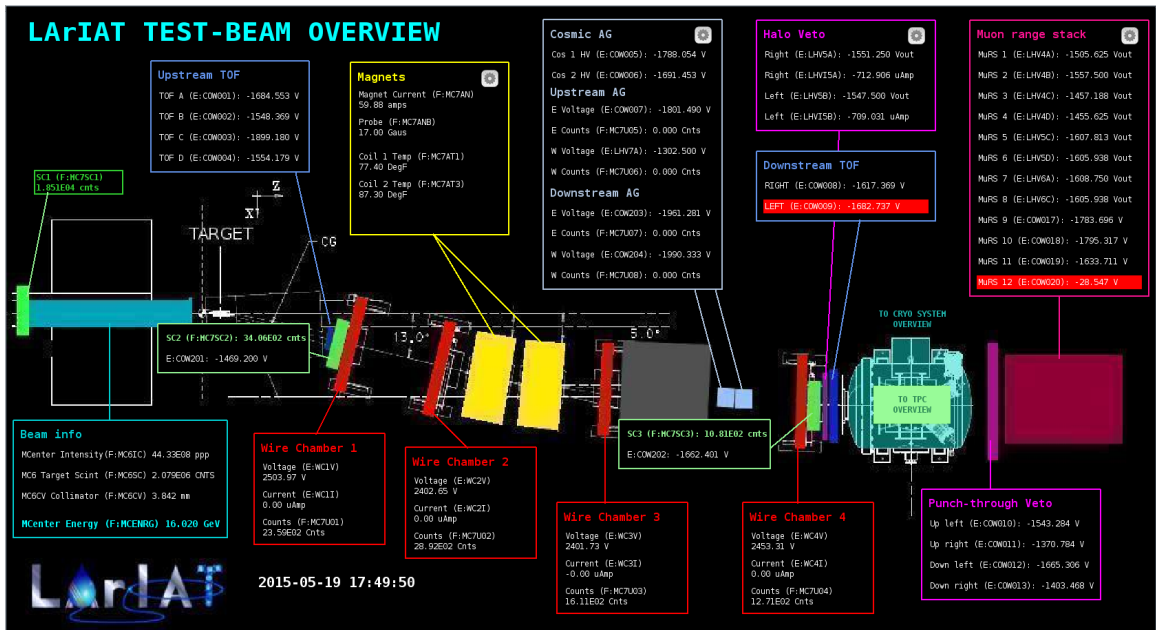


Figure 3.13: Interface of the Synoptic slow control system

1712 DAQ Monitoring

1713 We monitor the data taking and the run time evolution with the Run Status Webpage
 1714 (<http://lariat-wbm.fnal.gov/lariat/run.html>), a webpage updated in real-time. The

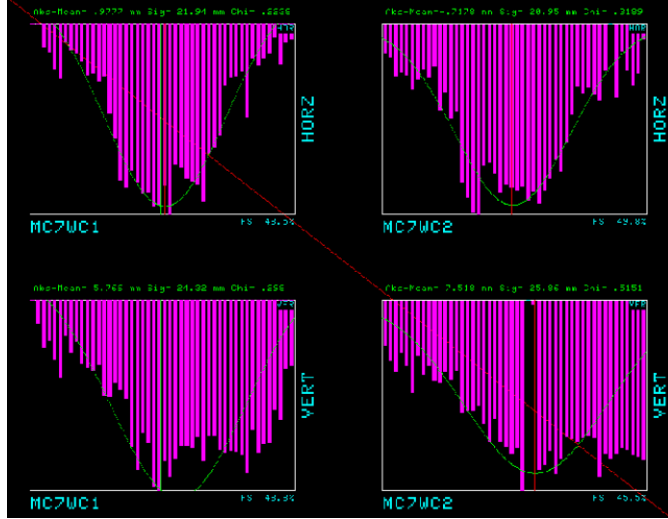


Figure 3.14: Beam position at the upstream wire chambers monitored with ACNET.

1715 page displays, among other information, the total number of triggers in the event,
 1716 the total number of detectors triggered during a beam spill, the trigger patterns, the
 1717 number of times a particular trigger pattern was satisfied during a beam spill, and
 1718 the current time relative to the Fermilab accelerator complex supercycle. A screen
 1719 shot of the page is show in figure 3.15.

1720 Data Quality Monitoring

1721 We employ two systems to ensure the quality of our data during data taking: the
 1722 Near-Real-Time Data Quality Monitoring and the Event Viewer.

1723 The Near-Real-Time Data Quality Monitoring (DQM) is a webpage which receives
 1724 updates from all the VME boards in the trigger system and displays the results of
 1725 a quick analysis of the DAQ stream of raw data on a spill-by-spill basis. The DQM
 1726 allows the shifter to monitor almost in real time (typically with a 2-minute delay)
 1727 a series of low level-quantities and compare them to past collections of beam spills.
 1728 Some of the variables monitored in the DQM are the pedestal mean and RMS on
 1729 CAEN digitizer boards of the TPC wires and PMTs of the beamline detectors, the
 1730 hit occupancy and timing plots on the wire chambers, and number of data fragments

1731 recorded that are used to build a TPC event. Abnormal values for low-level quantity
1732 in the data activates a series of alarms in the DQM; this quick feedback on the DAQ
1733 and beam conditions is fundamental to assure a fast debugging of the detector and a
1734 very efficient data taking during beam uptime.

1735 The online Event Viewer displays a two dimensional representation (Wire vs Time)
1736 of LArIAT TPC events on both the Induction and the Collection planes in near real
1737 time. The raw pulses collected by the DAQ on each wire are plotted as a function
1738 of drift time, resulting in an image of the TPC event easily readable by the shifter.
1739 This tool guarantees a particularly good check of the TPC operation which activate
1740 an immediate feedback for troubleshooting a number of issues. For example, it is
1741 easy for the shifter to spot high occupancy events and request a reduction of the
1742 primary beam intensity, or to spot a decrease of the argon purity which requires the
1743 regeneration of filters, or to catch the presence of electronic noise and reboot the
1744 ASICs. An example of high occupancy event is shown in 3.16.

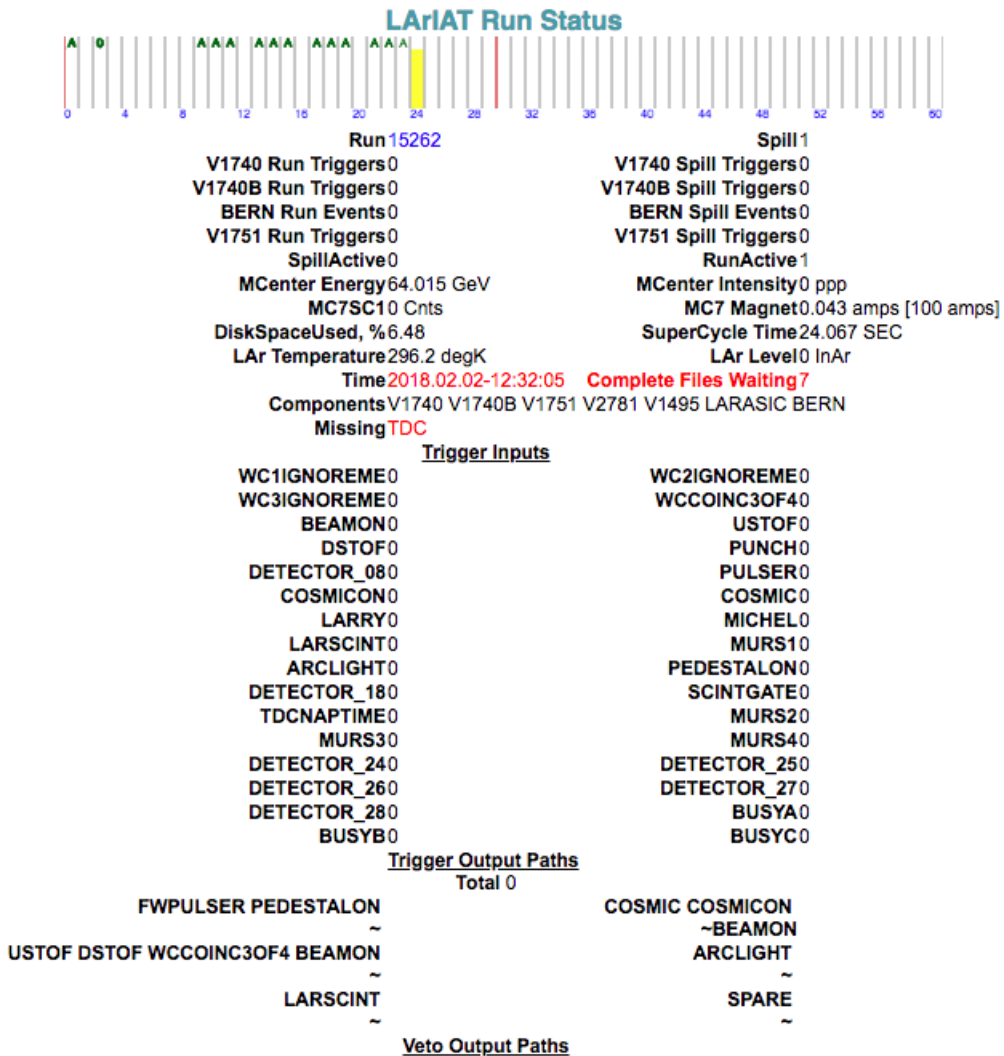


Figure 3.15: Run Status page at LArIAT downtime. At the top the yellow bar displays the current position in the Fermilab supercycle. Interesting information to be monitored by the shifter were the run number and number of spills, time elapsed from data taking (here in red), the energy of the secondary beam and the trigger paths.

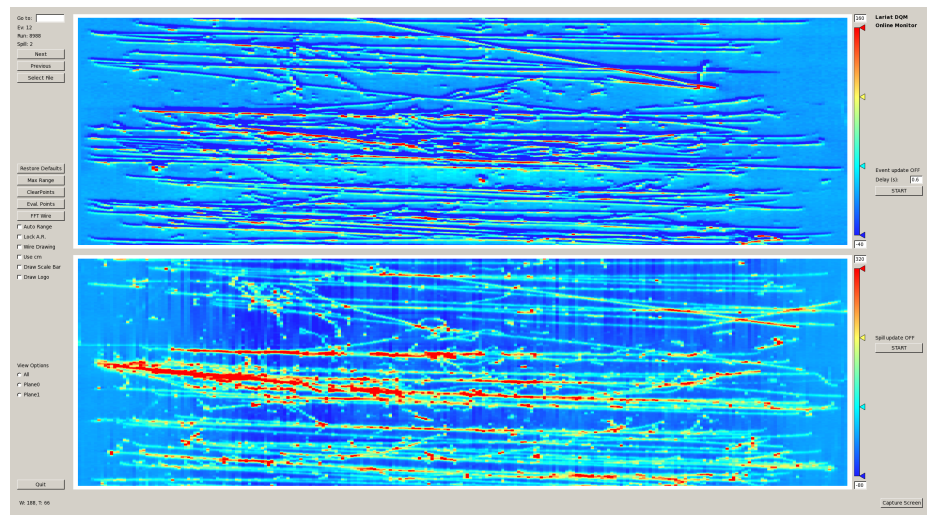


Figure 3.16: High occupancy event display: induction plane (top) and collection plane (bottom).

¹⁷⁴⁵ **Chapter 4**

¹⁷⁴⁶ **Total Hadronic Cross Section**

¹⁷⁴⁷ **Measurement Methodology**

¹⁷⁴⁸ “Like a lemon to the lime and the bubble to the bee”

¹⁷⁴⁹ – Eazy-E, 1993 –

¹⁷⁵⁰ This chapter describes the general procedure employed to measure a total hadronic
¹⁷⁵¹ differential cross section in LArIAT. Albeit with small differences, both the (π^- ,Ar)
¹⁷⁵² and (K^+ ,Ar) total hadronic cross section measurements rely on the same procedure.
¹⁷⁵³ We start by selecting the particle of interest using a combination of beamline detectors
¹⁷⁵⁴ and TPC information (Section 4.1). We then perform a handshake between the
¹⁷⁵⁵ beamline information and the TPC tracking to assure the selection of the correct
¹⁷⁵⁶ TPC track (Section 4.2). Finally, we apply the “thin slice” method and measure the
¹⁷⁵⁷ “raw” hadronic cross section (Section 4.3). A series of corrections are then evaluated
¹⁷⁵⁸ to obtain the “true” cross section (Section 4.3.3).

¹⁷⁵⁹ At the end of this chapter, we show a sanity check of the methodology by applying
¹⁷⁶⁰ the thin slice method employing only MC truth information and retrieving the Geant4
¹⁷⁶¹ tabulated cross section for pions and kaons (Section 4.4).

1762 4.1 Event Selection

1763 The measurement of the (π^- ,Ar) and (K^+ ,Ar) total hadronic cross section in LArIAT
1764 starts by selecting the pool of pion or kaon candidates and measuring their momen-
1765 tum. This is done through the series of selections on beamline and TPC information
1766 described in the next sections. The summary of the event selection in data is reported
1767 in Table 4.1.

1768 4.1.1 Selection of Beamline Events

1769 As shown in equation 4.5, we leverage the beamline particle identification and mo-
1770 mentum measurement before entering the TPC as an input to evaluate the kinetic
1771 energy for the hadrons used in the cross sections measurements. Thus, we select the
1772 LArIAT data to keep only events whose wire chamber and time of flight information
1773 is registered (line 1 in Table 4.1). Additionally, we perform a check of the plausi-
1774 bility of the trajectory inside the beamline detectors: given the position of the hits
1775 in the four wire chambers, we make sure the particle's trajectory does not cross any
1776 impenetrable material such as the collimator and the magnets steel (line 2 in Table
1777 4.1).

	Run-II Neg Pol	Run-II Pos Pol
1. Events Reconstructed in Beamline	158396	260810
2. Events with Plausible Trajectory	147468	240954
3. Beamline $\pi^-/\mu^-/e^-$ Candidate	138481	N.A.
4. Beamline K^+ Candidate	N.A	2837
5. Events Surviving Pile Up Filter	108929	2389
6. Events with WC2TPC Match	41757	1081
7. Events Surviving Shower Filter	40841	N.A.
8. Available Events For Cross Section	40841	1081

Table 4.1: Number of data events for Run-II Negative and Positive polarity

1778 **4.1.2 Particle Identification in the Beamline**

1779 In data, the main tool to establish the identity of the hadron of interest is the LArIAT
1780 tertiary beamline, in its function of mass spectrometer. We combine the measurement
1781 of the time of flight, TOF , and the beamline momentum, p_{Beam} , to reconstruct the
1782 invariant mass of the particles in the beamline, m_{Beam} , as follows

$$m_{Beam} = \frac{p_{Beam}}{c} \sqrt{\left(\frac{TOF * c}{l}\right)^2 - 1}, \quad (4.1)$$

1783 where c is the speed of light and l is the length of the particle's trajectory between
1784 the time of flight paddles.

1785 Figure 4.1 shows the mass distribution for the Run II negative polarity runs on
1786 the left and positive polarity runs on the right. We perform the classification of events
1787 into the different samples as follows:

- 1788 • $\pi/\mu/e$: mass $< 350 \text{ MeV}/c^2$
1789 • kaon: $350 \text{ MeV} < \text{mass} < 650 \text{ MeV}/c^2$
1790 • proton: $650 \text{ MeV} < \text{mass} < 3000 \text{ MeV}/c^2$.

1791 Lines 3 and 4 in Table 4.1 show the number of negative $\pi/\mu/e$ and positive K
1792 candidates which pass the mass selection for LArIAT Run-II data.

1793 **4.1.3 TPC Selection: Halo Mitigation**

1794 The secondary beam impinging on LArIAT secondary target produces a plethora of
1795 particles which propagates downstream. The presence of upstream and downstream
1796 collimators greatly abates the number of particles tracing down the LArIAT tertiary
1797 beamline. However, it is possible that more than one particle sneaks into the LArTPC
1798 during its readout time: the TPC readout is triggered by the particle firing the

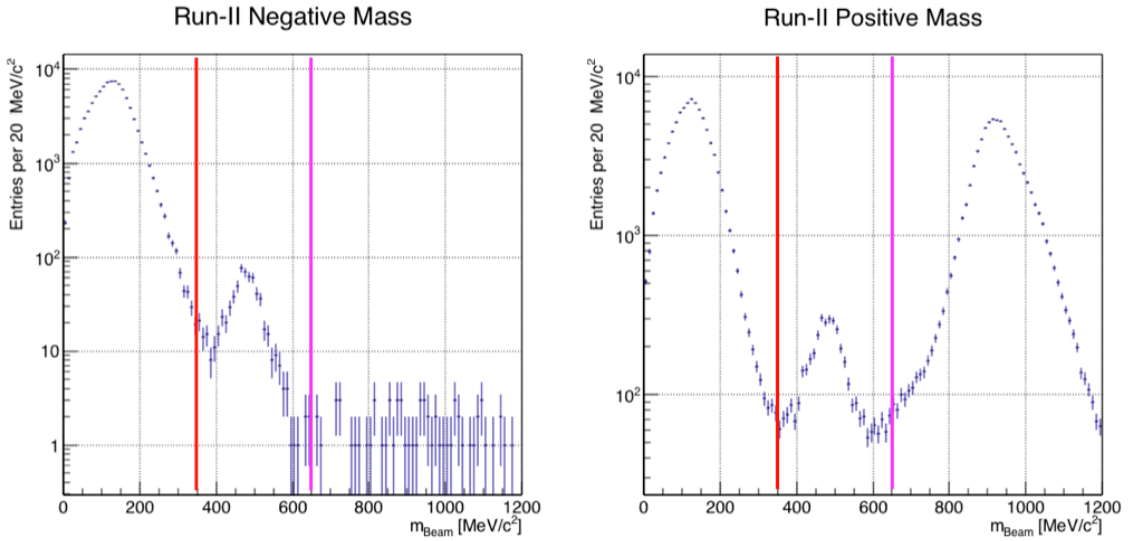


Figure 4.1: Distribution of the beamline mass as calculated according to equation 4.1 for the Run-II events reconstructed in the beamline, negative polarity runs on the left and positive polarity runs on the right. The classification of the events into $\pi^\pm/\mu^\pm/e^\pm$, K^\pm , or (anti)proton is based on these distributions, whose selection cut are represented by the vertical colored lines.

1799 beamline detectors, but particles from the beam halo might be present in the TPC at
 1800 the same time. We call “pile up” the additional traces in the TPC. We adjusted the
 1801 primary beam intensity between LArIAT Run I and Run II to reduce the presence of
 1802 events with high pile up particles in the data sample. For the cross section analyses,
 1803 we remove events with more than 4 tracks in the first 14 cm upstream portion of the
 1804 TPC from the sample (line 5 in in Table 4.1).

1805 4.1.4 TPC Selection: Shower Removal

1806 In the case of the (π^-,Ar) cross section, the resolution of beamline mass spectrometer
 1807 is not sufficient to select a beam of pure pions. In fact, muons and electrons survive
 1808 the selection on the beamline mass. It is important to notice that the composition of
 1809 the negative polarity beam is mostly pions, as will be discussed in section 5.2.1. Still,
 1810 we devise a selection on the TPC information to mitigate the presence of electrons

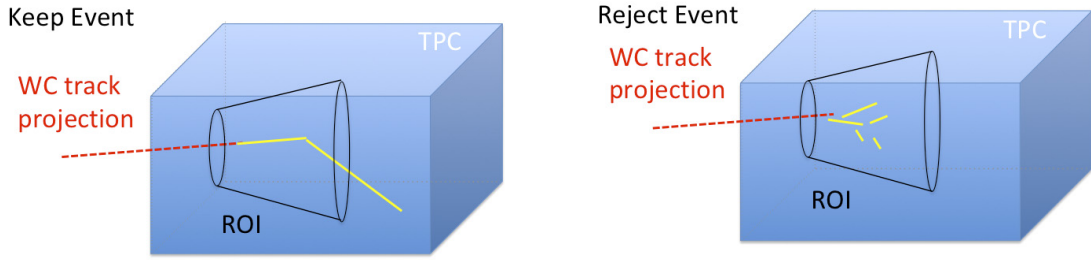


Figure 4.2: Visual rendering of the shower filter. The ROI is a cut cone, with a small radius of 4 cm, a big radius of 10 cm and an height of 42 cm (corresponding to 3 radiation lengths for electrons in Argon).

1811 in the sample used for the pion cross section. The selection relies on the different
 1812 topologies of a pion and an electron event in the argon: while the former will trace
 1813 a track inside the TPC active volume, the latter will tend to “shower”, i.e. interact
 1814 with the medium, producing bremsstrahlung photons which pair convert into several
 1815 short tracks. In order to remove the shower topology, we create a region of interest
 1816 (ROI) around the TPC track corresponding to the beamline particle. We look for
 1817 short tracks contained in the ROI, as depicted in figure 4.4: if more than 5 tracks
 1818 shorter than 10 cm are in the ROI, we reject the event. Line 7 in Table 4.1 shows
 1819 the number of events surviving this selection.

1820 4.2 Beamline and TPC Handshake: the Wire Cham- 1821 ber to TPC Match

1822 For each event passing the selection on its beamline information, we need to identify
 1823 the track inside the TPC corresponding to the particle which triggered the beamline
 1824 detectors, a procedure we refer to as “WC to TPC match” (WC2TPC for short).
 1825 In general, the TPC tracking algorithm will reconstruct more than one track in the
 1826 event, partially due to the fact that hadrons interact in the chamber and partially
 1827 because of pile up particles during the triggered TPC readout time, as shown in

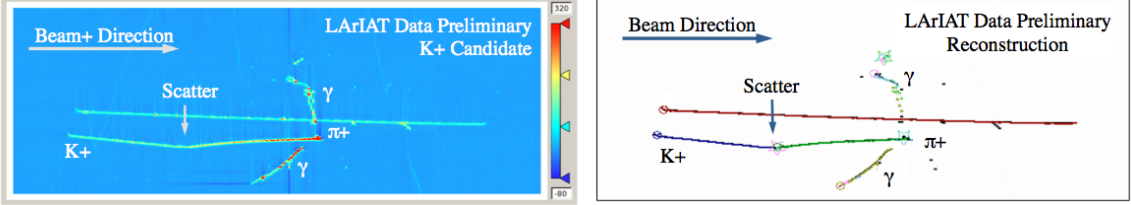


Figure 4.3: Kaon candidate event: on the right, event display showing raw quantities; on the left, event display showing reconstructed tracks. In the reconstructed event display, different colors represent different track objects. A kink is visible in the kaon ionization, signature of a hadronic interaction: the tracking correctly stops at the kink position and two tracks are formed. An additional pile-up track is so present in the event (top track in red).

1828 figure 4.3.

1829 We attempt to uniquely match one wire chamber track to one and only one recon-
 1830 structed TPC track. In order to determine if a match is present, we apply a geomet-
 1831 rical selection on the relative the position of the wire chamber and TPC tracks. We
 1832 start by considering only TPC tracks whose first point is in the first 2 cm upstream
 1833 portion of the TPC for the match. We project the wire chamber track to the TPC
 1834 front face where we define the coordinates of the projected point as x_{FF} and y_{FF} . For
 1835 each considered TPC track, we define ΔX as the difference between the x position of
 1836 the most upstream point of the TPC track and x_{FF} . ΔY is defined analogously. We
 1837 define the radius difference, ΔR , as $\Delta R = \sqrt{\Delta X^2 + \Delta Y^2}$. We define as α the angle
 1838 between the incident WC track and the TPC track in the plane that contains them.
 1839 If $\Delta R < 4$ cm, $\alpha < 8^\circ$, a match between WC-track and TPC track is found. We de-
 1840 scribe how we determine the value for the radius and angular selection in Section ??.
 1841 We discard events with multiple WC2TPC matches. We use only those TPC tracks
 1842 that are matched to WC tracks in the cross section calculation. Line 6 in Table 4.1
 1843 shows the number of events where a unique WC2TPC match was found.
 1844 In MC, we mimic the matching between the WC and the TPC track by construct-
 1845 ing a fake WC track using truth information at wire chamber four. We then apply
 1846 the same WC to TPC matching algorithm as in data.

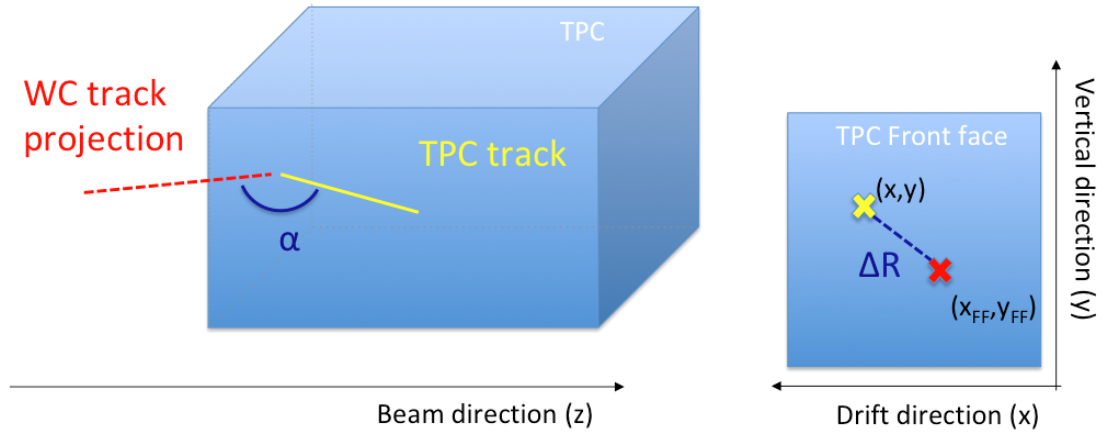


Figure 4.4: Visual rendering of the wire chamber to TPC match.

1847 4.3 The Thin Slice Method

1848 Once we have selected the pool of hadron candidates and we have identified the TPC
1849 track corresponding to the beamline event, we apply the thin slice method to measure
1850 the cross section, as the following sections describe.

1851 4.3.1 Cross Sections on Thin Target

1852 Cross section measurements on a thin target have been the bread and butter of
1853 nuclear and particle experimentalists since the Geiger-Marsden experiments [67]. At
1854 their core, this type of experiments consists in shooting a beam of particles with a
1855 known flux on a thin slab of material and recording the outgoing flux.

1856 In general even in the case of thin target, the target is not a single particle,
1857 but rather a slab of material containing many diffusion centers. The so-called “thin
1858 target” approximation assumes that the target centers are uniformly distributed in
1859 the material and that the target is thin compared to the projectile interaction length,
1860 so that no center of interaction sits in front of another. In this approximation, the
1861 ratio between the number of particles interacting in the target N_{Int} and the number of
1862 incident particles N_{Inc} on the target determines the interaction probability $P_{\text{Interacting}}$,

1863 which is the complementary to one of the survival probability $P_{Survival}$. Equation 4.2

$$P_{Survival} = 1 - P_{Interacting} = 1 - \frac{N_{Int}}{N_{Inc}} = e^{-\sigma_{TOT}n\delta X} \quad (4.2)$$

1864 describes the probability for a particle to survive the thin target. This formula relates
1865 the interaction probability to the total hadronic cross section (σ_{TOT}), the density of
1866 the target centers (n)¹ and the thickness of the target along the incident hadron
1867 direction (δX). If the target is thin compared to the interaction length of the process
1868 considered, we can Taylor expand the exponential function in equation 4.2 and find
1869 a simple proportionality relationship between the cross section and the number of
1870 incident and interacting particles, as shown in equation 4.3:

$$1 - \frac{N_{Int}}{N_{Inc}} = 1 - \sigma_{TOT}n\delta X + O(\delta X^2). \quad (4.3)$$

1871 Solving for the cross section, we find:

$$\sigma_{TOT} = \frac{1}{n\delta X} \frac{N_{Int}}{N_{Inc}}. \quad (4.4)$$

1872 4.3.2 Not-so-Thin Target: Slicing the Argon

1873 The interaction length of pions and kaons in argon is expected to be of the order
1874 of 50 cm for pions and 100 cm for kaons. Thus, the LArIAT TPC, with its 90 cm
1875 of length, is not a thin target. However, the fine-grained tracking of the LArIAT
1876 LArTPC allows us to treat the argon volume as a sequence of many adjacent thin
1877 targets.

1878 As described in Chapter 3, LArIAT wire planes consist of 240 wires each. The
1879 wires are oriented at +/- 60° from the vertical direction at 4 mm spacing, while the

1. The scattering center density in the target, n , relates to the argon density ρ , the Avogadro number N_A and the argon molar mass m_A as $n = \frac{\rho N_A}{m_A}$.

beam direction is oriented 3 degrees off the z axis in the XZ plane. The wires collect
 signals proportional to the energy loss of the hadron along its path in a $\delta X = 4$
 $\text{mm}/(\sin(60^\circ)\cos(3^\circ)) \approx 4.7$ mm slab of liquid argon. Thus, one can think to slice
 the TPC into many thin targets of $\delta X = 4.7$ mm thickness along the direction of the
 incident particle, making a measurement at each wire along the path.

Considering each slice j a “thin target”, we can apply the cross section calculation
 from Equation 4.4 iteratively, evaluating the kinetic energy of the hadron as it enters
 each slice, E_j^{kin} . For each WC2TPC matched particle, the energy of the hadron
 entering the TPC is known thanks to the momentum and mass determination by the
 tertiary beamline,

$$E_{FrontFace}^{kin} = \sqrt{p_{Beam}^2 - m_{Beam}^2} - m_{Beam} - E_{loss}, \quad (4.5)$$

where E_{loss} is a correction for the energy loss in the uninstrumented material between
 the beamline and the TPC front face. The energy of the hadron at each slab is
 determined by subtracting the energy released by the particle in the previous slabs.
 For example, at the j^{th} point of a track, the kinetic energy will be

$$E_j^{kin} = E_{FrontFace}^{kin} - \sum_{i < j} E_{Dep,i}, \quad (4.6)$$

where $E_{Dep,i}$ is the energy deposited at each argon slice before the j^{th} point as measured
 by the calorimetry associated with the tracking.

If the particle enters a slice, it contributes to $N_{Inc}(E^{kin})$ in the energy bin corresponding
 to its kinetic energy in that slice. If it interacts in the slice, it also contributes
 to $N_{Int}(E^{kin})$ in the appropriate energy bin. The cross section as a function of kinetic
 energy, $\sigma_{TOT}(E^{kin})$ will then be proportional to the ratio $\frac{N_{Int}(E^{kin})}{N_{Inc}(E^{kin})}$.

Our goal is to measure the total interaction cross section, independently from the
 topology of the interaction. Thus, we determine that a hadron interacted simply by

	min	max
X	1 cm	46 cm
Y	-15 cm	15 cm
Z	0 cm	86 cm

Table 4.2: Fiducial volume boundaries used to determine cross section interaction point.

requiring that the last point of the WC2TPC matched track lies inside the fiducial volume, whose boundaries are defined in Table 4.2. If the TPC track stops within the fiducial volume, its last point will be the interaction point; if the track crosses the boundaries of the fiducial volume, the track will be considered “through going” and no interaction point will be found. The only points of the hadronic candidate track considered to fill the N_{Inc}) and N_{Inc} plots are the ones contained in the fiducial volume.

4.3.3 Corrections to the Raw Cross Section

Equation 4.4 is a prescription for measuring the cross section in case of a pure beam of the hadron of interest and 100% efficiency in the determination of the interaction point. For example, if LArIAT had a beam of pure pions and were 100% efficient in determining the interaction point within the TPC, the pion cross section in each energy bin would be given by

$$\sigma_{TOT}^{\pi^-}(E_i) = \frac{1}{n\delta X} \frac{N_{\text{Int}}^{\pi^-}(E_i)}{N_{\text{Inc}}^{\pi^-}(E_i)}. \quad (4.7)$$

Unfortunately, this is not the case. In fact, the selection used to isolate pions in the LArIAT beam allows for the presence of some muons and electrons as background, while the kaon selection allows for a small percentage of protons (see Section 5.2.1). Also, the LArIAT TPC is not 100% efficient in determining the interaction point. Therefore we need to apply two corrections evaluated on the MC in order to

1920 extract the true cross section from LArIAT data: the background subtraction and
 1921 the efficiency correction. Still using the pion case as example, we estimate the pion
 1922 cross section in each energy bin changing Equation 4.7 into

$$\sigma_{TOT}^{\pi^-}(E_i) = \frac{1}{n\delta X} \frac{N_{Int}^{\pi^-}(E_i)}{N_{Inc}^{\pi^-}(E_i)} = \frac{1}{n\delta X} \frac{\epsilon^{Inc}(E_i)[N_{Int}^{TOT}(E_i) - B_{Int}(E_i)]}{\epsilon^{Int}(E_i)[N_{Inc}^{TOT}(E_i) - B_{Inc}(E_i)]}, \quad (4.8)$$

1923 where $N_{Int}^{TOT}(E_i)$ and $N_{Inc}^{TOT}(E_i)$ is the measured content of the interacting and
 1924 incident histograms for events that pass the event selection, $B_{Int}(E_i)$ and $B_{Inc}(E_i)$
 1925 represent the contributions from the background to the interacting and incident his-
 1926 tograms respectively, and $\epsilon^{Int}(E_i)$ and $\epsilon^{Inc}(E_i)$ are the efficiency corrections for said
 1927 histograms.

1928 As we will show in section 5.3, the background subtraction for the interacting
 1929 and incident histograms can be translated into a corresponding relative pion content
 1930 $C_{Interacting}^{\pi MC}(E_i)$ and $C_{Incident}^{\pi MC}(E_i)$ and the cross section re-written as follows

$$\sigma_{TOT}^{\pi^-}(E_i) = \frac{1}{n\delta X} \frac{\epsilon^{Inc}(E_i)}{\epsilon^{Int}(E_i)} \frac{C_{Int}^{\pi MC}(E_i)}{C_{Inc}^{\pi MC}(E_i)} \frac{N_{Int}^{TOT}(E_i)}{N_{Inc}^{TOT}(E_i)}. \quad (4.9)$$

1931 4.4 Procedure testing with truth quantities

1932 The (π^-, Ar) and (K^+, Ar) total hadronic cross section implemented in Geant4 can be
 1933 used as a tool to validate the measurement methodology. We describe here a closure
 1934 test done on Monte Carlo to prove that the methodology of slicing the TPC retrieves
 1935 the underlying cross section distribution implemented in Geant4 within the statistical
 1936 uncertainty.

1937 For pions and kaons in the considered energy range, the Geant4 inelastic model
 1938 adopted is “BertiniCascade”; the pion elastic cross sections are tabulated from on
 1939 Chips, while the kaon elastic cross sections are tabulated on Gheisha and Chips.

1940 For the validation test, we fire a sample of pions and a sample of kaons inside the

1941 LArIAT TPC active volume using the Data Driven Monte Carlo (see section 5.2.2).
1942 We apply the thin-sliced method using only true quantities to calculate the hadron
1943 kinetic energy at each slab in order to decouple reconstruction effects from possible
1944 issues with the methodology. For each slab of 4.7 mm length along the path of the
1945 hadron, we integrate the true energy deposition as given by the Geant4 transportation
1946 model. Then, we recursively subtracted it from the hadron kinetic energy at the TPC
1947 front face to evaluate the kinetic energy at each slab until the true interaction point is
1948 reached. Since the MC is a pure beam of the hadron of interest and truth information
1949 is used to retrieve the interaction point, no correction is applied. Doing so, we obtain
1950 the true interacting and incident distributions for the considered hadron, from which
1951 we derive the true MC cross section as a function of the hadron true kinetic energy.

1952 Figure 4.5 shows the total hadronic cross section for argon implemented in Geant4
1953 10.03.p1 (solid lines) overlaid with the true MC cross section as obtained with the
1954 sliced TPC method (markers) for pions on the left and kaons on the right; the total
1955 cross section is shown in green, the elastic cross section in blue and the inelastic
1956 cross section in red. The nice agreement with the Geant4 distribution and the cross
1957 section obtained with the sliced TPC method gives us confidence in the validity of
1958 the methodology.

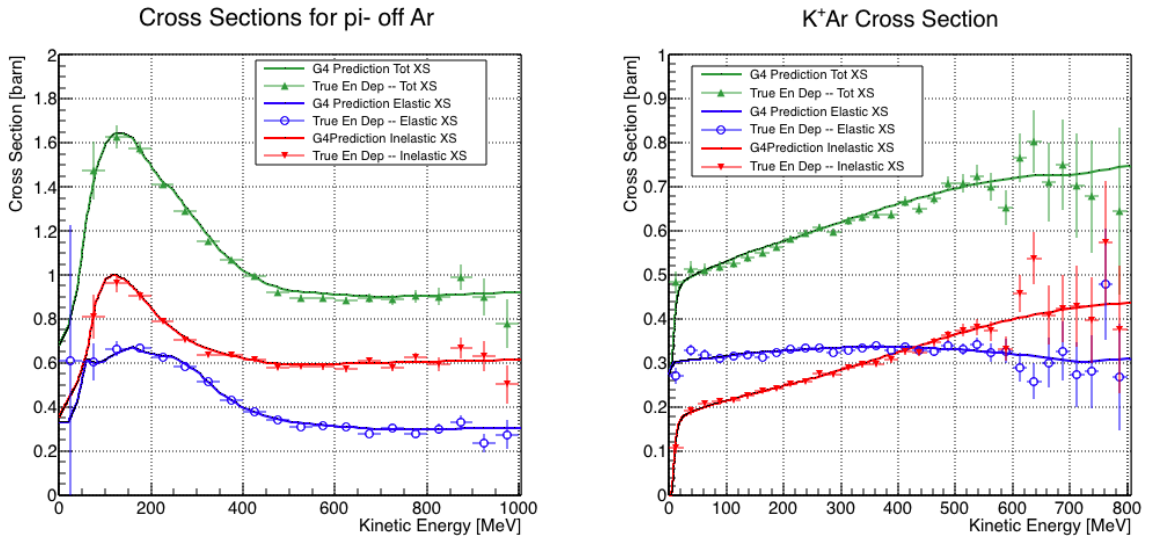


Figure 4.5: Hadronic cross sections for (π^- ,Ar) on the left and (K^+ ,Ar) on the right as implemented in Geant4 10.03.p1 (solid lines) overlaid the true MC cross section as obtained with the sliced TPC method (markers). The total cross section is shown in green, the elastic cross section in blue and the inelastic cross section in red.

1959 **Chapter 5**

1960 **Data and MC preparation for the**
1961 **Cross Section Measurements**

1962 “*Il dolce non lo mangi mai, ma qualche volta ti rifai.*
1963 *Abbracciami*”
1964 – Pietro Ciampi, 1971 –

1965 This chapter describes the work done on the data and Monte Carlo samples in
1966 preparation for the cross section analyses. This entails the choice of the datasets
1967 and the production of the information needed to construct the Monte Carlo Simula-
1968 tion (Section 5.1), the construction and use of said Monte Carlo simulation (section
1969 5.2), the study of backgrounds for the pion cross section (Section 5.3), the study of
1970 the energy loss between WC4 and TPC (Section 5.4), the study of the tracking in the
1971 TPC (Section 5.5), and study of the calorimetry response (Section 5.6).

1972 **5.1 Cross Section Analyses Data Sets**

1973 We choose LArIAT Run-II as the data period for the (π^- ,Ar) and (K^+ ,Ar) total
1974 hadronic cross section analyses. Data taking for the this period started on 03/15/2016

1975 and ended on 07/31/2016. Since we are interested in beamline and TPC information,
1976 we ask basic requirements on the operational status of the time of flight, wire chambers
1977 and TPC to form the good run list for this period, which we informally call “lovely
1978 runs”.

1979 The subset of lovely runs chosen for the (π^-, Ar) total hadronic cross section
1980 analysis includes only the -60A and -100A magnet configurations in negative polarity,
1981 even if LArIAT explored several other beamline configurations during Run-II. The -
1982 60A and -100A combined data set accounts for approximately 90% of the total Run-II
1983 negative polarity runs. The choice of the main two beamline settings limits the need
1984 for the production of many different MC sets and related corrections, still maintaining
1985 a high number of events.

1986 Similarly, the subset of lovely runs chosen for the (K^+, Ar) total hadronic cross
1987 section analysis includes only the +60A and +100A magnet configurations in positive
1988 polarity. It should be noted that kaons are extremely rare in the +60A sample, thus
1989 the data sample for the (K^+, Ar) cross section after the mass selection is about 90%
1990 +100A runs, as shown in Table 5.1.

1991 For the first measurements in LArIAT that uses both beamline and TPC infor-
1992 mation, we choose strict requirements on the reconstruction of the WC tracks, the
1993 so-called “Picky Track” sample (see Section 3.2.2). This choice presents two ad-
1994 vantages: the uncertainty on the momentum reconstruction for the “Picky Tracks”
1995 sample is smaller compared to the “High Yield” sample, and the comparison with
1996 the beamline MC results is straightforward. A possible future update and cross check
1997 of these analysis would be the use of the High Yield sample, where the statistics is
1998 about three times higher.

1999 The breakdown of beamline events as a function of the magnets settings is shown
2000 in Table 5.1. The choice of the data sets determines the production of beamline MC
2001 and serves as basis for the production of Data Driven MC, as shown in the next

2002 sections.

2003 **5.2 Construction of a Monte Carlo Simulation for** 2004 **LArIAT**

2005 For the simulation of LArIAT events and for the simulation of the datasets' particle
2006 make up, we use a combination of two MC generators: the G4Beamline Monte Carlo
2007 and the Data Driven single particle Monte Carlo (DDMC). We use the G4Beamline
2008 MC to simulate the particle transportation in the beamline and calculate the particle
2009 composition of the beam just after the fourth Wire Chamber (WC4). In order to
2010 simulate the beamline particles after WC4 and in the TPC, we use the DDMC.

2011 **5.2.1 G4Beamline**

2012 G4Beamline simulates the beam collision with the LArIAT secondary target, the
2013 energy deposited by the particles in the LArIAT beamline detectors, and the action
2014 of the LArIAT magnets, effectively accounting for particle transportation through the
2015 beamline from the LArIAT target until “Big Disk”, a fictional, void detector located
2016 just before the LArIAT cryostat. At the moment of this writing, G4Beamline does
2017 not simulated the responses of the beamline detectors. It is possible to interrogate the
2018 truth level information of the simulated particles in several points of the geometry.
2019 In order to ease the handshake between G4Beamline and the DDMC, we ask for
2020 the beam composition just after WC4. Since LArIAT data are taken under different

	I = 60 A	I = 100 A	Total
Data Events after $\pi/\mu/e$ Mass Selection	67068	71413	138481
Data Events after K Mass Selection	274	2563	2837

Table 5.1: Number of data events which fit the $\pi/\mu/e$ or K mass hypothesis as a function of magnet settings.

beam conditions, we need to simulate separately the beam composition according to the magnets' settings and the secondary beam intensity with G4Beamline. For the pion cross section analysis the relevant beam conditions are secondary beam energy of 64 GeV, negative polarity magnet with current of 100 A and 60 A. For the kaon cross section analysis the relevant beam conditions is a secondary beam energy of 64 GeV, positive polarity magnet with current of 100 A.

Beam Composition for Negative Pion Cross Section

Even if pions are by far the biggest beam component in negative polarity runs, the LArIAT tertiary beam is not a pure pion beam. While useful to discriminate between pions, kaons, and protons, the beamline detectors are not sensitive enough to discriminate among the lighter particles in the beam: electrons, muons and pions fall under the same mass hypothesis. Thus, we need to assess the contamination from beamline particles other than pions in the event selections used for the pion cross section analysis and correct for its effects. The first step of this process is assessing the percentage of electrons and muons in the $\pi/\mu/e$ beamline candidates via the G4Beamline MC. Since the beamline composition is a function of the magnet settings, we simulate separately events for magnet current of -60A and -100A. Figure 5.1 shows the momentum predictions from G4Beamline overlaid with data for the 60A runs (left) and for the 100A runs (right). The predictions for electrons, muons and pions have been staggered and their sum is area normalized to data. Albeit not perfect, these plots show a reasonable agreement between the momentum shapes in data and MC. We attribute the difference in shape to a two approximations performed in the MC. Firstly, G4Beamline lacks the simulation of the WC efficiency which is momentum dependent and leads to enhance the number events in the center of the momentum distribution. Secondly, G4Beamline stop tracking pions and their products if they decay in after WC1; in data, pion decays in flight can still create a

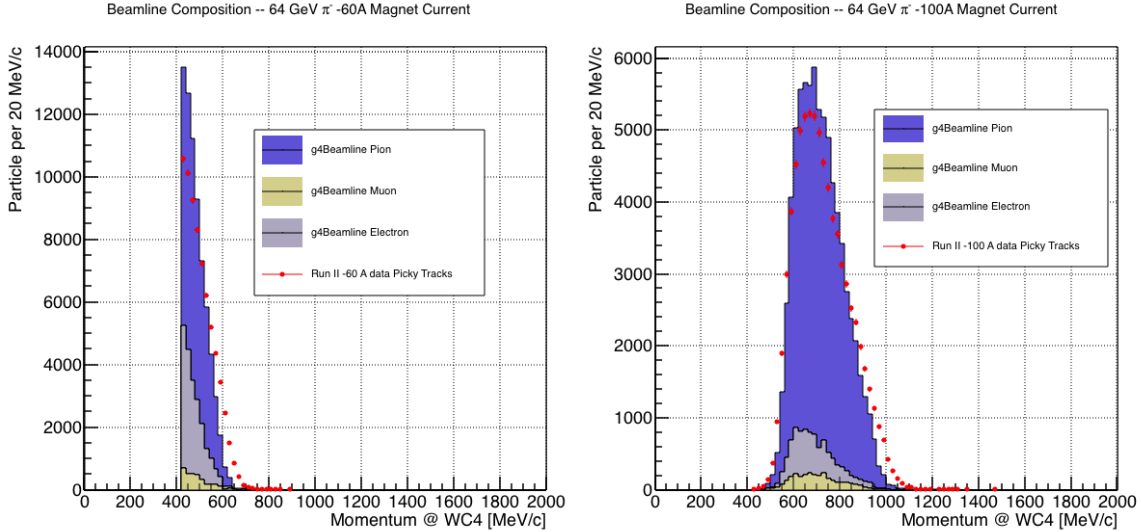


Figure 5.1: Beam composition for the -60A runs (left) and -100A runs (right). The solid blue plot represents the simulated pion content, the yellow plot represents the simulated muon content and the grey plot represents the simulated electron content. The plots are area normalized to the number of data events, shown in red.

	I = -60 A	I = -100 A
G4Pions	68.8 %	87.4 %
G4Muons	4.6 %	3.7 %
G4Electrons	26.6 %	8.9 %

Table 5.2: Simulated beamline composition per magnet settings

2047 trigger if the produced muon travels thought the beamline detectors. In the pion cross
 2048 section analysis, these differences between data and G4Beamline are accounted for as
 2049 a systematic uncertainty related to the beam composition (see Section 6.2.1).

2050 Table 5.2 shows the beam composition per magnet setting after the mass selection
 2051 according to the G4Beamline simulation.

2052 The estimated beam composition is used as a basis to estimate the background
 2053 contamination in the (π^-, Ar) cross section measurement, whose full treatment is
 2054 described in section 5.3.

2055 **Beam Composition for Positive Kaon Cross Section**

2056 In the positive polarity runs, the tertiary beam composition is mainly pions and
2057 protons. The left side of Figure 5.2 shows the predictions for the momentum spectra
2058 for the 100A positive runs according to G4Beamline (solid colors) overlaid with data
2059 (black points). Since the LArIAT beamline detectors can discriminate between kaons
2060 and other particles, we do not rely on the G4Beamline simulation to estimate the
2061 beamline contamination in the pool of kaon candidates (as in the case of the pion
2062 cross section), but rather we use a data driven approach. The basic idea of this data
2063 driven approach is to estimate the bleed over from high and low mass peaks under
2064 the kaon peak by fitting the tails of the $\pi/\mu/e$ and proton mass distributions, as
2065 shown in Figure 5.2 right side. Since the shape of the tails is unknown, the estimate
2066 is done multiple times varying the range and shape for reasonable functions. For
2067 example, to estimate the proton content under the kaon peak, we start by fitting the
2068 left tail of the proton mass distribution with a gaussian function between $650 \text{ MeV}/c^2$
2069 and $750 \text{ MeV}/c^2$. We extend the fit function under the kaon peak and integrate the
2070 extended fit function between $350-650 \text{ MeV}/c^2$. We integrate the mass histogram
2071 in the same range and calculate the proton contamination as the ratio between the
2072 two integrals. We repeat this procedure for several fit shapes (gaussian, linear and
2073 exponential functions) and tail ranges. Finally, we calculate the contamination as
2074 the weighted average of single estimates, where the weights are calculated to be the
2075 $1./|1 - \chi^2|$ of the tail fits. The procedure is repeated for lighter particles mass peak
2076 independently. With 12 iterations of this method we find a proton contamination of
2077 $5.0 \pm 2.0 \%$ and a contamination from the lighter particles of $0.2 \pm 0.5 \%$. The
2078 estimate of the proton background is currently not used in the kaon cross section
2079 analysis, but it is a fundamental step to retrieve the true kaon cross section which
2080 will be implemented in the further development of the analysis.

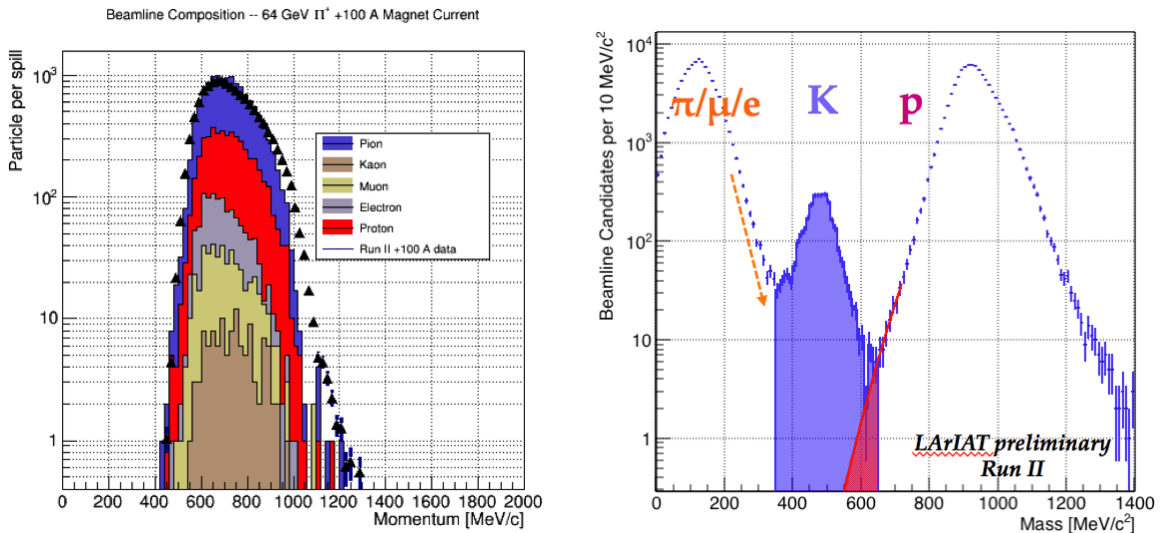


Figure 5.2: *Left:* Beam composition for the +100A runs after WC4 (no mass selection applied). The solid colors represent the contributions from the G4Beamline simulated particles: blue plot represents the simulated pion content, the yellow plot represents the simulated muon content and the grey plot represents the simulated positron content, the red the proton content and the mustard the kaon content. The plots are area normalized to the number of data events, shown in black. *Right:* Mass distribution for the Run-II positive runs, where the area under the kaon mass peak is highlighted in purple. The area under the extension of a possible fit for the proton tail is highlighted in red.

2081 **5.2.2 Data Driven MC**

2082 The Data Driven single particle Monte Carlo (DDMC) is a single particle gun which
2083 simulates the particle transportation from WC4 into the TPC leveraging on the beam-
2084 line data information. The DDMC uses the data momentum and position at WC4
2085 to derive the event generation: a general sketch of the DDMC workflow is shown in
2086 Figure 5.3.

2087 When producing a DDMC sample, beamline data from a particular running pe-
2088 riod and/or running condition are selected first. For example, data for the negative
2089 60A runs and for the negative 100A runs inform the event generation stage of two
2090 different DDMC samples. Figure 5.4 schematically shows the data quantities of in-
2091 terest leveraged from data: the momentum (P_x, P_y, P_z) and position (X, Y) at WC4.
2092 For each data event, we obtain the particle position (X, Y) at WC4 directly from the
2093 data measurement; we calculate the components of the momentum using the beam-
2094 line measurement of the momentum magnitude in conjunction with the hits on WC3
2095 and WC4 to determine the direction of the momentum vector, as described in section
2096 3.2.2. The momentum and position of the selected data form a 5-dimensional tuple,
2097 which we sample thousands of times through a 5-dimensional hit-or-miss sampling
2098 procedure to generate the MC events. This sampling generates MC events with the
2099 same momentum and position distributions as data, with the additional benefit of
2100 accounting for the correlations between the P_x, P_y, P_z, X, Y variables. As an example,
2101 the results of the DDMC generation compared to data for the kaon +100A sample
2102 are shown in figure 5.5 for the P_z, X and Y distributions; as expected, MC and data
2103 agree within the statistical uncertainty by construction. A LArSoft simulation mod-
2104 ule then launches single particle MC from $z = -100$ cm (the location of the WC4)
2105 using the generated events. The particles are free to decay and interact in their path
2106 from WC4 to the TPC according to the Geant4 simulation.

2107 Using the DDMC technique ensures that the MC and data particles have very

2108 similar momentum, position and angular distributions at WC4 and allows us to use
 2109 the MC sample in several occasions: to estimate the background contamination to
 2110 the pion cross section (see Section 5.3), to calibrate the energy loss upstream of the
 2111 TPC (see Section 5.4), or to study the tracking and the calorimetric performance
 2112 (sections 5.5 and 5.6). A small caveat is in order here: the DDMC is a single particle
 2113 Monte Carlo, which means that the beam pile-up is not simulated.

2114 We generate six samples for the pion cross section measurement: three samples
 2115 of ~ 330000 pions, muons and electrons to simulate the negative 60A runs, and three
 2116 samples of ~ 340000 pions, muons and electrons for the negative 100A runs. We
 2117 generate a sample of 195000 kaons for the kaon cross section analysis.

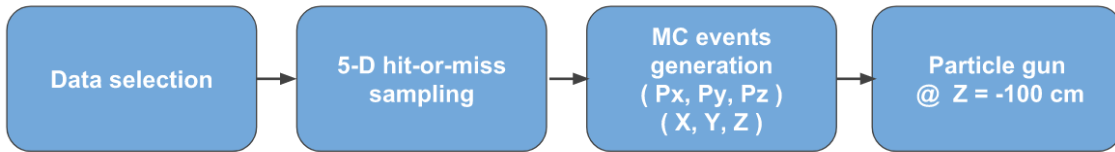


Figure 5.3: Workflow for Data Driven single particle Monte Carlo production.

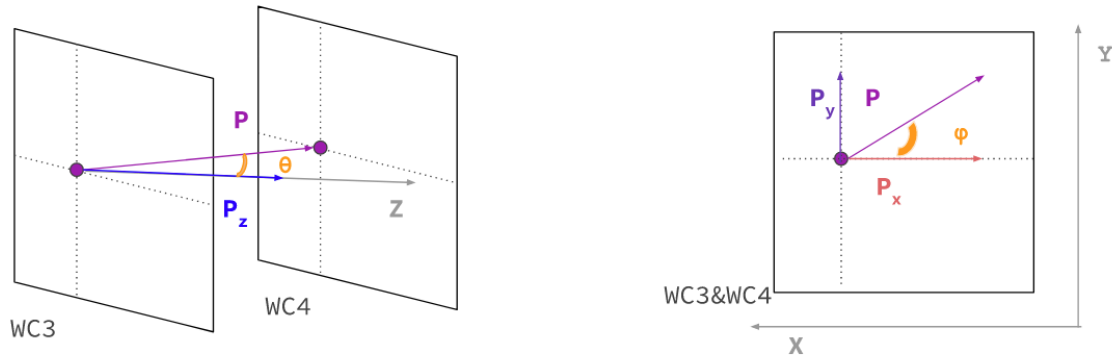


Figure 5.4: Scheme of the quantities of interest for the DDMC event generation:
 P_x, P_y, P_z, X, Y at WC4.

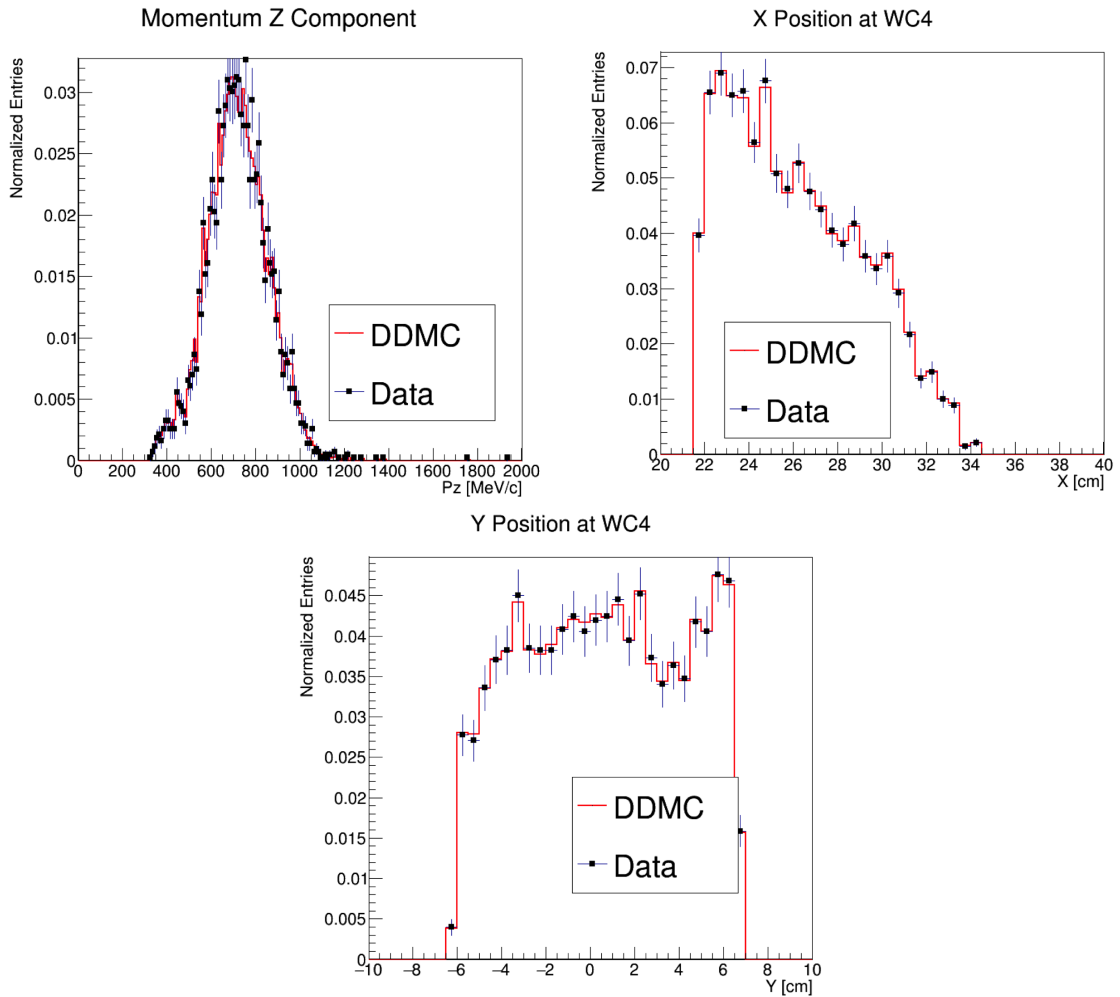


Figure 5.5: Comparison between generated quantities and data distributions for the 100A kaon sample: Z component of the momentum at WC4 (top left), X position at Wire Chamber 4 (top right), Y position at Wire Chamber 4 (bottom).

2118 **5.3 Estimate of Backgrounds in the Pion Cross**
2119 **Section**

2120 We use the beamline simulation and the DDMC simulation to estimate the back-
2121 ground in the total hadronic pion cross section. Two categories of background exists
2122 for the negative pion cross section measurement: the one related to the pion interac-
2123 tion in the chamber, discussed in Section 5.3.1 and the one related to the beamline
2124 contamination, discussed in Section 5.3.2.

2125 **5.3.1 Background from Pion Capture and Decay**

2126 Our goal is to measure the total hadronic cross section for negative pions in argon.
2127 Since pion capture can be classified as an electromagnetic process and pion decay is a
2128 week process, capture and decay represent unwanted interactions. We present here a
2129 study of capture and decay in Monte Carlo and the solution we adopted to mitigate
2130 their occurrence in the data sample.

2131 For this MC study, we use a sample of MC pions generated according to the
2132 –60A beam profile with the DDMC (see Section 5.2.2). It is important to notice
2133 that capture occurs predominantly at rest, while decay may occur both in flight and
2134 at rest. Thus, we can highly mitigate capture and decay at rest by removing pions
2135 which would release all their energy in the TPC and stop. This translates into a
2136 momentum selection, where we keep only events whose WC momentum is above a
2137 certain threshold. Figure 5.6 shows the true momentum distribution for the primary
2138 pions¹ that arrive to the TPC (pink), that capture (green) or decay (blue) inside the
2139 TPC, on a linear scale (left) and on a log scale (right) vertical axis.

1. We use here the Geant4 denomination “primary” to indicate that the pion considered does not undergo interactions modifying its energy before getting to the TPC. In fact, not every pion shot from wire chamber four will arrive to the TPC as primary, some will decay or interact before the TPC.

2140 In order to choose the selection value for the wire chamber momentum, it is
2141 beneficial to estimate the ratio of events which capture or decay that survive the
2142 selection in MC as a function of the momentum threshold, and compare it with the
2143 survival ratio for all the 60A events. This is done in figure 5.7. We define the survival
2144 ratio simply as the number of events surviving the true momentum selection divided
2145 by the number of events of that category. We calculate the survival ratio separately
2146 for the three event categories explained above: total (pink), capture (green) and decay
2147 (blue). Selecting pions with momentum greater than 420 MeV/c reduces the capture
2148 events by 99% while maintaining about 80% of the 60A data sample and almost
2149 the entire 100A sample. Figure 5.8 shows the ratio of events which end their life in
2150 capture (green) or decay (blue) over the total number of events as a as a function of
2151 the true momentum at wire chamber four. This ratio is slightly dependent on the
2152 inelastic cross section implemented in Geant4, as we are able to register a pion capture
2153 (or decay) only if it did not interact inelastically in the TPC. We choose a momentum
2154 threshold of 420 MeV/c because the percentage of capture events drops below 1% and
2155 the percentage of decays is never above 2% for momenta greater than 420 MeV/c.
2156 After the momentum selection, we evaluate the contribution of capture and decay to
2157 be a negligibly small background to the cross section measurement compared to the
2158 background related to the beamline which we will address in the next section.

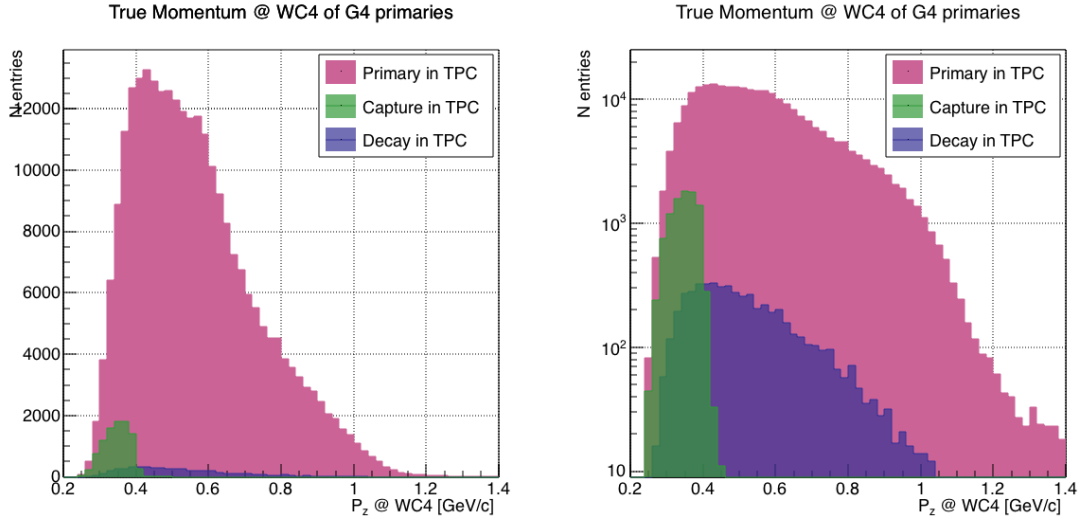


Figure 5.6: True momentum distribution at wire chamber 4 for every simulated pion arriving in the TPC (pink), ending its life in capture (green) or in decay (blue) in the TPC, linear vertical axis on the left, logarithmic on the right.

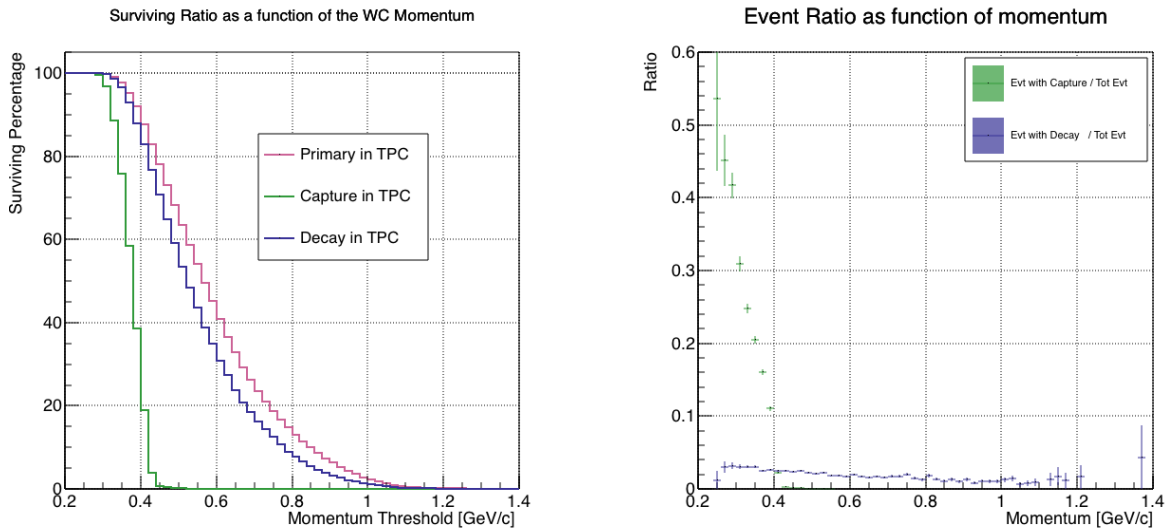


Figure 5.7: Survival ratio as a function of selection threshold on true momentum at wire chamber four for every simulated pion arriving in the TPC (pink), capture (green) or in decay (blue).

Figure 5.8: Ratio between the capture (green) and decay (blue) events over the total number of events as a function of the true momentum at wire chamber four.

2159 **5.3.2 Contributions from the Beamline Background**

2160 We define beamline background every TPC track matched to the WC track which is
2161 not a primary pion. Potentially, there are 4 different types of beamline background:

2162 1) electrons,

2163 2) muons,

2164 3) secondaries from pion events,

2165 4) matched pile up events.

2166 The first step to quantify the effect of the beamline background on the pion cross
2167 section is to estimate what percentage of events used in the cross section calculation
2168 is not a primary pion. We start by noting that the last type of background, the
2169 “matched pile up” events, is a negligible fraction, because of the definition of the
2170 WC2TPC match: we deem the probability of a single match with a halo particle in
2171 the absence of a beamline particle² negligibly small. As shown in Section 5.2.1, we
2172 use G4Beamline to estimate the percentage of pions, muons and electrons at WC4,
2173 obtaining the composition shown in Table 5.2. The next step is to simulate those
2174 pions, muons and electrons from WC4 to the TPC with the DDMC and evaluate their
2175 contribution to the cross section. To do so, we start by simulating the same number
2176 of electrons, muons and pions with the DDMC and we apply the same selection chain
2177 (i.e. track multiplicity rejection, WC2TPC acceptance and shower rejection) on the
2178 three samples. The number of events per particle species surviving this selection is
2179 shown on table 5.3. In order to reproduce the closest make up of the beam to data,
2180 we weight each event of a given particle species according to the estimated beam
2181 composition. In case of 60A runs, for example, the weights are 0.688 for pions, 0.046
2182 for muons and 0.266 for electrons.

2. Events with multiple WC2TPC matches are always rejected.

	Magnet Current -60A			Magnet Current -100 A		
	MC π^-	MC μ^-	MC e^-	MC π^-	MC μ^-	MC e^-
Total Initial events	334500	334500	334500	344500	344500	344500
After Multiplicity Rejection	330668	333420	198065	326576	344208	201380
After WC2TPC Selection	218239	296333	91139	230418	300228	98834
Evts After Shower Rejection	208063	288914	20293	219882	293585	17780
Selection Survival Rate	62.3%	86.6%	6.1%	63.8%	85.5%	5.2%
Beam Composition @WC4	68.8%	4.6 %	26.6 %	87.4 %	3.7 %	8.9 %
Beam Composition @TPC FF	88.5%	8.2%	3.3 %	94.0%	5.3%	0.7%

Table 5.3: MC selection flow per particle species.

2183 It should be noted that pions may interact hadronically in the steel or in the
 2184 non-instrumented argon upstream to the TPC front face while travelling the length
 2185 of between WC4 and the TPC. Or, they could decay in flight between WC4 and the
 2186 TPC. One of the interaction products can leak into the TPC and be matched with the
 2187 WC track, contributing to the pool of events used for the cross section calculation. We
 2188 call this type of particles “secondaries” from pion events, with a terminology inspired
 2189 by Geant4. We estimate the number of secondaries using the DDMC pion sample.
 2190 The percentage of secondaries is given by the number of matched WC2TPC tracks
 2191 whose corresponding particle is not flagged as primary by Geant4. The secondary to
 2192 pion ratio is 4.9% in the 60A sample and 4.3% in the 100A sample.

2193 We evaluate the beamline background contribution to the cross section by pro-
 2194 ducing the interacting and incident histograms for the events surviving the selection,
 2195 staggering the contributions for each particle species, as shown in Figure 5.9. From
 2196 those histograms, we are able to evaluate the contribution of pions and beamline
 2197 backgrounds to each bin of the interacting and incident histograms separately and
 2198 obtain the relative pion content. The relative pion content in each bin for the inter-
 2199 acting and incident histograms represents the correction applied to data. We take

here the interacting histogram as example, noting that the derivation of the correction for the incident histogram is identical. The number of entries in each bin of the interacting plot (Figure 5.9 left) is $N_{\text{Int}}^{\text{TOT}}(E_i)$, equal to the sum of the pions and beamline backgrounds in that bin, namely

$$N_{\text{Int}}^{\text{TOT}}(E_i) = N_{\text{Int}}^{\pi}(E_i) + \underbrace{N_{\text{Int}}^{\mu}(E_i) + N_{\text{Int}}^e(E_i) + N_{\text{Int}}^{\text{Secondary}}(E_i)}_{B_{\text{Int}}(E_i)}. \quad (5.1)$$

Thus, the relative pion content to each bin in MC can be calculated as follows

$$C_{\text{Int}}^{\pi MC}(E_i) = \frac{N_{\text{Int}}^{\pi MC}}{N_{\text{Int}}^{\text{TOTMC}}(E_i)} = \frac{N_{\text{Int}}^{\text{TOTMC}}(E_i) - B_{\text{Int}}^{MC}(E_i)}{N_{\text{Int}}^{\text{TOTMC}}(E_i)}. \quad (5.2)$$

In order to evaluate the pion content of each bin in data, we scale the measured bin by the corresponding relative pion content found in MC, as follows

$$N_{\text{Int}}^{\pi RecoData} = N_{\text{Int}}^{\text{TOTData}}(E_i) - B_{\text{Int}}^{\text{Data}}(E_i) = C_{\text{Int}}^{\pi MC}(E_i)N_{\text{Int}}^{\text{TOTData}}(E_i). \quad (5.3)$$

The pion content is evaluated separately in the interacting and incident histograms. Their ratio determines a correction to the measured raw cross section. For example, the measured raw cross section of a sample with enhanced muons content will tend to be lower than the raw cross section of a muon free sample. This is because most of the muons will cross the TPC without stopping, thus contributing almost exclusively to the incident histogram, forcing the pion content to be lower in the incident histogram than in the interacting; thus, the correction will tend to enhance the cross section.

2215 **5.4 Estimate of Energy Loss before the TPC**

2216 The beamline particles travel a path from where their momentum is measured in
2217 the beamline until they are tracked again inside the TPC. In the LArIAT geometry,
2218 a particle leaving the WC4 will encounter the materials listed in Table 5.4 before
2219 being registered again. The energy lost by the particle in this non-instrumented
2220 material modifies the particle's kinetic energy and directly affects the cross section
2221 measurement, as shown in equation 4.5.

Material	density [g/cm ³]	width [cm]
Fiberglass laminate (G10)	1.7	1.28
Liquid Argon	1.4	3.20
Stainless Steel	7.7	0.23
Titanium	4.5	0.04
Air	$1.2 \cdot 10^{-3}$	89.43
Plastic Scintillator	1.03	1.20 (+ 1.30)

Table 5.4: LArIAT material budget from WC4 to the TPC Front Face.

We derive an estimate of the energy loss between the beamline momentum measurement and the TPC (E_{loss}) from the pion and kaon DDMC samples, since this quantity is not measurable directly on data. The E_{loss} distribution for the 60A and 100A pion sample is shown in figure 5.10, left and right respectively. The E_{loss} distribution for the whole kaon sample is shown in figure 5.11. A clear double peaked structure is visible, which is due to the particles either missing or hitting the HALO paddle: a schematic rendering of this occurrence is shown in figure 5.12. The kinematic at WC4 determines the trajectory of a particle and whether or not it will hit the halo paddle. In figure 5.13 , we plot the true horizontal component of the momentum P_x versus the true X position at WC4 for pions missing the halo paddle (left) and for pions hitting the halo paddle (right) for the -60A MC simulation runs – analogous plots are obtained with the -100A pion simulation and with the kaon simulation. These distributions can be separated drawing a line in this position-momentum space.

We use a logistic regression [13] as a classifier to find the best separating line, shown in both plots as the red line. We classify as “hitting the halo paddle” all pions whose P_x and X are such that

$$P_x + 0.02 * X - 0.4 < 0$$

and as “missing the halo paddle” all pions whose P_x and X are such that

$$P_x + 0.02 * X - 0.4 > 0,$$

where the coefficients of the line are empirically found by the logistic regression estimation. Overall, this simple method classifies in the right category (hit or miss) about 86% of the pion events. In MC, we assign $E_{loss} = 32 \pm 4$ MeV for pion events classified as “hitting the halo paddle”; we assign $E_{loss} = 24 \pm 3$ MeV for pion events classified as “missing the halo paddle”. We apply the same classifier on data.

A scan of the simulated geometry showed an excess of 3 cm of uninstrumented argon compared with the surveyed detector geometry. We account for this difference by assigning in data $E_{loss} = 24 \pm 6$ MeV for pion events classified as “hitting the halo paddle” and $E_{loss} = 17 \pm 6$ MeV for pion events classified as “missing the halo paddle”, where the uncertainty is derived as the standard deviation of the double peaked distribution.

The summary of the values for used for E_{Loss} for the pion sample is listed in table 5.5 with the analogous results for the study on the kaon case.

	E_{loss} [MeV]	
	Hitting Halo	Missing Halo
Pion MC	32 ± 4	24 ± 3
Pion Data	25 ± 6	17 ± 6
Kaon MC	38 ± 6	31 ± 5
Kaon Data	26 ± 7	22 ± 7

Table 5.5: Energy loss for pions and kaons.

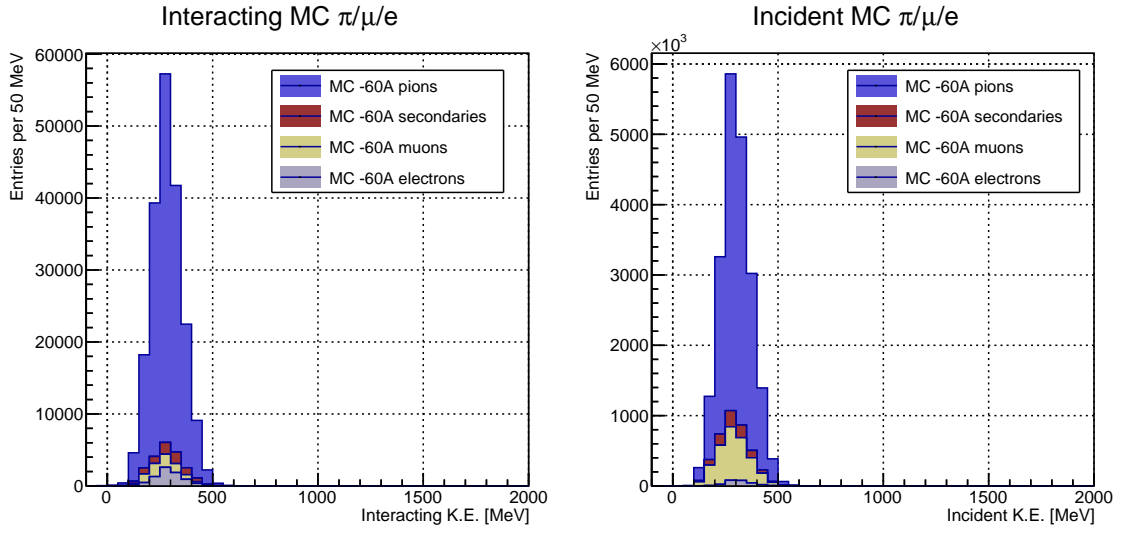


Figure 5.9: Left: staggered contributions to the interacting kinetic energy distribution for electron (grey), muons (yellow) and pion (blue) in the 60A simulation sample. Right: staggered contributions to the incident kinetic energy distribution for electron (grey), muons (yellow) and pion (blue) in the 60A simulation sample.

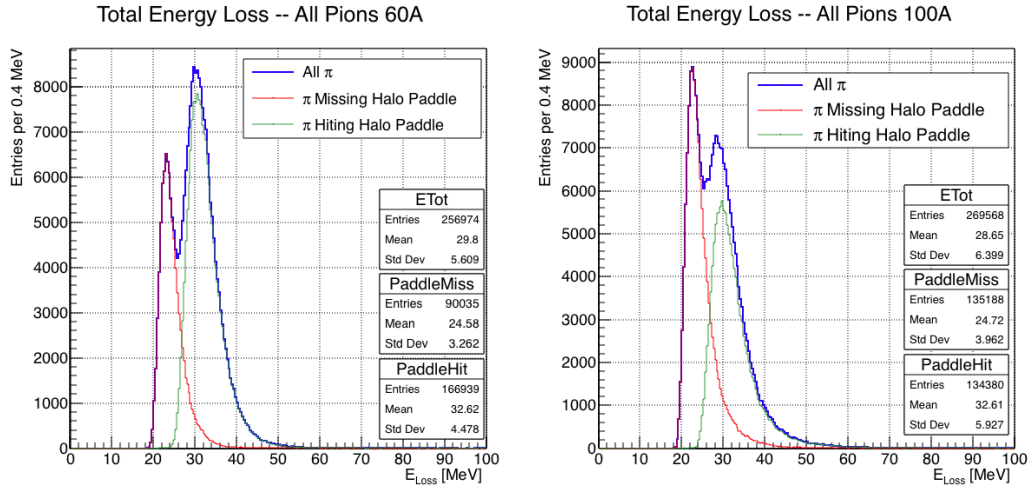


Figure 5.10: True energy loss between WC4 and the TPC front face according to the MC simulation of negative pions of the 60A runs (left) and of the 100A runs (right). The distribution for the whole data sample is shown in blue, the distribution for the pions missing the halo is shown in red, and the distribution for the pions hitting the halo is shown in green.

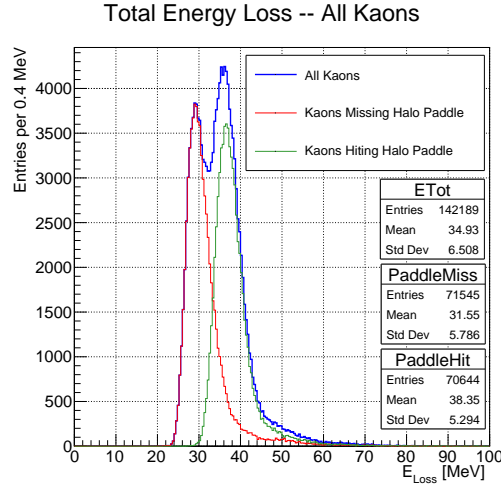


Figure 5.11: True energy loss between WC4 and the TPC front face according to the MC simulation of positive kaons in the 60A and 100A combined sample. The distribution for the whole data sample is shown in blue, the distribution for the kaons missing the halo is shown in red, and the distribution for the kaons hitting the halo is shown in green.

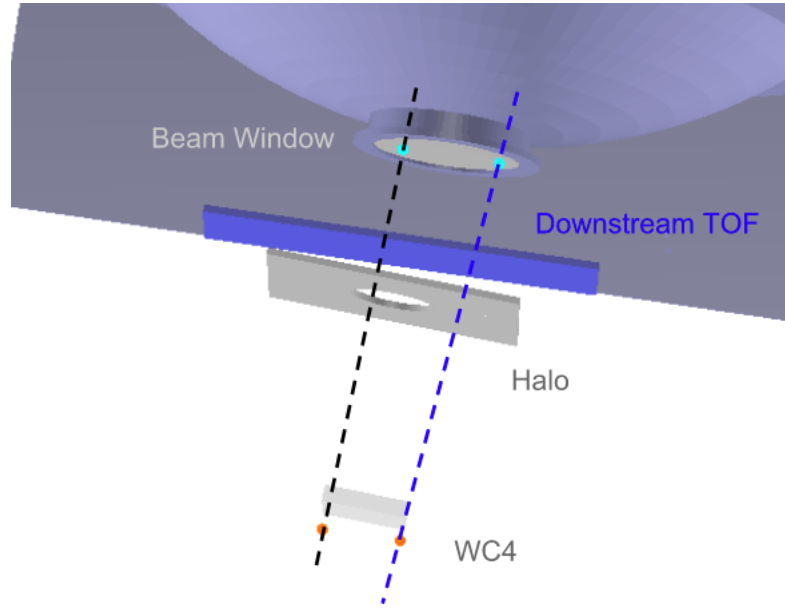


Figure 5.12: Schematic rendering of the particle path between WC4 and the TPC front face. The paddle with the hollow central circle represents the Halo paddle. We illustrate two possible trajectories: in black, a trajectory that miss the paddle and goes through the hole in the Halo, in blue a trajectory that hits the Halo paddle and goes through the scintillation material.

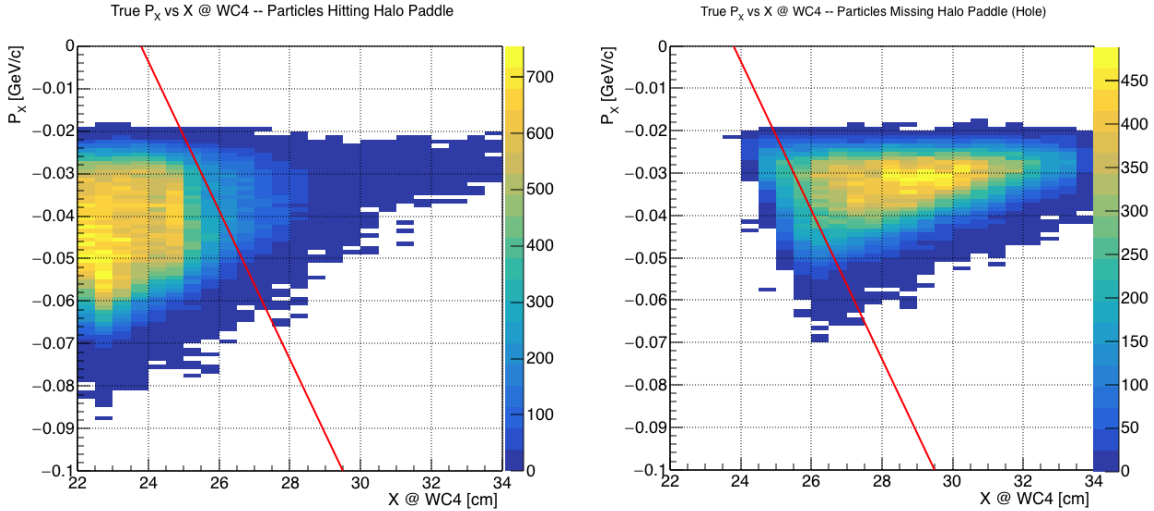


Figure 5.13: Horizontal component of the true momentum vs the horizontal position at WC4 for MC simulated pions of the 60A runs. The plot on the left shows the distribution for pion that miss the halo paddle and the plot on the right shows the distributions for pions that hit the halo. The form of the classifier is overlaid to both plots (red line).

2235 5.5 Tracking Studies

2236 The tracking of hadrons in the TPC determines both the beamline to TPC hand-
 2237 shake and the identification of the interaction point within the TPC. Thus, it plays
 2238 a fundamental role in the cross section measurements. We performed several studies
 2239 geared towards the optimization of the package for tracking in the TPC. In particular,
 2240 we studied a suitable set of parameters for the WC2TPC match and we optimized
 2241 the clustering algorithm to maximize the efficiency of finding the interaction point on
 2242 MC. Given the technical nature of these studies, we report them in Appendix B. We
 2243 report here the evaluation of the angular resolution of the tracking algorithm in data
 2244 and MC, due to its implication on the physics measurement.

2245 5.5.1 Angular Resolution

2246 Scope of this study is to understand and compare the tracking performances and
 2247 angular resolution of the TPC tracking on data and MC. We use the angular resolution

2248 of the tracking to determine the value of smallest angle that we can reconstruct with
2249 a non-zero efficiency, effectively determining a selection on the angular distribution
2250 of the cross section measurement due to the tracking performance.

2251 We start by selecting all the WC2TPC matched tracks used for the cross section
2252 analysis. These tracks can contain from a minimum of 3 3D-space points to a maxi-
2253 mum of 240 3D-space points. We fit a line to all the 3D-space points associated with
2254 the track. For each track we calculate the average distance between each point in
2255 space and the fit line as follows

$$\bar{d} = \frac{\sum_i^N d_i}{N}, \quad (5.4)$$

2256 where N is the number of 3D-space points of the track and d_i is the distance of the
2257 i -th space point to the line fit. Several tests to compare the goodness of fit between
2258 data and MC have been considered. We decided to use \bar{d} for its straightforward
2259 interpretation. The \bar{d} distribution for data and MC is shown in Figure 5.16 for pions
2260 and in Figure 5.18 for kaons and shows a relatively good agreement between data and
2261 MC.

2262 A visual representation of the procedure used to evaluate the angular resolution
2263 is shown in Figure 5.14. For each track, we order the space points according to their
2264 Z position along the positive beam direction (panel a) and we split them in two sets:
2265 the first set contains all the points belonging to the first half of the track and the
2266 second set contains all the points belonging the second half of the track. We remove
2267 the last four points in the first set and the first four points in the second set, so to
2268 have a gap in the middle of the original track (panel b). We fit the first and the second
2269 set of points with two lines (panel c). We then calculate the angle between the fit of
2270 the first and second half α (panel d). The angle α determines the spatial resolution
2271 of the tracking. The distributions for data and MC for α are given in Figure 5.17 for
2272 pions and in Figure 5.19 for kaons. The mean of the data and MC angular resolution
2273 are reported in Table tab:AngRes for pions and kaons in data and MC.

2274 Interaction angles smaller than the angle resolution are indistinguishable for the
 2275 reconstruction. Therefore, we assess our ability to measure the cross section to be
 2276 limited to interaction angles greater than 5.0 deg. More accurate studies of the angular
 2277 resolution as a function of the kinetic energy and track length, albeit interesting, are
 2278 left for an improvement of the analysis.

2279 It is beneficial to take a moment to describe the definition of interaction angle.
 2280 In case of elastic scattering, the definition is straightforward: the interaction angle is
 2281 the angle between the incoming and outgoing hadron, i.e.

$$\theta = \cos^{-1} \left(\frac{\vec{p}_{\text{incoming}} \cdot \vec{p}_{\text{outgoing}}}{|\vec{p}_{\text{incoming}}| |\vec{p}_{\text{outgoing}}|} \right). \quad (5.5)$$

2282 In case of inelastic scattering, the presence of several topologies requires a more
 2283 complex definition, as shown in figure 5.15. We define the scattering angle as the
 2284 biggest of the angles between the incoming hadron and the visible daughters, where
 2285 the visible daughters are charged particles that travel more than 0.47 cm in the
 2286 detector (see panel a); in case all the daughters are invisible, the angle is assigned
 2287 to be 90 deg (see panel b). We chose this working definition of scattering angle
 2288 for inelastic scattering keeping in mind how our tracking reconstruction works: the
 2289 tracking will stop correctly non of the daughters are is visible in the detector and it
 2290 is likely to stop correctly if multiple daughters form an interaction vertex. The only
 2291 “dangerous” case is the production of one charged daughter plus neutrals, which we
 2292 can study with this working definition of scattering angle (see panel c).

2293 We can see the effects of the angular resolution on the cross section by plotting the
 2294 true Geant4 cross section for interaction angles greater than a minimum interaction

	Data	MC
Pions	$\bar{\alpha}_{Data} = (5.0 \pm 4.5) \text{ deg}$	$\bar{\alpha}_{MC} = (4.5 \pm 3.9) \text{ deg}$
Kaons	$\bar{\alpha}_{Data} = (4.3 \pm 3.7) \text{ deg}$	$\bar{\alpha}_{MC} = (4.4 \pm 3.6) \text{ deg}$

Table 5.6: Angular resolution for Pion and Kaon tracking in both data and MC.

angle. Figure 5.20 shows the true Geant4 cross section for interaction angles greater than 0 deg (green), 4.5 deg (red), 5.0 deg (blue) and 9.0 deg (yellow). A small 0.5 deg systematic shift between the mean of the data and MC angular resolution is present.

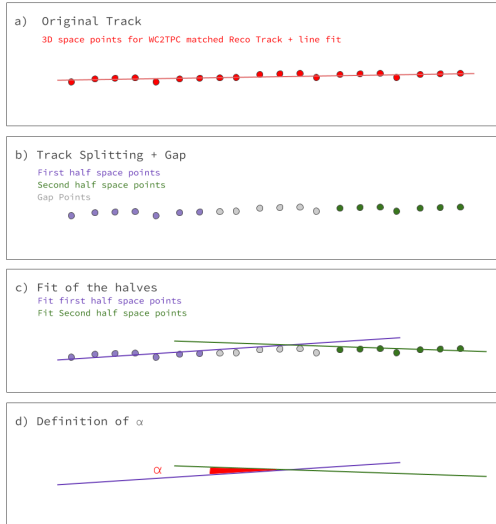


Figure 5.14: A visual representation of the procedure used to evaluate the angular resolution.

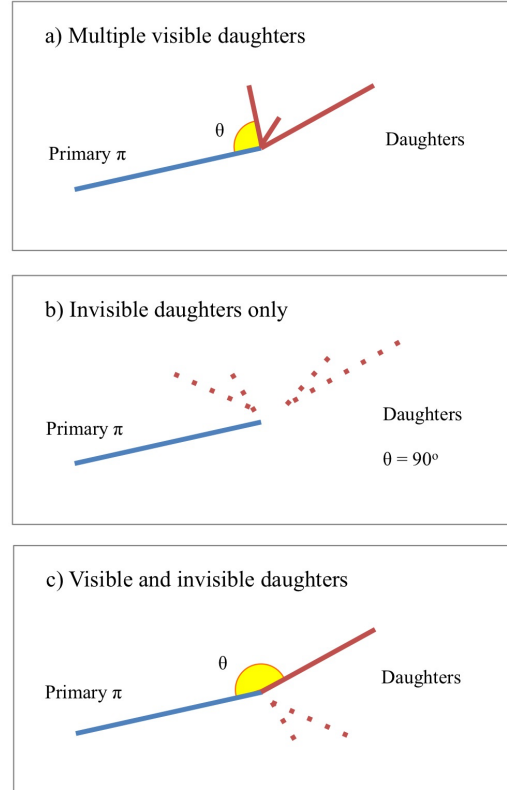


Figure 5.15: A visual representation of the scattering angle definition in case of inelastic scattering.

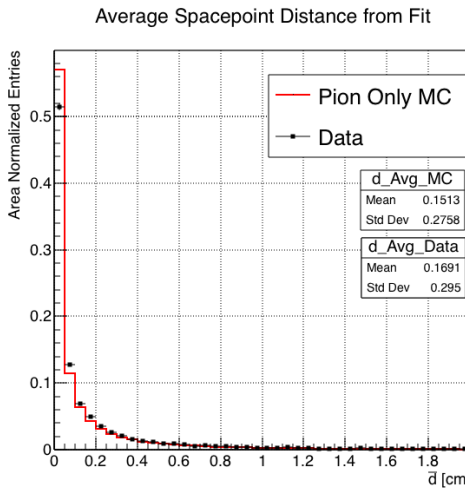


Figure 5.16: Distributions of the average distance between each 3D point in space and the fit line, \bar{d} for the data used in the pion cross section analysis and the pion only DDMC. The distributions are area normalized.

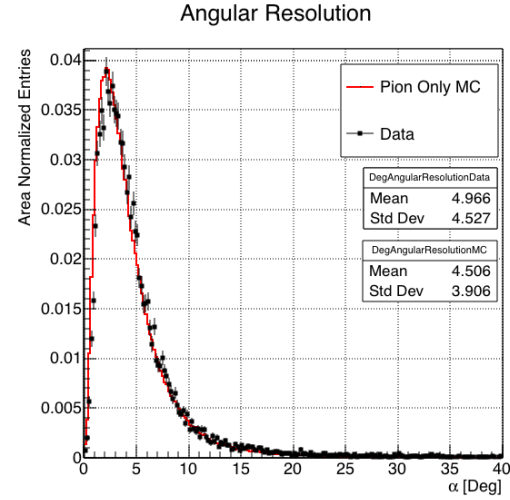


Figure 5.17: Distributions of angular resolution α for data used in the pion cross section analysis and pion only DDMC. The distributions are area normalized.

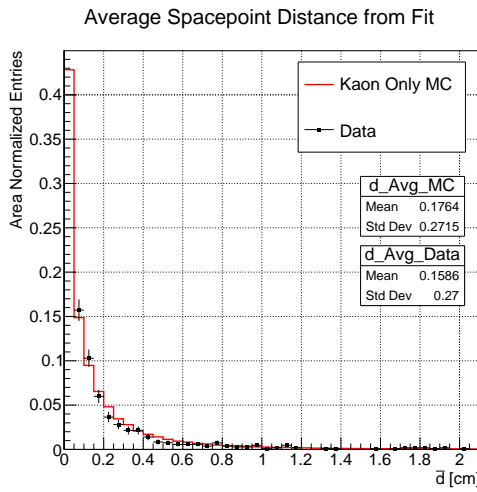


Figure 5.18: Distributions of the average distance between each 3D point in space and the fit line, \bar{d} for the data used in the kaon cross section analysis and the kaon only DDMC. The distributions are area normalized.

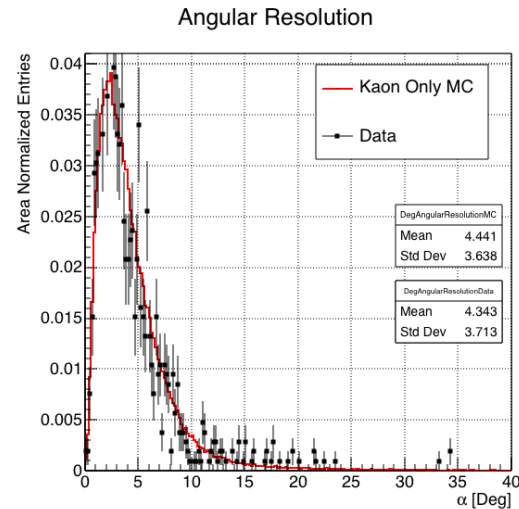


Figure 5.19: Distributions of angular resolution α for data used in the kaon cross section analysis and kaon only DDMC. The distributions are area normalized.

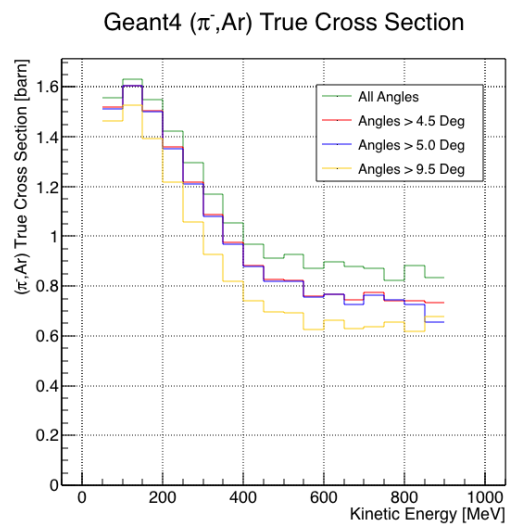


Figure 5.20: True (π^- , Ar) cross section for interaction angles greater than 0 deg (green), 4.5 deg (red), 5.0 deg (blue) and 9.0 deg (yellow).

2298 **5.6 Calorimetry Studies**

2299 The measured kinetic energy of a hadron candidate at each argon slab determines
2300 which bins of the interacting and incident histograms a selected event is going to fill.
2301 Thus, the energy measurement provided by the LArTPC is fundamental for the cross
2302 section analysis. In Appendix C, we describe how we calibrate the TPC calorimetric
2303 response. In the following section, we describe how we measure the kinetic energy of
2304 the hadrons in the TPC.

2305 **5.6.1 Kinetic Energy Measurement**

2306 In this section, we define the measurement on the kinetic energy and determine the
2307 related uncertainty. We will propagate this uncertainty into the cross section mea-
2308 surement, as discussed in Section 6.1.2 for the pion cross section and in Section ??
2309 for the kaon cross section.

2310 The kinetic energy of a hadron at the j^{th} slice of argon in the TPC is given by

$$KE_j = \sqrt{p_{\text{Beam}}^2 + m_{\text{Beam}}^2} - m_{\text{Beam}} - E_{\text{Loss}} - E_{\text{FF-j}}, \quad (5.6)$$

2311 where p_{Beam} is the momentum measured by the beamline detectors, m_{Beam} is the
2312 mass of the hadron as reported in the PDG, E_{Loss} is the energy loss between the
2313 beamline and the TPC, and $E_{\text{FF-j}}$ is the energy that the hadron deposited from the
2314 TPC front face until the j^{th} slice. The uncertainty on KE_j is then given by

$$\delta KE_j = \sqrt{\delta p_{\text{Beam}}^2 + \delta E_{\text{Loss}}^2 + \delta E_{\text{dep FF-j}}^2}, \quad (5.7)$$

2315 where we have dropped the uncertainty on the mass, since it is orders of magnitude
2316 smaller than the other uncertainties. We assume the relative uncertainty on p_{Beam} to
2317 be 2%, and the uncertainty on the energy loss upstream to be 7 MeV, as calculated

2318 in Section 5.4. We describe the estimate of the uncertainty on $E_{\text{FF-j}}$ in the rest of
2319 this section.

2320 The energy deposited by the hadron from the TPC front face until the j^{th} slice is
2321 the sum of the measured energy deposited in each previous slabs E_i , i.e.

$$E_{\text{FF-j}} = \sum_{i < j} E_i, \quad (5.8)$$

2322 where E_i is measured in each slab as the product of the stopping power, dE/dX_i ,
2323 and the track pitch, Pitch_i , for that point. If we assume conservatively that the
2324 measurements of E_i are not independent from one another, the uncertainty on $E_{\text{FF-j}}$
2325 becomes

$$\delta E_{\text{FF-j}} = (j - 1)\delta E_i, \quad (5.9)$$

2326 where δE_i is the uncertainty on the energy loss in one slab of argon.

2327 The left side of Figure 5.21 shows the distribution of the energy deposited in each
2328 slab of argon, for the 60A negative pion dataset in black and for the pion only MC
2329 in blue. The analogous plot for the -100A negative pion data set is show on the right
2330 side of Figure 5.21. The distributions are fitted with a landau displayed in red for
2331 data and in teal for MC. The uncertainty on E_i is given by the width of the Landau
2332 fit to the data. A small systematic uncertainty is given by a 1.0% difference between
2333 the most probable value of the landau fits in data and MC.

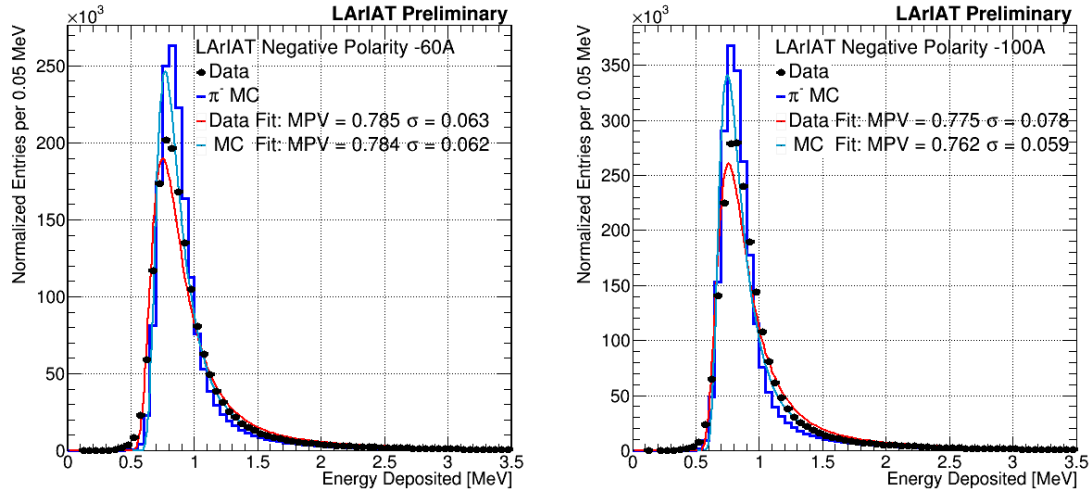


Figure 5.21: Energy deposited E_i in a single slab of argon for the pion -60A runs (left) and -100A runs (right). The data is shown in black, the MC in blue. The distributions are fitted with a landau displayed in red for data and in teal for MC.

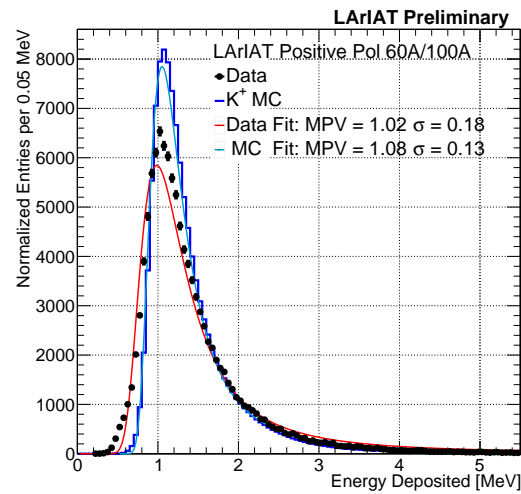


Figure 5.22: Energy deposited E_i in a single slab of argon for the kaons of the +60A runs and +100A runs. The data is shown in black, the MC in blue. The distributions are fitted with a landau displayed in red for data and in teal for MC.

2334 **Chapter 6**

2335 **Negative Pion Cross Section**

2336 **Measurement**

2337 “*Y ella es flama que se eleva, Y es un pájaro a volar.*
2338 *En la noche que se incendia, estrella de oscuridad*
2339 *que busca entre la tiniebla, la dulce hoguera del beso.*”
2340 – Lila Downs, 2002 –

2341 In this chapter, we show the result of the thin slice method to measure the (π^- -
2342 Ar) total hadronic cross section. In Section 6.1, we start by measuring the raw
2343 cross section, i.e. the cross section obtained exclusively using data reconstruction,
2344 without any additional corrections. In Section 6.2, we apply a statistical subtraction
2345 of the background contributions based on simulation and a correction for detection
2346 inefficiency. The final results are presented in Section 6.3.

2347 **6.1 Raw Cross Section**

2348 We measure the raw (π^- -Ar) total hadronic cross section as a function of the kinetic
2349 energy in the two chosen data sets, the -60A and -100A negative runs. As we will

clarify in Section 6.2, the corrections to the raw cross section depend on the beam conditions and need to be calculated independently for the two datasets. Thus, we present here the measurement of the raw cross section on the two datasets separately.

As stated in section 4.3.2, the raw cross section is given by the equation 4.4

$$\sigma_{TOT}(E_i) = \frac{1}{n\delta X} \frac{N_{Int}^{TOT}(E_i)}{N_{Inc}^{TOT}(E_i)}, \quad (6.1)$$

where N_{Int}^{TOT} is the measured number of particles interacting at kinetic energy E_i , N_{Inc}^{TOT} is the measured number of particles incident on an argon slice at kinetic energy E_i , n is the density of the target centers and δX is the thickness of the argon slice. The density of the target centers and the slab thickness are $n = 0.021 \cdot 10^{24} \text{ cm}^{-3}$ and $\delta X = 0.47 \text{ cm}$, respectively.

Figure 6.1 shows the distribution of N_{Int}^{TOT} as a function of the kinetic energy for the 60A dataset on the left and for the 100A dataset on the right. The data central points are represented by black dots, the statistical uncertainty is shown in black, while the systematic uncertainty is shown in red. Data is displayed over the N_{Int}^{TOT} distribution obtained with a MC mixed sample of pions, muon and electrons (additional details on the composition will be provided in Section ??). The contribution from the simulated pions is shown in blue, the one from secondaries in red, the one from muons in yellow and the ones from electrons in gray. The simulated pion's and backgrounds' contributions are stacked; the sum of the integrals from each particle species is normalized to the integral of the data.

Figure 6.2 shows the distribution of N_{Inc}^{TOT} for the 60A dataset on the left and for the 100A dataset on the right. Data is displayed over the MC. The same color scheme and normalization procedure is used for both the interacting and incident histograms.

Figure 6.3 shows the raw cross section for the 60A dataset on the left and for the 100A dataset on the right, statistical uncertainty in black and systematic uncertainty

2374 in red. The raw data cross section is overlaid to the reconstructed cross section for
 2375 the MC mixed sample, displayed in azure. Since the background contributions and
 2376 the detector effects for the 60A and 100A sample are different, it is premature to
 2377 compare the raw cross sections obtained from the two samples at this point.

2378 We describe the calculation of the statistical uncertainty for the interacting, in-
 2379 cident and cross section distributions in Section 6.1.1; we describe the procedure to
 2380 calculate the corresponding systematics uncertainty on Section 6.1.2.

2381 6.1.1 Statistical Uncertainty

2382 The statistical uncertainty for a given kinetic energy bin of the cross section is cal-
 2383 culated by error propagation from the statistical uncertainty on $N_{\text{Inc}}^{\text{TOT}}$ and $N_{\text{Int}}^{\text{TOT}}$
 2384 correspondent bin. Since the number of incident particles in each energy bin is given
 2385 by a simple counting, we assume that $N_{\text{Inc}}^{\text{TOT}}$ is distributed as a poissonian with mean
 2386 and variance equal to $N_{\text{Inc}}^{\text{TOT}}$ in each bin. On the other hand, $N_{\text{Int}}^{\text{TOT}}$ follows a bino-
 2387 mial distribution: a particle in a given energy bin might or might not interact. The
 2388 variance for the binomial is given by

$$\text{Var}[N_{\text{Int}}^{\text{TOT}}] = \mathcal{N}P_{\text{Interacting}}(1 - P_{\text{Interacting}}). \quad (6.2)$$

2389 Since the interaction probability $P_{\text{Interacting}}$ is $\frac{N_{\text{Int}}^{\text{TOT}}}{N_{\text{Inc}}^{\text{TOT}}}$ and the number of tries \mathcal{N} is
 2390 $N_{\text{Inc}}^{\text{TOT}}$, equation 6.2 translates into

$$\text{Var}[N_{\text{Int}}^{\text{TOT}}] = N_{\text{Inc}}^{\text{TOT}} \frac{N_{\text{Int}}^{\text{TOT}}}{N_{\text{Inc}}^{\text{TOT}}} \left(1 - \frac{N_{\text{Int}}^{\text{TOT}}}{N_{\text{Inc}}^{\text{TOT}}}\right) = N_{\text{Int}}^{\text{TOT}} \left(1 - \frac{N_{\text{Int}}^{\text{TOT}}}{N_{\text{Inc}}^{\text{TOT}}}\right). \quad (6.3)$$

2391 $N_{\text{Inc}}^{\text{TOT}}$ and $N_{\text{Int}}^{\text{TOT}}$ are not independent. The statistical uncertainty on the cross
 2392 section is thus calculated as

$$\delta\sigma_{\text{TOT}}(E) = \sigma_{\text{TOT}}(E) \left(\frac{\delta N_{\text{Int}}^{\text{TOT}}}{N_{\text{Int}}^{\text{TOT}}} + \frac{\delta N_{\text{Inc}}^{\text{TOT}}}{N_{\text{Inc}}^{\text{TOT}}} \right) \quad (6.4)$$

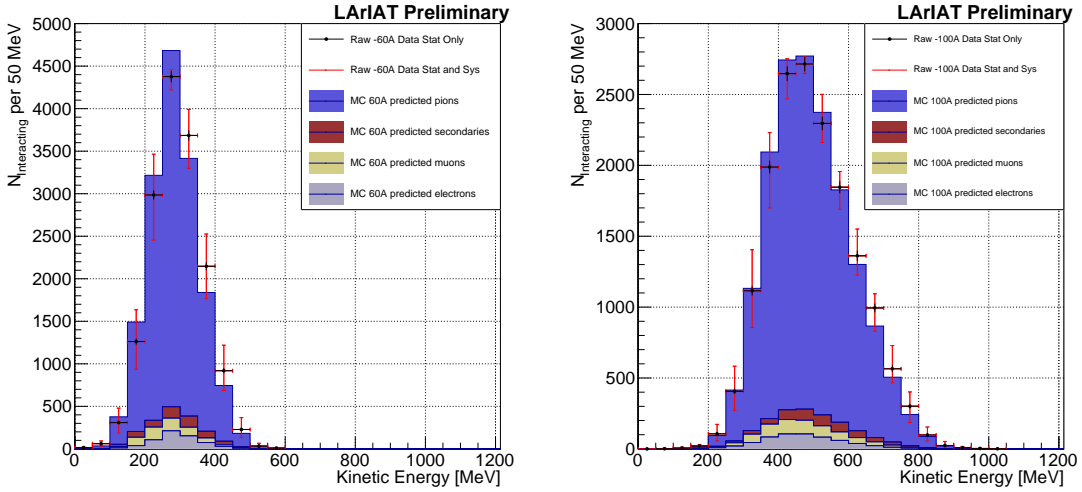


Figure 6.1: Raw number of interacting pion candidates as a function of the reconstructed kinetic energy for the 60A runs (left) and for the 100A runs (right). The statistical uncertainties are shown in black, the systematic uncertainties in red.

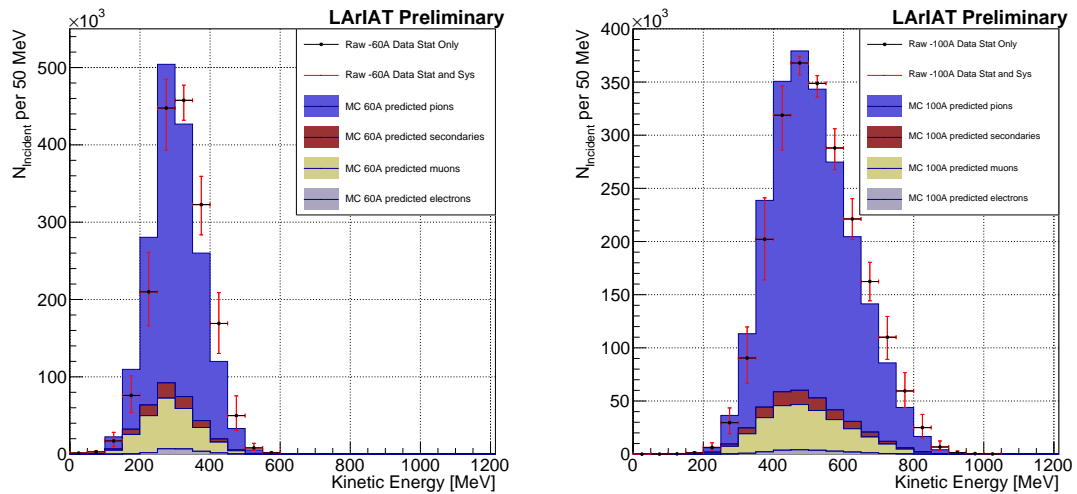


Figure 6.2: Raw number of incident pion candidates as a function of the reconstructed kinetic energy for the 60A runs (left) and for the 100A runs (right). The statistical uncertainty is shown in black, the systematic uncertainties in red.

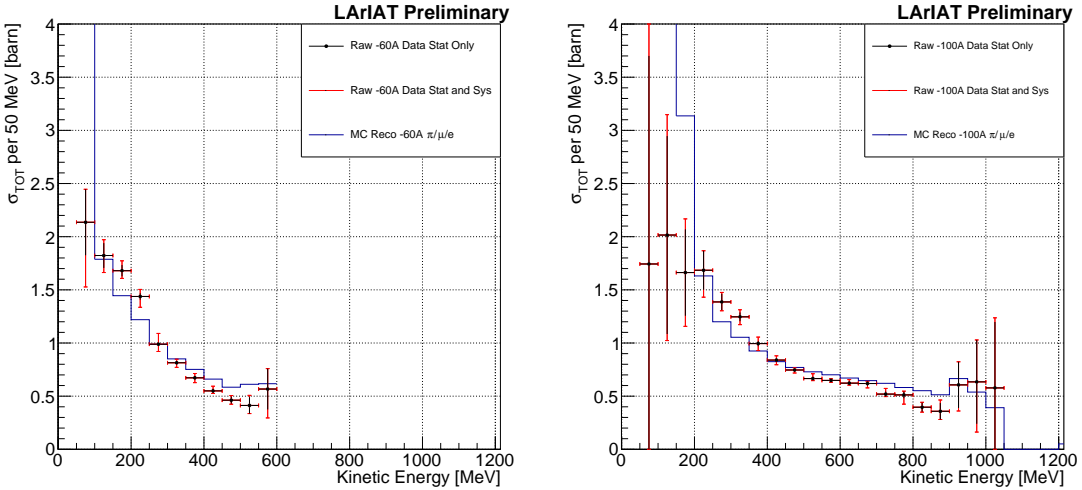


Figure 6.3: Raw (π^- -Ar) total hadronic cross section for the 60A runs (left) and for the 100A runs (right). The statistical uncertainty is shown in black, the systematic uncertainties in red. The raw cross section obtained with a MC mixed sample of pions, muon and electrons in the percentage predicted by G4Beamline is shown in azure.

2393 where:

$$\delta N_{\text{Inc}}^{\text{TOT}} = \sqrt{N_{\text{Inc}}^{\text{TOT}}} \quad (6.5)$$

$$\delta N_{\text{Int}}^{\text{TOT}} = \sqrt{N_{\text{Int}}^{\text{TOT}} \left(1 - \frac{N_{\text{Int}}^{\text{TOT}}}{N_{\text{Inc}}^{\text{TOT}}}\right)}. \quad (6.6)$$

2394 6.1.2 Treatment of Systematics

2395 The only systematic effect considered in the measurement of the raw cross section
 2396 results from the propagation of the uncertainty associate with the measurement of
 2397 the kinetic energy at each argon slab. As shown in Section 5.6.1, the uncertainty on
 2398 the kinetic energy of a pion candidate at the j^{th} slab of argon is given by

$$\delta KE_j = \sqrt{\delta p_{\text{Beam}}^2 + \delta E_{\text{Loss}}^2 + \delta E_{\text{dep FF-j}}^2} \quad (6.7)$$

$$= \sqrt{(2\% p_{\text{Beam}})^2 + (6 \text{ [MeV]})^2 + (j - 1)^2 (\sim 0.08 \text{ [MeV]})^2}. \quad (6.8)$$

2399 We propagate this uncertainty by varying the energy measurement KE_j at each
 2400 argon slab. We measure $N_{\text{Inc}}^{\text{TOT}}$, $N_{\text{Int}}^{\text{TOT}}$ and the cross section in three cases: first
 2401 assigning the measured KE_j at each kinetic energy sampling, then assigning $KE_j +$
 2402 δKE_j , and finally assigning $KE_j - \delta KE_j$. The difference between the values obtained
 2403 using the KE_j sampling and the maximum and minimum values in each kinetic energy
 2404 bin determines the systematic uncertainty.

2405 **6.2 Corrections to the Raw Cross Section**

2406 As described in section 4.3.3, we need to apply a background correction and an
 2407 efficiency correction in order to derive the true pion cross section from the raw cross
 2408 section. The true cross section is given in equation 4.9,

$$\sigma_{\text{TOT}}^{\pi^-}(E_i) = \frac{1}{n\delta X} \frac{\epsilon^{\text{Inc}}(E_i)}{\epsilon^{\text{Int}}(E_i)} \frac{C_{\text{Int}}^{\pi MC}(E_i)}{C_{\text{Inc}}^{\pi MC}(E_i)} \frac{N_{\text{Int}}^{\text{TOT}}(E_i)}{N_{\text{Inc}}^{\text{TOT}}(E_i)}. \quad (4.9)$$

2409 Section 6.2.1 describes the evaluation of pion content in the interacting and inci-
 2410 dent histograms, ($C_{\text{Int}}^{\pi MC}(E_i)$ and $C_{\text{Inc}}^{\pi MC}(E_i)$) and the propagation to the cross section
 2411 measurement of the relative systematic uncertainties.

2412 Section 6.2.2 describes the procedure employed to obtain the efficiency corrections
 2413 $\epsilon^{\text{Int}}(E_i)$ and $\epsilon^{\text{Inc}}(E_i)$ and the propagation to the cross section measurement of the
 2414 relative uncertainties.

2415 **6.2.1 Background subtraction**

2416 We use the procedure described in 5.3.2 to evaluate the relative pion content in
 2417 the interacting histogram $C_{\text{Int}}^{\pi MC}(E_i)$ and the relative pion content in the incident
 2418 $C_{\text{Inc}}^{\pi MC}(E_i)$. We start by evaluating the relative pion content assuming the beamline
 2419 composition simulated by G4Beamline, whose pion, muon and electron percentages
 2420 per beam condition are reported again in the first line of Table 6.1. The left side of

2421 Figure 6.4 shows the MC estimated relative pion content for the interacting histogram
2422 as function of kinetic energy for the 60A runs (top) and 100A runs (bottom). The
2423 right side of the same figure shows the MC estimated relative pion content for the
2424 incident histogram as function of kinetic energy for the 60A runs (top) and 100A
2425 runs (bottom). In Figure 6.4 the central curves displayed in light blue are obtained
2426 using the beamline composition as predicted by G4Beamline: these are the correction
2427 curves for the relative pion content applied to data.

2428 So, the question now becomes: how well do we know the beamline composition?
2429 In absence of additional data constraints, we take a 100% systematic uncertainty on
2430 the electron content, reported in lines 3 and 4 of Table 6.1. The effect of doubling or
2431 halving the electron percentage in the beam on the pion relative content is displayed
2432 in red in Figure 6.4. We reserve a slightly different treatment for the muon content.
2433 Since G4Beamline tracks only particles which cross all the wire chambers, pion events
2434 that decay in flight from WC1 to WC4 are not recorded by G4Beamline. Pion decays
2435 in the beamline could be trigger the beamline detectors in data, if the produced muon
2436 proceeds in the beamline. Thus, we take the G4Beamline prediction for muons as a
2437 lower bound in the composition: the effect of doubling the muon content (line 2 in
2438 Table 6.1) is shown in blue on Figure 6.4. A future study of data from additional
2439 beamline detectors such as the Aerogel Chernkov detectors [43] or the muon range
2440 stack (see Section 3.2.4) has the potential of a narrowing the systematics uncertainty
2441 coming from the beamline composition.

2442 We propagate the uncertainty on the beamline composition as a systematic un-
2443 certainty to the cross section by varying the beam composition for all the cases listed
2444 in Table 6.1 and evaluating variation of obtained data cross sections in each bin. This
2445 systematic uncertainty is summed in quadrature with the statistical uncertainty and
2446 the systematic uncertainty related to the kinetic energy measurement.

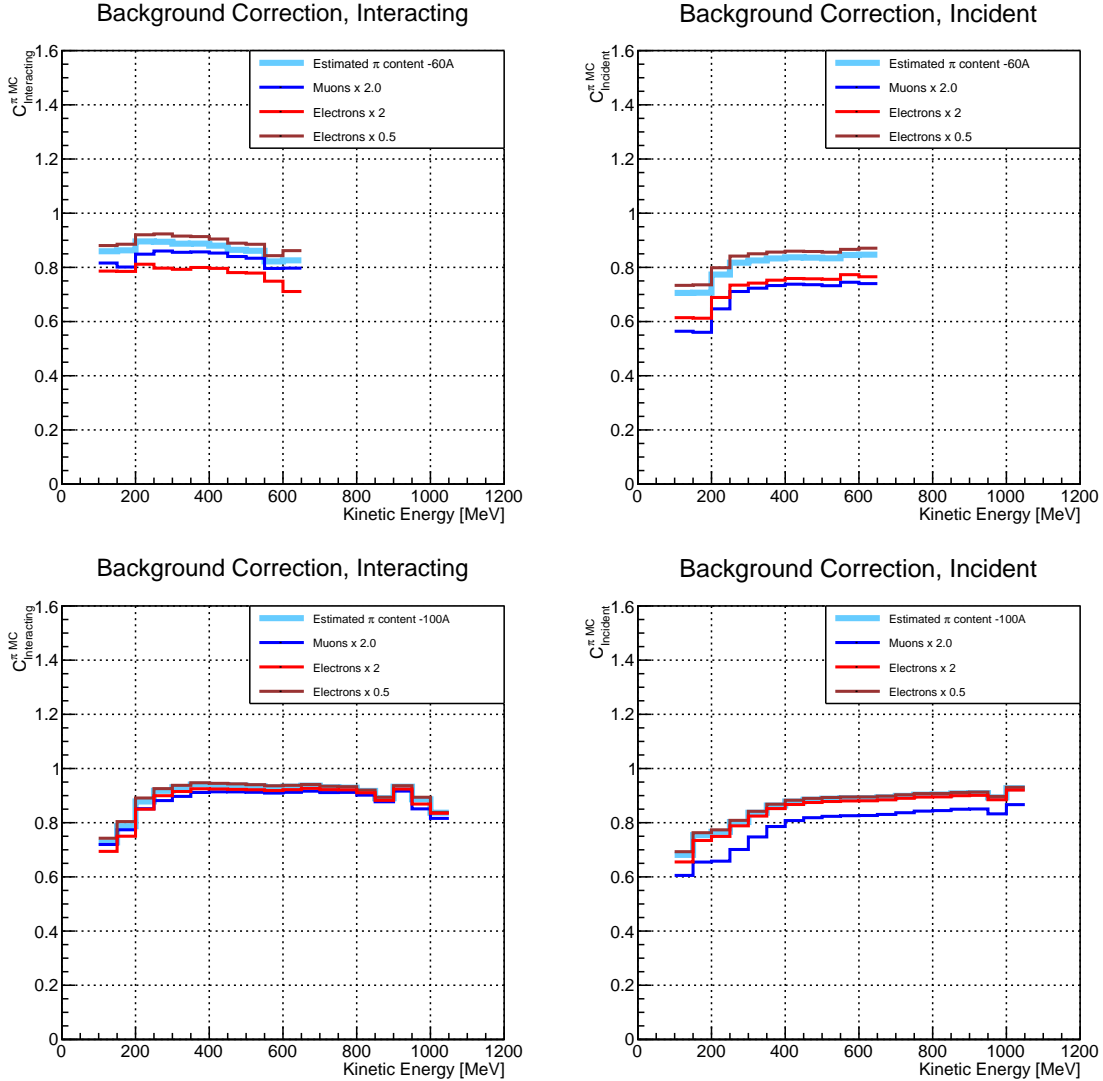


Figure 6.4: *Left:* MC estimated relative pion content for interacting histogram a function of kinetic energy for the 60A runs (top) and 100A runs (bottom), predicted background content in azure and muon and electron content variation in blue and red. *Right:* MC estimated relative pion content for incident histogram a function of kinetic energy for the 60A runs (top) and 100A (bottom), predicted background content in azure and muon and electron content variation in blue and red

2447 6.2.2 Efficiency Correction

2448 The interaction point for a track used in the total hadronic cross section analysis
2449 is defined to be the last point of the WC2TPC matched track which lies inside the
2450 fiducial volume. This definition is independent from the topology of the interaction.
2451 If the TPC track stops within the fiducial volume, its last point will be the interaction
2452 point, no matter what the products of the interaction look like; if the track crosses the
2453 boundaries of the fiducial volume, the track will be considered “through going” and no
2454 interaction point will be found. Given this definition, it is evident that we rely on the
2455 tracking algorithm to discern where the interaction occurred in the TPC and correctly
2456 stop the tracking. The tracking algorithm has an intrinsic angle resolution as shown
2457 in section 5.5.1, which limits its efficiency, especially in the case of elastic scattering
2458 occurring at low angles. Thus, we need to apply an efficiency correction to data in order
2459 to retrieve the true cross section. The efficiency correction is evaluated separately for
2460 the interacting and incident histograms, namely ϵ_i^{int} and ϵ_i^{inc} , and propagated to the
2461 cross section as shown in equation 4.9.

2462 Efficiency Correction: Procedure

2463 We describe here the procedure to calculate the efficiency correction taking the in-
2464 teracting histogram as example and noting that the procedure is identical for the
2465 incident histogram.

2466 We derive the correction on a set of pure pion MC, calculating its value bin by
2467 bin as the ratio between the true bin content and the correspondent reconstructed
2468 bin content. The correction is then applied to the relevant bin in data. In formulae,
2469 the efficiency correction is calculated to be

$$\epsilon^{\text{Int}}(E_i) = \frac{N_{\text{Interacting}}^{\pi \text{ Reco MC}}(E_i)}{N_{\text{Interacting}}^{\pi \text{ True MC}}(E_i)}, \quad (6.9)$$

2470 where $N_{\text{Int}}^{\pi \text{ True MC}}(E_i)$ is the content of the i -th bin in for the true interacting
 2471 histogram, and $N_{\text{Int}}^{\pi \text{ Reco MC}}(E_i)$ is the content of the i -th bin in for the reconstructed
 2472 interacting histogram. The correction is applied to data as follows

$$N_{\text{Int}}^{\pi \text{ True Data}}(E_i) = \frac{N_{\text{Int}}^{\pi \text{ Reco Data}}(E_i)}{\epsilon^{\text{Int}}(E_i)} = N_{\text{Int}}^{\pi \text{ Reco Data}}(E_i) \frac{N_{\text{Int}}^{\pi \text{ True MC}}(E_i)}{N_{\text{Int}}^{\pi \text{ Reco MC}}(E_i)}. \quad (6.10)$$

2473 where $N_{\text{Int}}^{\pi \text{ Reco Data}}(E_i)$ is the background subtracted bin content of the i -th bin in
 2474 for the reconstructed interacting histogram for data, i.e.

$$N_{\text{Int}}^{\pi \text{ Reco Data}}(E_i) = N_{\text{Int}}^{\text{TOT Data}}(E_i) - B_{\text{Int}}^{\text{Data}}(E_i) = C_{\text{Int}}^{\pi \text{ MC}}(E_i) N_{\text{Int}}^{\text{TOT Data}}(E_i). \quad (6.11)$$

2475 In section 5.5.1, we estimated the angular resolution for data and MC to be
 2476 $\bar{\alpha}_{\text{Data}} = (5.0 \pm 4.5)$ deg and $\bar{\alpha}_{\text{MC}} = (4.5 \pm 3.9)$ deg, respectively. Most interaction
 2477 angles smaller than the angular resolution will thus be indistinguishable for the re-
 2478 construction. Thus, we claim we are able to measure the cross section for interaction
 2479 angles greater than 5.0 deg. Geant4 simulates interactions at all angles, as shown in
 2480 figure 6.7. In order to calculate the efficiency correction, we select events which have
 2481 an interaction angle greater than a given α_{res} to construct the true interacting and
 2482 incident histograms (the denominator of the efficiency correction). The systematics
 2483 on the efficiency correction is estimated by varying the value of α_{res} between 0 deg
 2484 and 4.5 deg and propagating the uncertainty on the cross section.

2485 Figure 6.5 shows $\epsilon^{\text{Int}}(E_i)$ in the left side and $\epsilon^{\text{Inc}}(E_i)$ on the right as a function of
 2486 the kinetic energy for the 60A runs and their systematic uncertainty. Similarly, figure
 2487 6.6 shows $\epsilon^{\text{Int}}(E_i)$ in the left side and $\epsilon^{\text{Inc}}(E_i)$ on the right as a function of the kinetic
 2488 energy for the 100A runs and their systematic uncertainty.

	Magnet Current -60A			Magnet Current -100 A		
	MC π^-	MC μ^-	MC e^-	MC π^-	MC μ^-	MC e^-
Expected Composition	68.8 %	4.6 %	26.6 %	87.4 %	3.7 %	8.9 %
Composition 2x Muons	64.2 %	9.2 %	26.6 %	83.7 %	7.4 %	8.9 %
Composition 2x Electrons	42.2 %	4.6 %	53.2 %	78.5 %	3.7 %	17.8 %
Composition 0.5x Electrons	82.1 %	4.6 %	13.3 %	91.9 %	3.7 %	4.4 %

Table 6.1: Beam composition variation for the study of systematics due to beam contamination.

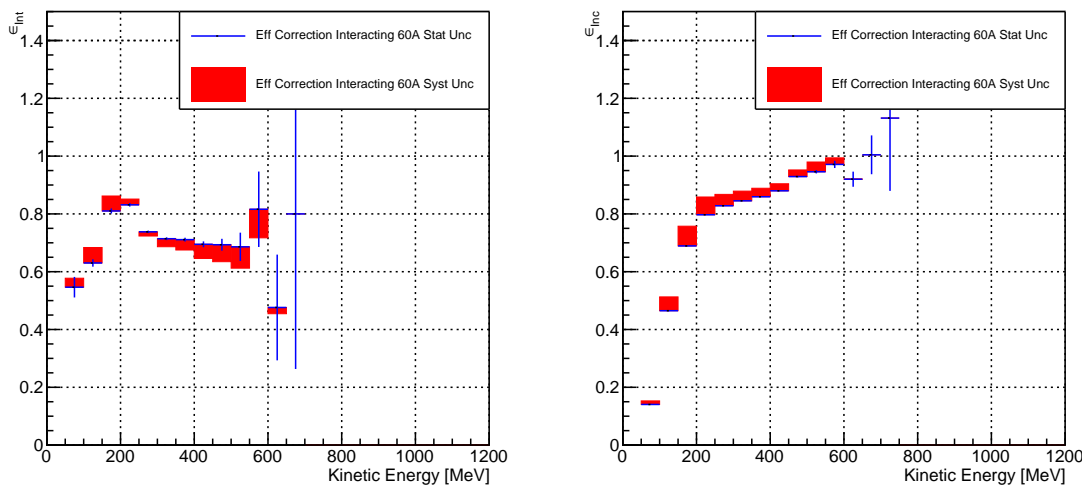


Figure 6.5: *Left:* Efficiency correction on the 60A interacting histogram, statistical uncertainty in blue, systematic uncertainty in red. *Right:* Efficiency correction on the 60A incident histogram, statistical uncertainty in blue, systematic uncertainty in red.

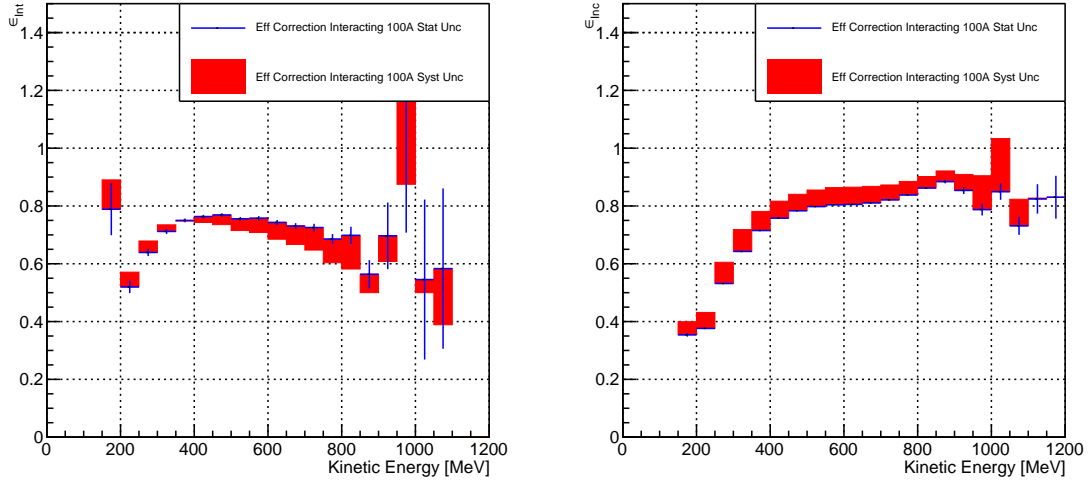


Figure 6.6: *Left*: Efficiency correction on the 100A interacting histogram, statistical uncertainty in blue, systematic uncertainty in red. *Right*: Efficiency correction on the 100A incident histogram, statistical uncertainty in blue, systematic uncertainty in red.

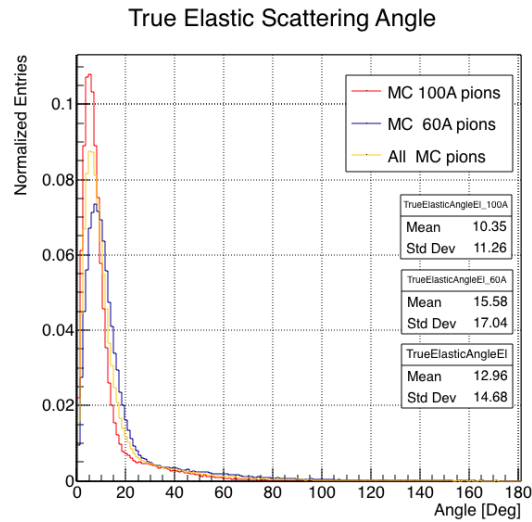


Figure 6.7: Distribution of the true scattering angle for a pion elastic scattering off the argon nucleus as simulated by Geant4.

2489 **6.3 Results**

2490 Figure 6.8 show the measurement of the (π^- -Ar) total hadronic cross section for
2491 scattering angles greater than 5° , as the result of the background subtraction and
2492 efficiency correction to the raw cross section. The top left plot is the measurement
2493 obtained on the 60A data, statistical uncertainty in black and systematic uncertainty
2494 in red. The top right plot is the measurement obtained on the 100A data, statistical
2495 uncertainty in black and systematic uncertainty in blue. The bottom plot shows the
2496 two measurements overlaid. In all three plot, the Geant4 prediction for the total
2497 hadronic cross section for angle scattering greater than 5° is displayed in green.

2498 The systematic uncertainty on the cross section is the sum in quadrature of the
2499 statistical uncertainty, the systematic uncertainty related to the kinetic energy mea-
2500 surement, the systematic uncertainty related to the beam composition and the sys-
2501 tematic uncertainty related to the efficiency correction.

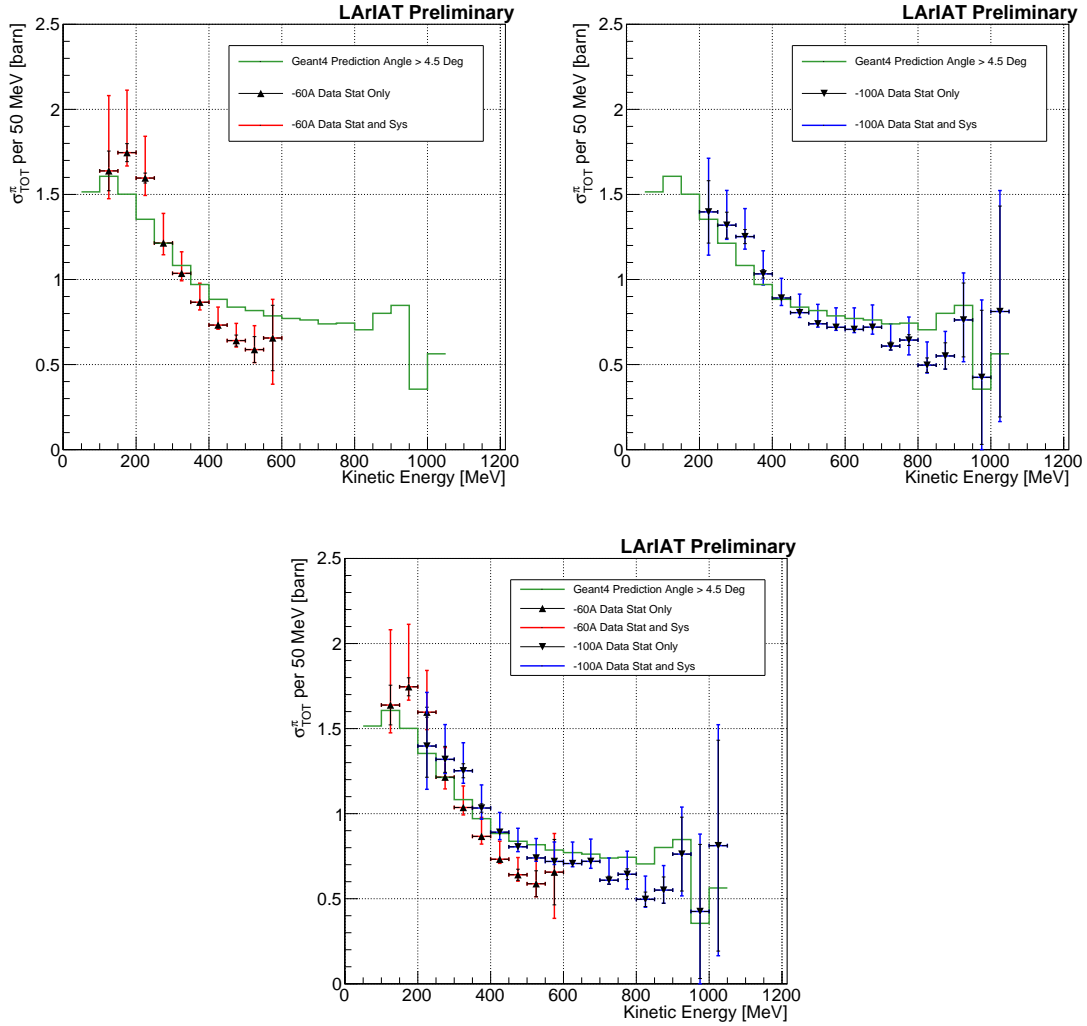


Figure 6.8: *Top Left:* (π^- -Ar) total hadronic cross section for scattering angles greater than 5° measured in the 60A sample, statistical uncertainty in black and systematic uncertainty in red. The Geant4 prediction for the total hadronic cross section for angle scattering greater than 5° is displayed in green.

Top Right: (π^- -Ar) total hadronic cross section for scattering angles greater than 5° measured in the 100A sample, statistical uncertainty in black and systematic uncertainty in blue. The Geant4 prediction for the total hadronic cross section for angle scattering greater than 5° is displayed in green.

Bottom: (π^- -Ar) total hadronic cross section measurements in the 60A and 100A samples overlaid with the Geant4 prediction (green).

2502 **Chapter 7**

2503 **Positive Kaon Cross Section**

2504 **Measurement**

2505 “Beat-up little seagull, on a marble stair
2506 Tryin’ to find the ocean, lookin’ everywhere.”
2507 – Nina Simone, 1978 –

2508 In this chapter, we show the result of the thin slice method to measure the (K^+ -
2509 Ar) total hadronic cross section. In Section 7.1, we start by measuring the raw
2510 cross section. In Section 7.2, we apply a statistical subtraction of the background
2511 contributions based on simulation and a correction for detection inefficiency. The
2512 final results are presented in Section 7.3.

2513 **7.1 Raw Cross Section**

2514 We measure the raw (K^+ -Ar) total hadronic cross section as a function of the kinetic
2515 energy in the combined +60A and +100A dataset.

2516 Similar to the pion case, the raw cross section is given by the equation 4.4

$$\sigma_{TOT}(E_i) = \frac{1}{n\delta X} \frac{N_{Int}^{TOT}(E_i)}{N_{Inc}^{TOT}(E_i)}, \quad (7.1)$$

2517 where N_{Int}^{TOT} is the measured number of particles interacting at kinetic energy E_i ,
2518 N_{Inc}^{TOT} is the measured number of particles incident on an argon slice at kinetic energy
2519 E_i , n is the density of the target centers and δX is the thickness of the argon slice.
2520 The density of the target centers and the slab thickness are $n = 0.021 \cdot 10^{24} \text{ cm}^{-3}$ and
2521 $\delta X = 0.47 \text{ cm}$, respectively.

2522 As in the case of pions, kaons might decay or interact between WC4 and the TPC
2523 front face. Some of the interaction products may be wrongly matched to the WC
2524 track, forming the “secondary” particle’s background in the kaon sample. We estimate
2525 the effect of the contamination of secondaries through the DDMC kaon sample. Figure
2526 7.1 shows the distribution of N_{Int}^{TOT} as a function of the kinetic energy. The data
2527 central points are represented by black dots, the statistical uncertainty is shown in
2528 black, while the systematic uncertainty is shown in red. Data is displayed over the
2529 N_{Int}^{TOT} distribution obtained with a DDMC sample of kaons shot from WC4. The
2530 contribution from the simulated kaons which interact hadronically is shown in pink,
2531 the contributions from kaon decay is shown in orange and the one from secondaries
2532 in red. The simulated kaon’s and secondaries’ contributions are stacked; the sum of
2533 their integrals is normalized to the integral of the data.

2534 Figure 7.2 shows the distribution of N_{Inc}^{TOT} . Data is displayed over the MC. For the
2535 N_{Inc}^{TOT} distribution we do not make a distinction between kaons that decay or interact
2536 hadronically because any kaon independently from its final interaction contributes
2537 to the flux of incident particles at given kinetic energy. The same normalization
2538 procedure is used for both the interacting and incident histograms.

2539 Figure 7.3 shows the raw cross section, statistical uncertainty in black and system-

atic uncertainty in red. The raw data cross section is overlaid to the reconstructed cross section for the MC mixed sample, displayed in azure. We calculate the statistical uncertainty for the interacting, incident and cross section distributions in a similar fashion to the pion case as described in Section 6.1.1.

As in the pion case, the only systematic effect considered in the measurement of the raw cross section results from the propagation of the uncertainty associate with the measurement of the kinetic energy at each argon slab. For kaons, the uncertainty on the kinetic energy of a candidate at the j^{th} slab of argon is given by

$$\delta KE_j = \sqrt{\delta p_{Beam}^2 + \delta E_{Loss}^2 + \delta E_{dep\ FF-j}^2} \quad (7.2)$$

$$= \sqrt{(2\% p_{Beam})^2 + (7\text{ [MeV]})^2 + (j - 1)^2(\sim 0.18\text{ [MeV]})^2}. \quad (7.3)$$

We propagate this uncertainty by varying the energy measurement KE_j at each argon slab. We measure N_{Inc}^{TOT} , N_{Int}^{TOT} and the cross section in three cases: first assigning the measured KE_j at each kinetic energy sampling, then assigning $KE_j + \delta KE_j$, and finally assigning $KE_j - \delta KE_j$. The difference between the values obtained using the KE_j sampling and the maximum and minimum values in each kinetic energy bin determines the systematic uncertainty.

7.2 Corrections to the Raw Cross Section

As described in section 4.3.3, we need to apply a background correction and an efficiency correction in order to derive the true Kaon cross section from the raw cross section. The true cross section is given in equation 4.9,

$$\sigma_{TOT}^{K^+}(E_i) = \frac{1}{n\delta X} \frac{\epsilon^{Inc}(E_i)}{\epsilon^{Int}(E_i)} \frac{C_{Int}^{KMC}(E_i)}{C_{Inc}^{KMC}(E_i)} \frac{N_{Int}^{TOT}(E_i)}{N_{Inc}^{TOT}(E_i)}. \quad (4.9)$$

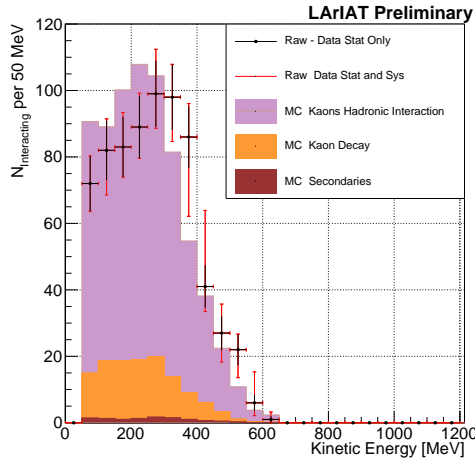


Figure 7.1: Raw number of interacting kaon candidates as a function of the reconstructed kinetic energy. The statistical uncertainties are shown in black, the systematic uncertainties in red.

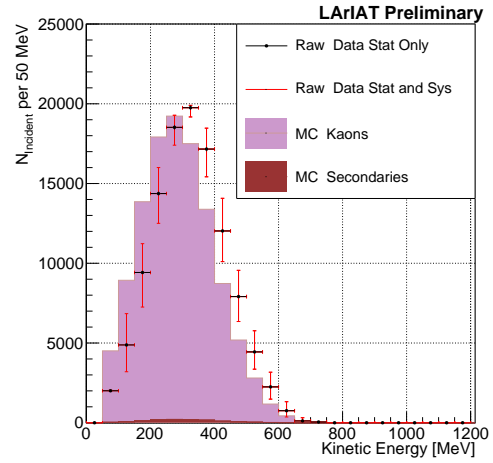


Figure 7.2: Raw number of incident kaon candidates as a function of the reconstructed kinetic energy. The statistical uncertainty is shown in black, the systematic uncertainties in red.

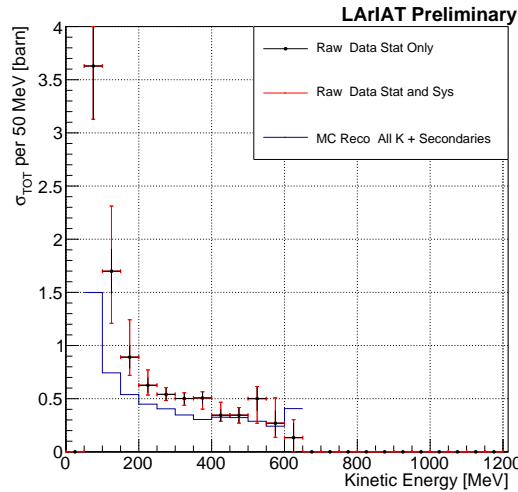


Figure 7.3: Raw (K^+ -Ar) total hadronic cross section. The statistical uncertainty is shown in black, the systematic uncertainties in red. The raw cross section obtained with a MC sample of kaons is shown in blue. For the MC cross section, we include the contributions from secondaries.

2558 Currently, the only background considered for the kaon hadronic cross section
2559 comes from the presence of secondaries. A further development of the analysis will
2560 need to account for the presence of a small proton contamination. Figure 7.4 shows
2561 the relative kaon content for the interacting and incident histograms.

2562 As described in 6.2.2 for the pion case, we derive the correction on a set of pure
2563 kaon MC, calculating its value bin by bin as the ratio between the true bin content
2564 and the correspondent reconstructed bin content. The correction is then applied to
2565 the relevant bin in data. The efficiency correction is evaluated separately for the
2566 interacting and incident histograms, namely ϵ_i^{int} and ϵ_i^{inc} , and propagated to the cross
2567 section as shown in equation 4.9.

2568 In section 5.5.1, we estimated the angular resolution for data and MC to be
2569 $\bar{\alpha}_{\text{Data}} = (4.3 \pm 3.7)$ deg and $\bar{\alpha}_{\text{MC}} = (4.4 \pm 3.6)$ deg, respectively. Most interaction
2570 angles smaller than the angular resolution will thus be indistinguishable for the re-
2571 construction. Thus, we claim we are able to measure the cross section for interaction
2572 angles greater than 4.5 deg. Geant4 simulates interactions at all angles: in order to
2573 calculate the efficiency correction, we select events which have an interaction angle
2574 greater than a α_{res} to construct the true interacting and incident histograms (the de-
2575 nominator of the efficiency correction). The systematics on the efficiency correction
2576 is estimated by varying the value of α_{res} between 0 deg and 4.5 deg and propagating
2577 the uncertainty on the cross section.

2578 Figure 7.5 shows $\epsilon^{\text{Int}}(E_i)$ in the left side and $\epsilon^{\text{Inc}}(E_i)$ on the right as a function of
2579 the kinetic energy for the kaon sample and their systematic uncertainty.

2580 7.3 Results

2581 Figure 7.6 show the measurement of the (K^+ -Ar) total hadronic cross section for
2582 scattering angles greater than 5° , as the result of the background subtraction and

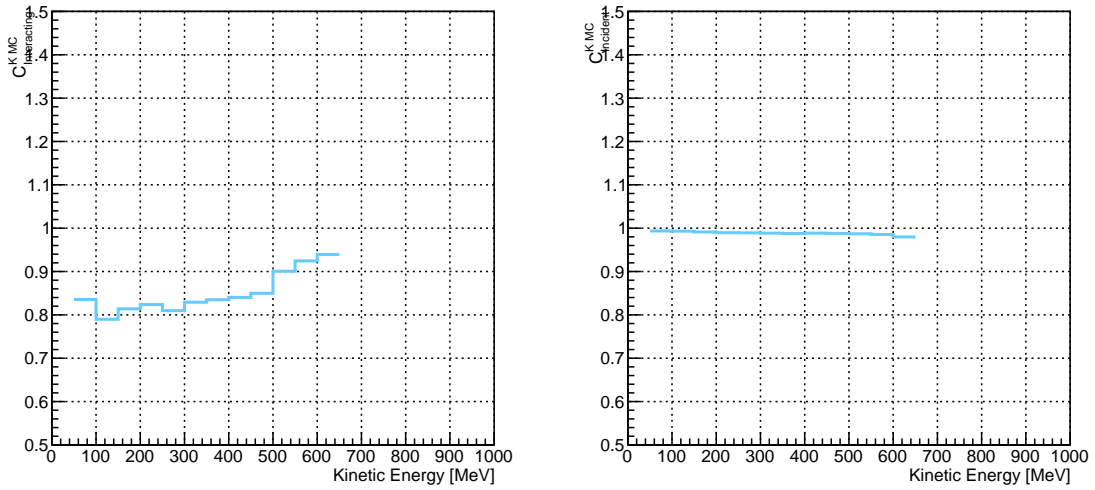


Figure 7.4: *Left:* MC estimated relative kaon content for kaons interacting hadronically as function of kinetic energy. *Right:* MC estimated relative kaon content for incident histogram a function of kinetic energy.

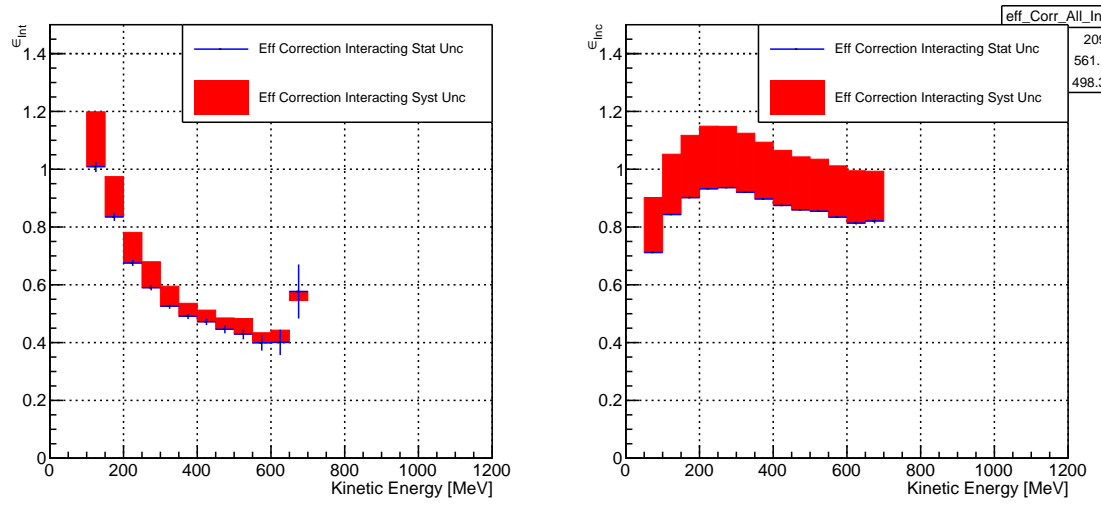


Figure 7.5: *Left:* Efficiency correction on the interacting histogram, statistical uncertainty in blue, systematic uncertainty in red. *Right:* Efficiency correction on the incident histogram, statistical uncertainty in blue, systematic uncertainty in red.

2583 efficiency correction to the raw cross section. The plot shows the measurement ob-
 2584 tained on the full dataset, statistical uncertainty in black and systematic uncertainty
 2585 in red. The Geant4 prediction for the total hadronic cross section for angle scattering
 2586 greater than 5° is displayed in green.

2587 The systematic uncertainty on the cross section is the sum in quadrature of the
 2588 statistical uncertainty, the systematic uncertainty related to the kinetic energy mea-
 2589 surement and the systematic uncertainty related to the efficiency correction.

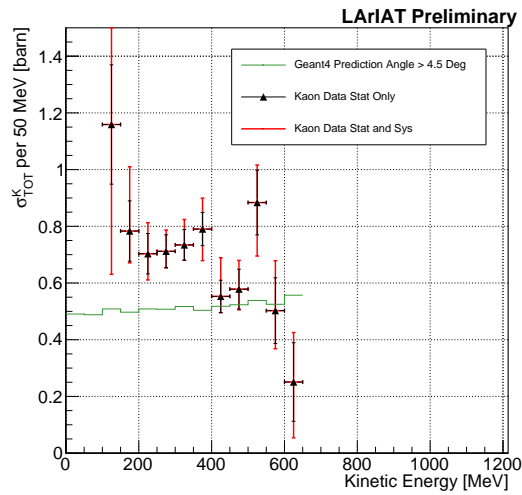


Figure 7.6: (K^+ -Ar) total hadronic cross section for scattering angles greater than 5° measured in the 60A sample, statistical uncertainty in black and systematic uncertainty in red. The Geant4 prediction for the total hadronic cross section for angle scattering greater than 5° is displayed in green.

2590

Chapter 8

2591

Conclusions

2592 In the era of neutrino precision measurements, of huge liquid argon detectors and
2593 of massive amount of information from LArTPCs, a renewed interest for an ancient
2594 measurement arises: the measurement of hadronic interactions with matter. With
2595 this work, we presented the first ever (π^- -Ar) and (K^+ -Ar) total hadronic cross
2596 section measurements as a function of the hadron kinetic energy. These analyses are
2597 the first physics analyses developed by the LArIAT experiment. Both the analysis
2598 follow a similar workflow and they rely on beam line detector information as well as
2599 both calorimetry and tracking in the TPC.

2600 In order to measure (π^- -Ar) total hadronic argon cross sections, we start by
2601 selecting pion beamline candidates through a series of selections on the beamline
2602 and TPC information apt to maximize the number of pions in the selection over
2603 the number of muons and electrons. We use the LArIAT beamline MC to estimate
2604 the beam composition of the selected beamline candidates and we propagate them
2605 to the LArIAT TPC constructing a properly weighted sample with the DDMC. We
2606 apply the thin slice method on the pion candidates and obtain the raw cross section
2607 measurement. From the simulated sample, we obtain two corrections accounting for
2608 the beamline background contamination and for detector effects. Finally, we apply

2609 the corrections to data and measure the true cross section.

2610 In order to measure (K^+ -Ar) total hadronic argon cross sections, we follow a
2611 similar procedure, i.e. we apply the thin slice method on kaon candidates identified
2612 in the beamline to obtain the raw cross section. We apply a background correction and
2613 a correction for detector effects to the raw cross section. The background correction
2614 accounts for the presence of secondary particles in both the interacting and incident
2615 histograms and for the presence of decay events in the interacting plot.

2616 The final results for the (π^- -Ar) and (K^+ -Ar) total hadronic cross section are
2617 shown side by side in figure 8.1.

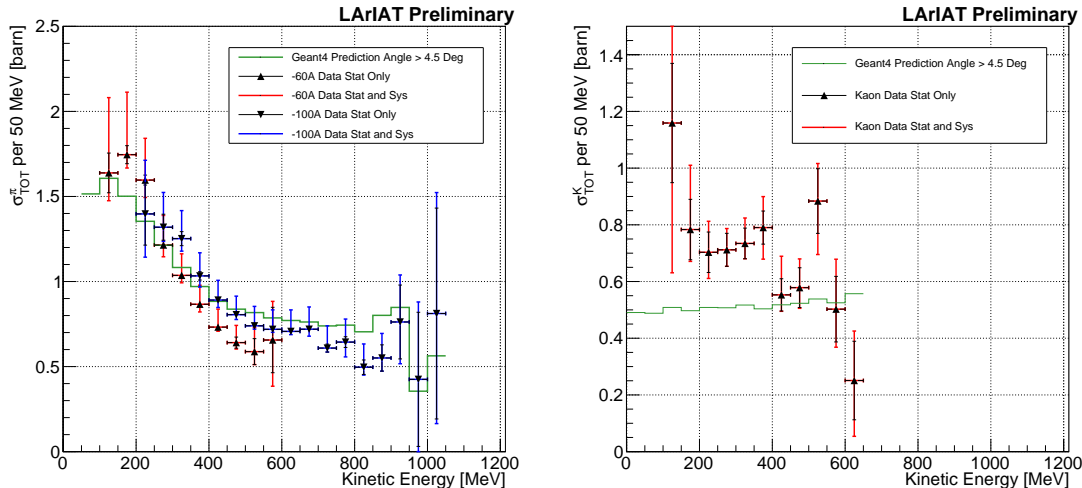


Figure 8.1: *Left:* (π^- -Ar) total hadronic cross section measurements in the 60A and 100A samples overlaid with the Geant4 prediction (green). *Right:* (K^+ -Ar) total hadronic cross section for scattering angles greater than 5° measured in the 60A sample, statistical uncertainty in black and systematic uncertainty in red. The Geant4 prediction for the total hadronic cross section for angle scattering greater than 5° is displayed in green.

2618 These analyses' will serve as a basis for the future cross section measurements of
2619 pions and kaons for the exclusive channels in LArIAT.

2620 **Appendix A**

2621 **Measurement of LArIAT Electric
2622 Field**

2623 The electric field of a LArTPC in the drift volume is a fundamental quantity for
2624 the proper functionality of this technology, as it affects almost every reconstructed
2625 quantity such as the position of hits or their collected charge. Given its importance,
2626 we calculate the electric field for LArIAT with a single line diagram from our HV
2627 circuit and we cross check the obtained value with a measurement relying only on
2628 TPC data.

2629 Before getting into the details of the measurement procedures, it is important to
2630 explicit the relationship between some quantities in play. The electric field and the
2631 drift velocity (v_{drift}) are related as follows

$$v_{drift} = \mu(E_{field}, T)E_{field}, \quad (\text{A.1})$$

2632 where μ is the electron mobility, which depends on the electric field and on the
2633 temperature (T). The empirical formula for this dependency is described in [115]
2634 and shown in Figure A.1 for several argon temperatures.

2635 The relationship between the drift time (t_{drift}) and the drift velocity is trivially

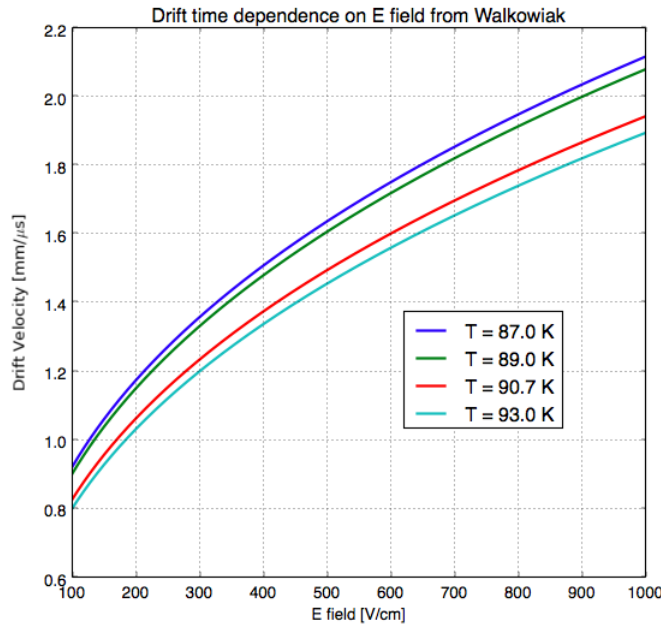


Figure A.1: Drift velocity dependence on electric field for several temperatures. The slope of the line at any one point represents the electron mobility for that given temperature and electric field.

Table A.1: Electric field and drift velocities in LArIAT smaller drift volumes

	Shield-Induction	Induction-Collection
E_{field}	700.63 V/cm	892.5 V/cm
v_{drift}	1.73 mm/μs	1.90 mm/μs
t_{drift}	2.31 μs	2.11 μs

2636 given by

$$t_{drift} = \Delta x / v_{drift}, \quad (\text{A.2})$$

2637 where Δx is the distance between the edges of the drift region. Table A.1 reports the
2638 values of the electric field, drift velocity, and drift times for the smaller drift volumes.

2639 With these basic parameters established, we can now move on to calculating the
2640 electric field in the main drift region (between the cathode and the shield plane).

2641 Single line diagram method

2642 The electric field strength in the LArIAT main drift volume can be determined know-
 2643 ing the voltage applied to the cathode, the voltage applied at the shield plane, and the
 2644 distance between them. We assume the distance between the cathode and the shield
 2645 plane to be 470 mm and any length contraction due to the liquid argon is negligibly
 2646 small (~ 2 mm).

2647 The voltage applied to the cathode can be calculated using Ohm's law and the
 2648 single line diagram shown in Figure A.2. A set of two of filter pots for emergency
 2649 power dissipation are positioned between the Glassman power supply and the cathode,
 2650 one at each end of the feeder cable, each with an internal resistance of $40 \text{ M}\Omega$.

2651 Given the TPC resistor chain, the total TPC impedance is $6 \text{ G}\Omega$. Since the total
 2652 resistance on the circuit is driven by the TPC impedance, we expect the resulting
 2653 current to be

$$I = V_{PS}/R_{tot} = -23.5 \text{ kV}/6 \text{ G}\Omega \sim 4 \mu\text{A}, \quad (\text{A.3})$$

2654 which we measure with the Glassman power supply, shown in Figure A.3.

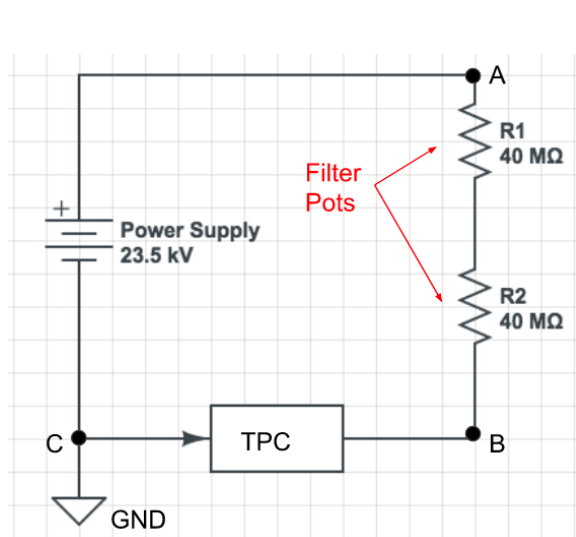


Figure A.2: LArIAT HV simple schematics.

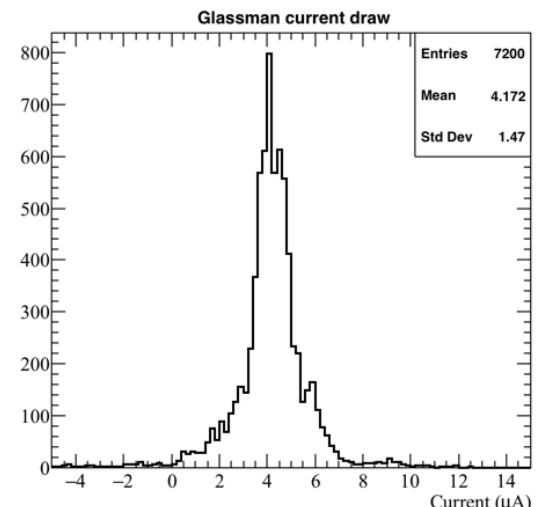


Figure A.3: Current reading from the Glassman between May 25th and May 30th, 2016 (typical Run-II conditions).

2655 Using this current, the voltage at the cathode is calculated as

$$V_{BC} = V_{PS} - (I \times R_{eq}) = -23.5 \text{ kV} + (0.00417 \text{ mA} \times 80 \text{ M}\Omega) = -23.17 \text{ kV}, \quad (\text{A.4})$$

2656 where I is the current and R_{eq} is the equivalent resistor representing the two filter
2657 pots. The electric field is then calculated to be

$$E_{\text{field}} = \frac{V_{BC} - V_{\text{shield}}}{\Delta x} = 486.54 \text{ V/cm}. \quad (\text{A.5})$$

2658 **E field using cathode-anode piercing tracks**

2659 We devise an independent method to measure the drift time (and consequently drift
2660 velocity and electric field) using TPC cathode to anode piercing tracks. We use this
2661 method as a cross check to the single line method. The basic idea is simple:

- 2662 0. Select cosmic ray events with only 1 reconstructed track
- 2663 1. Reduce the events to the one containing tracks that cross both anode and cath-
- 2664 ode
- 2665 2. Identify the first and last hit of the track
- 2666 3. Measure the time difference between these two hits (Δt).

2667 This method works under the assumptions that the time it takes for a cosmic particle
2668 to cross the chamber ($\sim \text{ns}$) is small compared to the charge drift time ($\sim \text{hundreds}$
2669 of μs).

2670 We choose cosmic events to allow for a high number of anode to cathode piercing
2671 tracks (ACP tracks), rejecting beam events where the particles travel almost perpen-
2672 dicularly to drift direction. We select events with only one reconstructed track to
2673 maximize the chance of selecting a single crossing muon (no-michel electron). We
2674 utilize ACP tracks because their hits span the full drift length of the TPC, see figure

2675 A.4, allowing us to define where the first and last hit of the tracks are located in space
2676 regardless of our assumption of the electric field.

2677 One of the main features of this method is that it doesn't rely on the measurement
2678 of the trigger time. Since Δt is the time difference between the first and last hit of a
2679 track and we assume the charge started drifting at the same time for both hits, the
2680 measurement of the absolute beginning of drift time t_0 is unnecessary. We boost the
2681 presence of ACP tracks in the cosmic sample by imposing the following requirements
2682 on tracks:

- 2683 • vertical position (Y) of first and last hits within ± 18 cm from TPC center
2684 (avoid Top-Bottom tracks)
- 2685 • horizontal position (Z) of first and last hits within 2 and 86 cm from TPC front
2686 face (avoid through going tracks)
- 2687 • track length greater than 48 cm (more likely to be crossing)
- 2688 • angle from the drift direction (phi in figure A.5) smaller than 50 deg (more
2689 reliable tracking)
- 2690 • angle from the beam direction (theta in figure A.5) greater than 50 deg (more
2691 reliable tracking)

2692 Tracks passing all these selection requirements are used for the Δt calculation.

2693 For each track passing our selection, we loop through the associated hits to retrieve
2694 the timing information. The analysis is performed separately on hits on the collection
2695 plane and induction plane, but lead to consistent results. As an example of the time
2696 difference, figures A.6 and A.7 represent the difference in time between the last and
2697 first hit of the selected tracks for Run-II Positive Polarity sample on the collection
2698 and induction plane respectively. We fit with a Gaussian to the peak of the Δt
2699 distributions to extract the mean drift time and the uncertainty associated with it.

2700 The long tail at low Δt represents contamination of non-ACP tracks in the track
2701 selection. We apply the same procedure to Run-I and Run-II, positive and negative
2702 polarity alike.

2703 To convert Δt recorded for the hits on the induction plane to the drift time we
2704 employ the formula

$$t_{drift} = \Delta t - t_{S-I} \quad (\text{A.6})$$

2705 where t_{drift} is the time the charge takes to drift in the main volume between the
2706 cathode and the shield plane and t_{S-I} is the time it takes for the charge to drift from
2707 the shield plane to the induction plane. In Table A.1 we calculated the drift velocity
2708 in the S-I region, thus we can calculate t_{S-I} as

$$t_{S-I} = \frac{l_{S-I}}{v_{S-I}} = \frac{4mm}{1.73mm/\mu s} \quad (\text{A.7})$$

2709 where l_{S-I} is the distance between the shield and induction plane and v_{S-I} is the drift
2710 velocity in the same region. A completely analogous procedure is followed for the hits
2711 on the collection plane, taking into account the time the charge spent in drifting from
2712 shield to induction as well as between the induction and collection plane. The value
2713 for Δt_{drift} , the calculated drift velocity (v_{drift}), and corresponding drift electric field
2714 for the various run periods is given in Table A.2 and are consistent with the electric
2715 field value calculated with the single line diagram method.

Delta t_{drift} , drift v and E field with ACP tracks

Data Period	Δt_{Drift} [μs]	Drift velocity [mm/ μs]	E field [V/cm]
RunI Positive Polarity Induction	311.1 ± 2.4	1.51 ± 0.01	486.6 ± 21
RunI Positive Polarity Collection	310.9 ± 2.6	1.51 ± 0.01	487.2 ± 21
RunII Positive Polarity Induction	315.7 ± 2.8	1.49 ± 0.01	467.9 ± 21
RunII Positive Polarity Collection	315.7 ± 2.7	1.49 ± 0.01	467.9 ± 21
RunII Negative Polarity Induction	315.9 ± 2.6	1.49 ± 0.01	467.1 ± 21
RunII Negative Polarity Collection	315.1 ± 2.8	1.49 ± 0.01	470.3 ± 21
Average Values	314.1	1.50 ± 0.01	474.3 ± 21

Table A.2: Δt for the different data samples used for the Anode-Cathode Piercing tracks study.

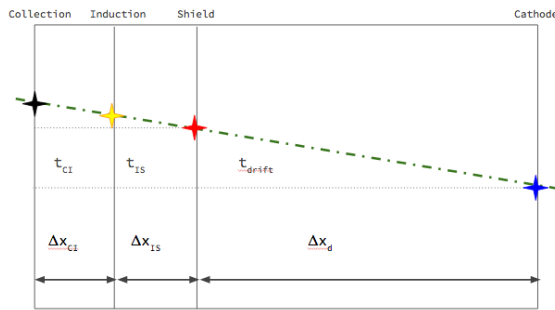


Figure A.4: Pictorial representation of the YX view of the TPC. The distance within the anode planes and between the shield plane and the cathode is purposely out of proportion to illustrate the time difference between hits on collection and induction. An ACP track is shown as an example.

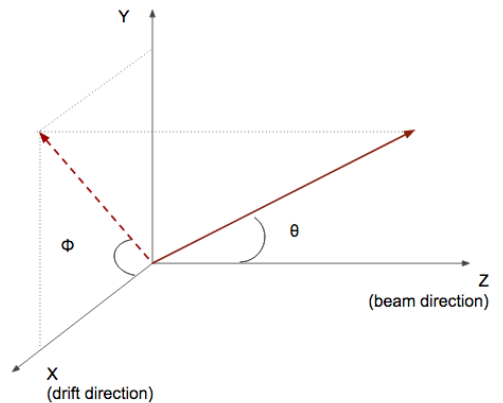


Figure A.5: Angle definition in the context of LArIAT coordinate system.

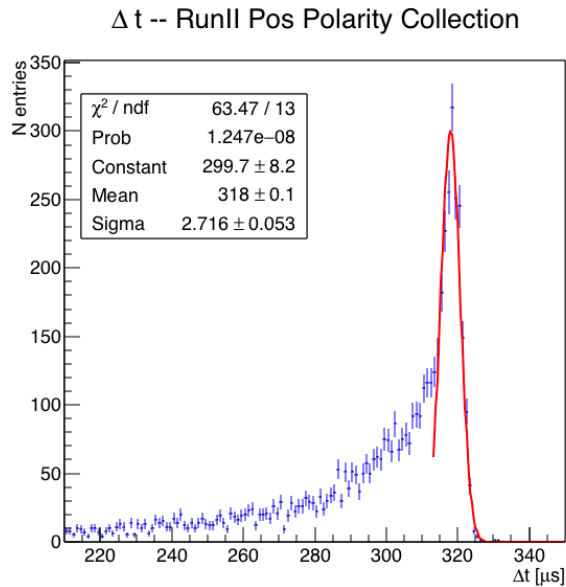


Figure A.6: Collection plane Δt fit for Run II positive polarity ACP data selected tracks.

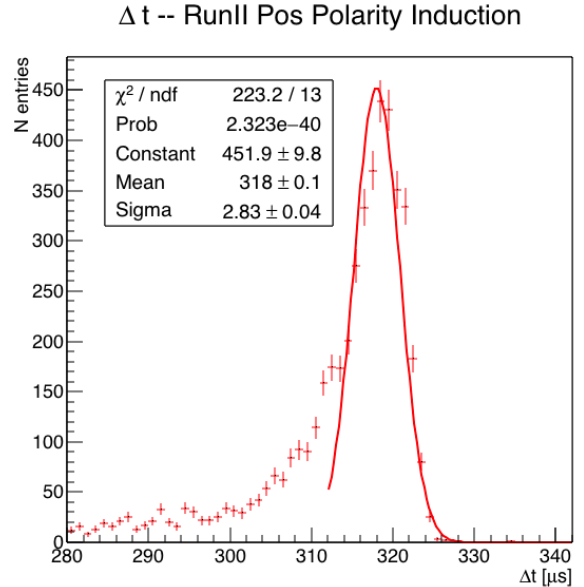


Figure A.7: Induction plane Δt fit for Run II positive polarity ACP data selected tracks.

²⁷¹⁶ **Appendix B**

²⁷¹⁷ **Additional Tracking Studies for**
²⁷¹⁸ **LArIAT Cross Section Analyses**

²⁷¹⁹ In this section, we describe two studies. The first is a justification of the selection
²⁷²⁰ criteria for the beamline handshake with the TPC information. We perform this
²⁷²¹ study to boost the correct identification of the particles in the TPC associated with
²⁷²² the beamline information, while maintaining sufficient statistics for the cross section
²⁷²³ measurement. The second study is an optimization of the tracking algorithm, with
²⁷²⁴ the scope of maximizing the identification of the hadronic interaction point inside the
²⁷²⁵ TPC. These two studies are related, since the optimization of the tracking is per-
²⁷²⁶ formed on TPC tracks which have been matched to the wire chamber track; in turn,
²⁷²⁷ the tracking algorithm for TPC tracks determines the number of reconstructed tracks
²⁷²⁸ in each event used to try the matching with the wire chamber track. Starting with
²⁷²⁹ a sensible tracking reconstruction, we perform the WC2TPC matching optimization
²⁷³⁰ first, then the tracking optimization. The WC2TPC match purity and efficiency are
²⁷³¹ then calculated again with the optimized tracking.

2732 **B.0.1 Study of WC to TPC Match**

2733 Scope of this study is assessing the performances of the WC2TPC match on Monte
2734 Carlo (see Section 4.2) and decide the selection values we will use on data. A
2735 word of caution is necessary here. With this study, we want to minimize pathologies
2736 associated with the presence of the primary hadron itself, e.g. the incorrect association
2737 between the beamline hadron and its decay products inside the TPC. Assessing the
2738 contamination from pile-up¹, albeit related, is beyond the scope of this study.

2739 In MC, we are able to define a correct WC2TPC match using the Geant4 truth
2740 information. We are thus able to count how many times the WC tracks is associated
2741 with the wrong TPC reconstructed track.

2742 We define a correct match if the all following conditions are met:

- 2743 - the length of the true primary Geant4 track in the TPC is greater than 2 cm,
2744 - the length of the reconstructed track length is greater than 2 cm,
2745 - the Z position of the first reconstructed point is within 2 cm from the TPC
2746 front face
2747 - the distance between the reconstructed track and the true entering point is the
2748 minimum compared with all the other reconstructed tracks.

2749 In order to count the wrong matches, we consider all the reconstructed tracks
2750 whose Z position of the first reconstructed point lies within 2 cm from the TPC front
2751 face. Events with true length in TPC < 2 cm are included. Since hadrons are shot
2752 100 cm upstream from the TPC front face, the following two scenarios are possible
2753 from a truth standpoint:

2754 [Ta] the primary hadron decays or interact strongly before getting to the TPC,

1. We remind the reader that the DDMC is a single particle Monte Carlo, where the beam pile up is not simulated.

2755 [Tb] the primary hadron enters the TPC.

2756 As described in Section 4.2, we define a WC2TPC match according to the relative
2757 position of the WC and TPC track parametrized with ΔR and the angle between
2758 them, parametrized with α . Once we choose the selection values r_T and α_T to de-
2759 termine a reconstructed WC2TPC match, the following five scenarios are possible in
2760 the truth to reconstruction interplay :

- 2761 1) only the correct track is matched
- 2762 2) only one wrong track is matched
- 2763 3) the correct track and one (or more) wrong tracks are matched
- 2764 4) multiple wrong tracks matched.
- 2765 5) no reconstructed tracks are matched

2766 Since we keep only events with one and only one match, we discard cases 3), 4)
2767 and 5) from the events used in the cross section measurement. For each set of r_T and
2768 α_T selection value, we define purity and efficiency of the selection as follows:

$$\text{Efficiency} = \frac{\text{Number of events correctly matched}}{\text{Number of events with primary in TPC}}, \quad (\text{B.1})$$

$$\text{Purity} = \frac{\text{Number of events correctly matched}}{\text{Total number of matched events}}. \quad (\text{B.2})$$

2769 Figure B.1 shows the efficiency (left) and purity (right) for WC2TPC match as
2770 a function of the radius, r_T , and angle, α_T , selection value. It is apparent how both
2771 efficiency and purity are fairly flat as a function of the radius selection value at a
2772 given angle. This is not surprising. Since we are studying a single particle gun Monte
2773 Carlo sample, the wrong matches can occur only for mis-tracking of the primary or

for association with decay products; decay products will tend to be produced at large angles compared to the primary, but could be fairly close to the in x and y projection of the primary. The radius cut would play a key role in removing pile up events.

For LArIAT cross section measurements, we generally prefer purity over efficiency, since a sample of particles of a pure species will lead to a better measurement. Obviously, purity should be balanced with a sensible efficiency to avoid rejecting the whole sample.

We choose $(\alpha_T, r_T) = (8 \text{ deg}, 4 \text{ cm})$ and get a MC 85% efficiency and 98% purity for the kaon sample and a MC 95% efficiency and 90% purity for the pion sample.

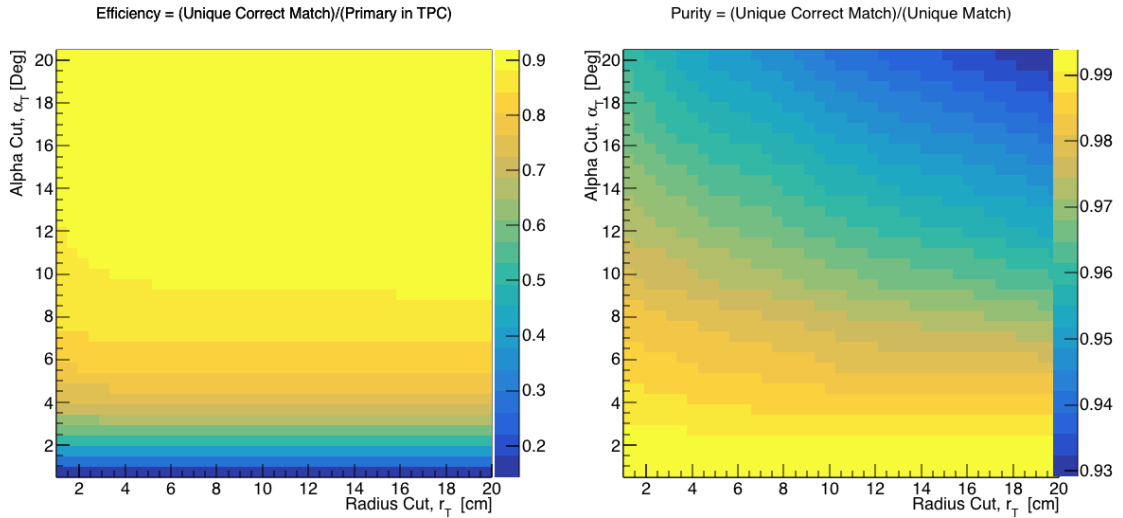


Figure B.1: Efficiency (left) and purity (right) for WC2TPC match as a function of the radius and angle selections for the kaon sample.

B.0.2 Tracking Optimization

We perform an optimization of the clustering algorithm (see Section 2.1.5) with the scope of maximizing the efficiency of finding the interaction point for the total hadronic cross section measurements. We define as the interaction point the most downstream point of a WC2TPC matched TPC tracks within the TPC fiducial volume. Since all the WC2TPC tracks are by definition beam particles, tracks travel

2789 from upstream to downstream in the TPC; thus, identifying the interaction point
2790 means to stop the tracking correctly.

2791 TrajCluster is the package used to cluster hits in LArIAT; this package counts more
2792 than 20 tunable parameters. A standard method to develop clustering algorithms and
2793 checking their performances is to “hand scan”, which means recognizing the effect of
2794 parameters tuning by looking at a series of data event displays. Albeit we recognize
2795 the importance of hand scanning as a great diagnosis tool, we developed a fully
2796 automated optimization package which compares MC reconstructed information to
2797 MC truth.

2798 We start by defining a figure of merit in order to discern what makes a parameter
2799 configuration better than an other. We chose the percentage of events whose recon-
2800 structed and true length differ less than 2 cm. We then identify the parameters in
2801 TrajCluster that are most important to correctly stop the tracking and an appropriate
2802 range of values for each of them. We chose to optimize the parameters that leverage
2803 on the angle between consecutive groups of hits, the number of hits use in the cluster
2804 fit and the average hit charge to stop the tracking. We define a configuration space
2805 with all possible combination of values for the chosen parameters and we perform
2806 reconstruction one combination at a time: the combination with the highest figure of
2807 merit determines the optimized tracking reconstruction.

2808 We chose construct the combination space using a total of 5 parameters, 3 values
2809 each and two iterations of the method (for a total of 486 combinations). We run the
2810 combinations on a sample of 100000 pion events. After the optimization, the most
2811 upstream point of the tracking is correctly identified 99.5% of the times, the most
2812 downstream point is correctly identified 62.5% of the times, the tracking stops short
2813 about 15% of the times and misses the interaction point 22.5% of the times. Hand
2814 scanning confirmed that the missed interaction points happen in the vast majority of
2815 cases for very shallow angles, as shown in the event display in Figure, or in the case

2816 of angles visible only in one projection plane. We also noticed that the premature
2817 stopping of the tracks is often related to the presence of delta rays parallel to the
2818 track. We see room of improvement, such as the delta ray removal and a forced track
2819 breaking in case of a kink present in a single plane, for a future analysis. **ADD evd**

2820 The procedure behind this optimization package is virtually applicable to any
2821 LArSoft module where it is possible to define figure of merit.

2822 **Appendix C**

2823 **Energy Calibration**

2824 Scope of the energy calibration is to identify the factors which convert the charge
2825 collected (dQ) to energy deposited in the chamber (dE). As described in section
2826 2.1.5, this is a multi-step procedure. In LArIAT, we first correct the raw charge by
2827 the electronic noise on the considered wire [103], then by the electron lifetime [104],
2828 and then by the recombination using the ArgoNeut recombination values. Lastly, we
2829 apply overall calibration of the energy, i.e. we determine the “calorimetry constants”
2830 using the procedure described in this section.

2831 We independently determine the calorimetry constants for Data and Monte Carlo
2832 in the LArIAT Run-II Data samples using a parametrization of the stopping power
2833 (a.k.a. energy deposited per unit length, dE/dX) as a function of momentum. This is
2834 done by comparing the stopping power measured on reconstructed quantities against
2835 the Bethe-Bloch theoretical prediction for various particle species (see Equation 2.1).
2836 We obtain the theoretical expectation for the dE/dX most probable value of pions
2837 (π), muons (μ), kaons (K), and protons (p) in the momentum range most relevant
2838 for LArIAT (Figure C.1) using the tables provided by the Particle Data Group [101]
2839 for liquid argon [1].

2840 The basic idea of this calibration technique is to utilize a sample of beamline

2841 events with known particle species and momentum to measure the dE/dX of the
2842 corresponding tracks in the TPC. In particular, we decided to use positive pions as
2843 calibration sample and samples from all the other particle species as cross check. Once
2844 the dE/dX of the positive pion sample has been measured at various momenta, we
2845 tune to calorimetry constants within the reconstruction software to align the measured
2846 values to match the theoretical ones found in Figure C.1.

2847 In data, we start by selecting a sample of beamline positive pion beamline can-
2848 didates without any restriction on their measured momentum¹. We then apply the
2849 WC2TPC match and subtract the energy loss upstream to the TPC front face, de-
2850 termining the momentum at the TPC front face. For each surviving pion candidate,
2851 we measure the dE/dx at each of the first 12 spacepoints associated the 3D recon-
2852 structed track, corresponding to a ~ 5 cm portion. These dE/dX measurements are
2853 then put into a histogram that corresponds to measured momentum of the track.
2854 The dE/dX histograms are sampled every 50 MeV/c in momentum (e.g. 150 MeV/c
2855 $< P < 200$ MeV/c, 200 MeV/c $< P < 250$ /c MeV, etc...). This process of selecting,
2856 sampling, and recording the dE/dX for various momentum bins is repeated over the
2857 entire sample of events, allowing us to collect sufficient statistic in most of the mo-
2858 mentum bins between 150 MeV/c and 1100 MeV/c. On average, pions and muons
2859 only lose ~ 10 MeV in this 5 cm section of the track and protons lose ~ 20 MeV. Thus
2860 choosing 50 MeV/c size bins for our histograms covers the energy spread within those
2861 bins due to energy loss from ionization for all the particle species identifiable in the
2862 beamline. Each 50 MeV/c momentum binned dE/dX histogram is now fit with a
2863 simple Landau function. The most probable value (MPV) and the associated error
2864 on the MPV from the fit are extracted and plotted against the theoretical prediction
2865 Figure C.1. Depending on the outcome of the data-prediction comparison, we modify
2866 the calorimetry constants and we repeat the procedure until a qualitative agreement

1. it should be noted that some muon and position contamination is present in the π^+ sample

2867 is achieved. We perform this tuning for the collection and induction plane separately.
 2868 As a cross check to the calorimetry constants determined using the positive pions,
 2869 we lock the constants and plot the dE/dx versus momentum distribution of all the
 2870 other particle species identifiable in the beamline data ($\pi/\mu/e$, K , p, in both polarities)
 2871 against the corresponding Beth-Bloch prediction. The agreement between data
 2872 from the other particle species and the predictions is the expected result of this cross
 2873 check. The results of the tuning and cross check for Run-II data on the collection
 2874 plane is shown in Figure C.2 negative polarity data on top, positive polarity data on
 2875 the bottom.

2876 In MC, we simulate the corresponding positive pion sample with the DDMC (see
 2877 section 5.2.2) and follow the same steps as in data. More details on the calorimetry
 2878 tuning can be found in [79].

2879 **Add agreement between data and MC for dedx for pions**

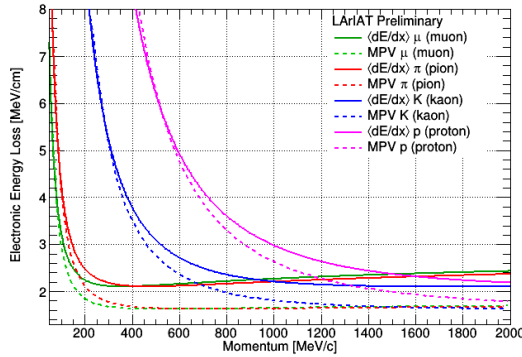


Figure C.1: Stopping power for pions, muons, kaons, and protons in liquid argon over the momentum range most relevant for LArIAT according to the Beth-Bloch equation. The solid lines represent the prediction for the mean energy dE/dX , while the dashed lines are the predictions for the MPV.

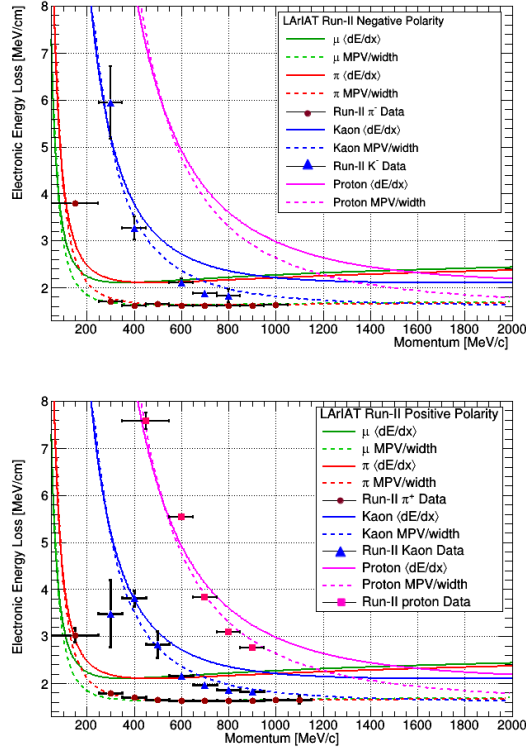


Figure C.2: Stopping power versus Momentum for Run-II negative (top) and positive (bottom) polarity data. We achieve the agreement between the Bethe-Bloch predictions and the distribution obtained with of the positive pions (top plot, red dots) by tuning the calorimetry constants. Once the calorimetry constants are locked in, the agreement between the other particle species and the Bethe-Bloch predictions follows naturally.

2880 **Bibliography**

- 2881 [1] PDG Tables for Liquid Argon. . Technical report.
- 2882 [2] Precision electroweak measurements on the Z resonance. *Physics Reports*,
2883 427(5):257 – 454, 2006.
- 2884 [3] K. Abe, J. Amey, C. Andreopoulos, M. Antonova, S. Aoki, A. Ariga, D. Au-
2885 tiero, S. Ban, M. Barbi, G. J. Barker, G. Barr, C. Barry, P. Bartet-Friburg,
2886 M. Batkiewicz, V. Berardi, S. Berkman, S. Bhadra, S. Bienstock, A. Blondel,
2887 S. Bolognesi, S. Bordoni, S. B. Boyd, D. Brailsford, A. Bravar, C. Bronner,
2888 M. Buizza Avanzini, R. G. Calland, T. Campbell, S. Cao, S. L. Cartwright,
2889 M. G. Catanesi, A. Cervera, C. Checchia, D. Cherdack, N. Chikuma,
2890 G. Christodoulou, A. Clifton, J. Coleman, G. Collazuol, D. Coplowe, A. Cudd,
2891 A. Dabrowska, G. De Rosa, T. Dealtry, P. F. Denner, S. R. Dennis, C. Densham,
2892 D. Dewhurst, F. Di Lodovico, S. Di Luise, S. Dolan, O. Drapier, K. E. Duffy,
2893 J. Dumarchez, M. Dziewiecki, S. Emery-Schrenk, A. Ereditato, T. Feusels,
2894 A. J. Finch, G. A. Fiorentini, M. Friend, Y. Fujii, D. Fukuda, Y. Fukuda,
2895 V. Galymov, A. Garcia, C. Giganti, F. Gizzarelli, T. Golan, M. Gonin, D. R.
2896 Hadley, L. Haegel, M. D. Haigh, D. Hansen, J. Harada, M. Hartz, T. Hasegawa,
2897 N. C. Hastings, T. Hayashino, Y. Hayato, R. L. Helmer, A. Hillairet, T. Hiraki,
2898 A. Hiramoto, S. Hirota, M. Hogan, J. Holeczek, F. Hosomi, K. Huang, A. K.
2899 Ichikawa, M. Ikeda, J. Imber, J. Insler, R. A. Intonti, T. Ishida, T. Ishii, E. Iwai,
2900 K. Iwamoto, A. Izmaylov, B. Jamieson, M. Jiang, S. Johnson, P. Jonsson,

2901 C. K. Jung, M. Kabirnezhad, A. C. Kaboth, T. Kajita, H. Kakuno, J. Kameda,
2902 D. Karlen, T. Katori, E. Kearns, M. Khabibullin, A. Khotjantsev, H. Kim,
2903 J. Kim, S. King, J. Kisiel, A. Knight, A. Knox, T. Kobayashi, L. Koch, T. Koga,
2904 A. Konaka, K. Kondo, L. L. Kormos, A. Korzenev, Y. Koshio, K. Kowalik,
2905 W. Kropp, Y. Kudenko, R. Kurjata, T. Kutter, J. Lagoda, I. Lamont, M. Lam-
2906 oureux, E. Larkin, P. Lasorak, M. Laveder, M. Lawe, M. Licciardi, T. Lindner,
2907 Z. J. Liptak, R. P. Litchfield, X. Li, A. Longhin, J. P. Lopez, T. Lou, L. Ludovici,
2908 X. Lu, L. Magaletti, K. Mahn, M. Malek, S. Manly, A. D. Marino, J. F. Martin,
2909 P. Martins, S. Martynenko, T. Maruyama, V. Matveev, K. Mavrokordis, W. Y.
2910 Ma, E. Mazzucato, M. McCarthy, N. McCauley, K. S. McFarland, C. McGrew,
2911 A. Mefodiev, C. Metelko, M. Mezzetto, P. Mijakowski, A. Minamino, O. Mi-
2912 neev, S. Mine, A. Missent, M. Miura, S. Moriyama, Th. A. Mueller, J. Myslik,
2913 T. Nakadaira, M. Nakahata, K. G. Nakamura, K. Nakamura, K. D. Nakamura,
2914 Y. Nakanishi, S. Nakayama, T. Nakaya, K. Nakayoshi, C. Nantais, C. Nielsen,
2915 M. Nirko, K. Nishikawa, Y. Nishimura, P. Novella, J. Nowak, H. M. O'Keeffe,
2916 K. Okumura, T. Okusawa, W. Oryszczak, S. M. Oser, T. Ovsyannikova, R. A.
2917 Owen, Y. Oyama, V. Palladino, J. L. Palomino, V. Paolone, N. D. Patel,
2918 P. Paudyal, M. Pavin, D. Payne, J. D. Perkin, Y. Petrov, L. Pickard, L. Pick-
2919 ering, E. S. Pinzon Guerra, C. Pistillo, B. Popov, M. Posiadala-Zezula, J.-M.
2920 Poutissou, R. Poutissou, P. Przewlocki, B. Quilain, T. Radermacher, E. Radi-
2921 cioni, P. N. Ratoff, M. Ravonel, M. A. Rayner, A. Redij, E. Reinherz-Aronis,
2922 C. Riccio, P. A. Rodrigues, E. Rondio, B. Rossi, S. Roth, A. Rubbia, A. Rychter,
2923 K. Sakashita, F. Sánchez, E. Scantamburlo, K. Scholberg, J. Schwehr, M. Scott,
2924 Y. Seiya, T. Sekiguchi, H. Sekiya, D. Sgalaberna, R. Shah, A. Shaikhiev,
2925 F. Shaker, D. Shaw, M. Shiozawa, T. Shirahige, S. Short, M. Smy, J. T.
2926 Sobczyk, H. Sobel, M. Sorel, L. Southwell, J. Steinmann, T. Stewart, P. Stowell,
2927 Y. Suda, S. Suvorov, A. Suzuki, S. Y. Suzuki, Y. Suzuki, R. Tacik, M. Tada,

- 2928 A. Takeda, Y. Takeuchi, H. K. Tanaka, H. A. Tanaka, D. Terhorst, R. Terri,
2929 T. Thakore, L. F. Thompson, S. Tobayama, W. Toki, T. Tomura, C. Touramani,
2930 T. Tsukamoto, M. Tzanov, Y. Uchida, M. Vagins, Z. Vallari, G. Vasseur,
2931 T. Vladislavljevic, T. Wachala, C. W. Walter, D. Wark, M. O. Wascko, A. We-
2932 ber, R. Wendell, R. J. Wilkes, M. J. Wilking, C. Wilkinson, J. R. Wilson, R. J.
2933 Wilson, C. Wret, Y. Yamada, K. Yamamoto, M. Yamamoto, C. Yanagisawa,
2934 T. Yano, S. Yen, N. Yershov, M. Yokoyama, K. Yoshida, T. Yuan, M. Yu, A. Za-
2935 lewska, J. Zalipska, L. Zambelli, K. Zaremba, M. Ziembicki, E. D. Zimmerman,
2936 M. Zito, and J. Źmuda. Combined analysis of neutrino and antineutrino oscil-
2937 lations at t2k. *Phys. Rev. Lett.*, 118:151801, Apr 2017.
- 2938 [4] K. Abe, Y. Haga, Y. Hayato, M. Ikeda, K. Iyogi, J. Kameda, Y. Kishimoto,
2939 M. Miura, S. Moriyama, M. Nakahata, T. Nakajima, Y. Nakano, S. Nakayama,
2940 A. Orii, H. Sekiya, M. Shiozawa, A. Takeda, H. Tanaka, T. Tomura, R. A. Wen-
2941 dell, R. Akutsu, T. Irvine, T. Kajita, K. Kaneyuki, Y. Nishimura, E. Richard,
2942 K. Okumura, L. Labarga, P. Fernandez, J. Gustafson, C. Kachulis, E. Kearns,
2943 J. L. Raaf, J. L. Stone, L. R. Sulak, S. Berkman, C. M. Nantais, H. A.
2944 Tanaka, S. Tobayama, M. Goldhaber, W. R. Kropp, S. Mine, P. Weatherly,
2945 M. B. Smy, H. W. Sobel, V. Takhistov, K. S. Ganezer, B. L. Hartfiel, J. Hill,
2946 N. Hong, J. Y. Kim, I. T. Lim, R. G. Park, A. Himmel, Z. Li, E. O’Sullivan,
2947 K. Scholberg, C. W. Walter, T. Wongjirad, T. Ishizuka, S. Tasaka, J. S. Jang,
2948 J. G. Learned, S. Matsuno, S. N. Smith, M. Friend, T. Hasegawa, T. Ishida,
2949 T. Ishii, T. Kobayashi, T. Nakadaira, K. Nakamura, Y. Oyama, K. Sakashita,
2950 T. Sekiguchi, T. Tsukamoto, A. T. Suzuki, Y. Takeuchi, T. Yano, S. V. Cao,
2951 T. Hiraki, S. Hirota, K. Huang, T. Kikawa, A. Minamino, T. Nakaya, K. Suzuki,
2952 Y. Fukuda, K. Choi, Y. Itow, T. Suzuki, P. Mijakowski, K. Frankiewicz, J. Hig-
2953 night, J. Imber, C. K. Jung, X. Li, J. L. Palomino, M. J. Wilking, C. Yanag-
2954 isawa, D. Fukuda, H. Ishino, T. Kayano, A. Kibayashi, Y. Koshio, T. Mori,

- 2955 M. Sakuda, C. Xu, Y. Kuno, R. Tacik, S. B. Kim, H. Okazawa, Y. Choi,
2956 K. Nishijima, M. Koshiba, Y. Totsuka, Y. Suda, M. Yokoyama, C. Bronner,
2957 M. Hartz, K. Martens, Ll. Marti, Y. Suzuki, M. R. Vagins, J. F. Martin, A. Kon-
2958 aka, S. Chen, Y. Zhang, and R. J. Wilkes. Search for proton decay via $p \rightarrow e^+ \pi^0$
2959 and $p \rightarrow \mu^+ \pi^0$ in 0.31 megaton · years exposure of the super-kamiokande water
2960 cherenkov detector. *Phys. Rev. D*, 95:012004, Jan 2017.
- 2961 [5] R Acciarri, C Adams, J Asaadi, B Baller, T Bolton, C Bromberg, F Ca-
2962 vanna, E Church, D Edmunds, A Ereditato, S Farooq, B Fleming, H Greenlee,
2963 G Horton-Smith, C James, E Klein, K Lang, P Laurens, D McKee, R Mehdiyev,
2964 B Page, O Palamara, K Partyka, G Rameika, B Rebel, M Soderberg, J Spitz,
2965 A M Szelc, M Weber, M Wojcik, T Yang, and G P Zeller. A study of electron
2966 recombination using highly ionizing particles in the argoneut liquid argon tpc.
2967 *Journal of Instrumentation*, 8(08):P08005, 2013.
- 2968 [6] R Acciarri, M Antonello, B Baibussinov, M Baldo-Ceolin, P Benetti,
2969 F Calaprice, E Calligarich, M Cambiaghi, N Canci, F Carbonara, F Cavanna,
2970 S Centro, A G Cocco, F Di Pompeo, G Fiorillo, C Galbiati, V Gallo, L Grandi,
2971 G Meng, I Modena, C Montanari, O Palamara, L Pandola, G B Piano Mortari,
2972 F Pietropaolo, G L Raselli, M Roncadelli, M Rossella, C Rubbia, E Segreto,
2973 A M Szelc, S Ventura, and C Vignoli. Effects of nitrogen contamination in
2974 liquid argon. *Journal of Instrumentation*, 5(06):P06003, 2010.
- 2975 [7] R. Acciarri et al. Demonstration and Comparison of Operation of Photomulti-
2976 plier Tubes at Liquid Argon Temperature. *JINST*, 7:P01016, 2012.
- 2977 [8] R. Acciarri et al. Design and Construction of the MicroBooNE Detector. *JINST*,
2978 12(02):P02017, 2017.

- 2979 [9] R. Acciarri et al. First Observation of Low Energy Electron Neutrinos in a
2980 Liquid Argon Time Projection Chamber. *Phys. Rev.*, D95(7):072005, 2017.
2981 [Phys. Rev.D95,072005(2017)].
- 2982 [10] M Adamowski, B Carls, E Dvorak, A Hahn, W Jaskierny, C Johnson, H Jostlein,
2983 C Kendziora, S Lockwitz, B Pahlka, R Plunkett, S Pordes, B Rebel, R Schmitt,
2984 M Stancari, T Tope, E Voirin, and T Yang. The liquid argon purity demon-
2985 strator. *Journal of Instrumentation*, 9(07):P07005, 2014.
- 2986 [11] C. Adams et al. The Long-Baseline Neutrino Experiment: Exploring Funda-
2987 mental Symmetries of the Universe. 2013.
- 2988 [12] P. Adamson, L. Aliaga, D. Ambrose, N. Anfimov, A. Antoshkin, E. Arrieta-
2989 Diaz, K. Augsten, A. Aurisano, C. Backhouse, M. Baird, B. A. Bambah,
2990 K. Bays, B. Behera, S. Bending, R. Bernstein, V. Bhatnagar, B. Bhuyan,
2991 J. Bian, T. Blackburn, A. Bolshakova, C. Bromberg, J. Brown, G. Brunetti,
2992 N. Buchanan, A. Butkevich, V. Bychkov, M. Campbell, E. Catano-Mur, S. Chil-
2993 dress, B. C. Choudhary, B. Chowdhury, T. E. Coan, J. A. B. Coelho, M. Colo,
2994 J. Cooper, L. Corwin, L. Cremonesi, D. Cronin-Hennessy, G. S. Davies, J. P.
2995 Davies, P. F. Derwent, R. Dharmapalan, P. Ding, Z. Djurcic, E. C. Dukes,
2996 H. Duyang, S. Edayath, R. Ehrlich, G. J. Feldman, M. J. Frank, M. Gabrielyan,
2997 H. R. Gallagher, S. Germani, T. Ghosh, A. Giri, R. A. Gomes, M. C. Goodman,
2998 V. Grichine, R. Group, D. Grover, B. Guo, A. Habig, J. Hartnell, R. Hatcher,
2999 A. Hatzikoutelis, K. Heller, A. Himmel, A. Holin, J. Hylen, F. Jediny, M. Judah,
3000 G. K. Kafka, D. Kalra, S. M. S. Kasahara, S. Kasetti, R. Keloth, L. Kolupaeva,
3001 S. Kotelnikov, I. Kourbanis, A. Kreymer, A. Kumar, S. Kurbanov, K. Lang,
3002 W. M. Lee, S. Lin, J. Liu, M. Lokajicek, J. Lozier, S. Luchuk, K. Maan, S. Mag-
3003 ill, W. A. Mann, M. L. Marshak, K. Matera, V. Matveev, D. P. Méndez, M. D.
3004 Messier, H. Meyer, T. Miao, W. H. Miller, S. R. Mishra, R. Mohanta, A. Moren,

- 3005 L. Mualem, M. Muether, S. Mufson, R. Murphy, J. Musser, J. K. Nelson,
3006 R. Nichol, E. Niner, A. Norman, T. Nosek, Y. Oksuzian, A. Olshevskiy, T. Ol-
3007 son, J. Paley, P. Pandey, R. B. Patterson, G. Pawloski, D. Pershey, O. Petrova,
3008 R. Petti, S. Phan-Budd, R. K. Plunkett, R. Poling, B. Potukuchi, C. Principato,
3009 F. Psihas, A. Radovic, R. A. Rameika, B. Rebel, B. Reed, D. Rocco, P. Rojas,
3010 V. Ryabov, K. Sachdev, P. Sail, O. Samoylov, M. C. Sanchez, R. Schroeter,
3011 J. Sepulveda-Quiroz, P. Shanahan, A. Sheshukov, J. Singh, J. Singh, P. Singh,
3012 V. Singh, J. Smolik, N. Solomey, E. Song, A. Sousa, K. Soustruznik, M. Strait,
3013 L. Suter, R. L. Talaga, M. C. Tamsett, P. Tas, R. B. Thayyullathil, J. Thomas,
3014 X. Tian, S. C. Tognini, J. Tripathi, A. Tsaris, J. Urheim, P. Vahle, J. Vasel,
3015 L. Vinton, A. Vold, T. Vrba, B. Wang, M. Wetstein, D. Whittington, S. G. Wo-
3016 jcicki, J. Wolcott, N. Yadav, S. Yang, J. Zalesak, B. Zamorano, and R. Zwaska.
3017 Constraints on oscillation parameters from ν_e appearance and ν_μ disappearance
3018 in nova. *Phys. Rev. Lett.*, 118:231801, Jun 2017.
- 3019 [13] Alan Agresti. *Categorical Data Analysis*. Wiley Series in Probability and Statis-
3020 tics. Wiley, 2013.
- 3021 [14] A. Aguilar-Arevalo et al. Evidence for neutrino oscillations from the observation
3022 of anti-neutrino(electron) appearance in a anti-neutrino(muon) beam. *Phys.*
3023 *Rev.*, D64:112007, 2001.
- 3024 [15] A. A. Aguilar-Arevalo et al. Improved Search for $\bar{\nu}_\mu \rightarrow \bar{\nu}_e$ Oscillations in the
3025 MiniBooNE Experiment. *Phys. Rev. Lett.*, 110:161801, 2013.
- 3026 [16] S. Amoruso et al. Study of electron recombination in liquid argon with the
3027 ICARUS TPC. *Nucl. Instrum. Meth.*, A523:275–286, 2004.
- 3028 [17] C. Anderson et al. The ArgoNeuT Detector in the NuMI Low-Energy beam
3029 line at Fermilab. *JINST*, 7:P10019, 2012.

- 3030 [18] C. Andreopoulos et al. The GENIE Neutrino Monte Carlo Generator. *Nucl.*
3031 *Instrum. Meth.*, A614:87–104, 2010.
- 3032 [19] Timofei Bolshakov Andrey Petrov. Java synoptic toolkit. Technical report,
3033 Sept 2010.
- 3034 [20] M. Antonello, B. Baibussinov, P. Benetti, E. Calligarich, N. Canci, S. Cen-
3035 tro, A. Cesana, K. Cieslik, D. B. Cline, A. G. Cocco, A. Dabrowska, D. De-
3036 qual, A. Dermenev, R. Dolfini, C. Farnese, A. Fava, A. Ferrari, G. Fiorillo,
3037 D. Gibin, S. Gninenko, A. Guglielmi, M. Haranczyk, J. Holeczek, A. Ivashkin,
3038 J. Kisiel, I. Kochanek, J. Lagoda, S. Mania, A. Menegolli, G. Meng, C. Monta-
3039 nari, S. Otwinowski, A. Piazzoli, P. Picchi, F. Pietropaolo, P. Plonski, A. Rap-
3040 poldi, G. L. Raselli, M. Rossella, C. Rubbia, P. Sala, A. Scaramelli, E. Seg-
3041 reto, F. Sergiampietri, D. Stefan, J. Stepaniak, R. Sulej, M. Szarska, M. Ter-
3042 rani, F. Varanini, S. Ventura, C. Vignoli, H. Wang, X. Yang, A. Zalewska,
3043 and K. Zaremba. Precise 3d track reconstruction algorithm for the ICARUS
3044 t600 liquid argon time projection chamber detector. *Advances in High Energy*
3045 *Physics*, 2013:1–16, 2013.
- 3046 [21] M. Antonello et al. A Proposal for a Three Detector Short-Baseline Neutrino
3047 Oscillation Program in the Fermilab Booster Neutrino Beam. 2015.
- 3048 [22] D. Ashery, I. Navon, G. Azuelos, H. K. Walter, H. J. Pfeiffer, and F. W.
3049 Schlepütz. True absorption and scattering of pions on nuclei. *Phys. Rev. C*,
3050 23:2173–2185, May 1981.
- 3051 [23] C. Athanassopoulos et al. Evidence for $\nu(\mu) \rightarrow \nu(e)$ neutrino oscillations
3052 from LSND. *Phys. Rev. Lett.*, 81:1774–1777, 1998.

- 3053 [24] Borut Bajc, Junji Hisano, Takumi Kuwahara, and Yuji Omura. Threshold
3054 corrections to dimension-six proton decay operators in non-minimal {SUSY}
3055 $\text{su}(5)$ {GUTs}. *Nuclear Physics B*, 910:1 – 22, 2016.
- 3056 [25] B. Baller. Trajcluster user guide. Technical report, apr 2016.
- 3057 [26] Gary Barker. Neutrino event reconstruction in a liquid argon TPC. *Journal of*
3058 *Physics: Conference Series*, 308:012015, jul 2011.
- 3059 [27] BASF Corp. 100 Park Avenue, Florham Park, NJ 07932 USA.
- 3060 [28] R. Becker-Szendy, C. B. Bratton, D. R. Cady, D. Casper, R. Claus, M. Crouch,
3061 S. T. Dye, W. Gajewski, M. Goldhaber, T. J. Haines, P. G. Halverson, T. W.
3062 Jones, D. Kielczewska, W. R. Kropp, J. G. Learned, J. M. LoSecco, C. Mc-
3063 Grew, S. Matsuno, J. Matthews, M. S. Mudah, L. Price, F. Reines, J. Schultz,
3064 D. Sinclair, H. W. Sobel, J. L. Stone, L. R. Sulak, R. Svoboda, G. Thornton,
3065 and J. C. van der Velde. Search for proton decay into $e^+ + \pi^0$ in the imb-3
3066 detector. *Phys. Rev. D*, 42:2974–2976, Nov 1990.
- 3067 [29] J B Birks. Scintillations from organic crystals: Specific fluorescence and relative
3068 response to different radiations. *Proceedings of the Physical Society. Section A*,
3069 64(10):874, 1951.
- 3070 [30] A. Bodek and J. L. Ritchie. Further studies of fermi-motion effects in lepton
3071 scattering from nuclear targets. *Phys. Rev. D*, 24:1400–1402, Sep 1981.
- 3072 [31] Mark G. Boulay and A. Hime. Direct WIMP detection using scintillation time
3073 discrimination in liquid argon. 2004.
- 3074 [32] D. V. Bugg, R. S. Gilmore, K. M. Knight, D. C. Salter, G. H. Stafford, E. J. N.
3075 Wilson, J. D. Davies, J. D. Dowell, P. M. Hattersley, R. J. Homer, A. W. O'dell,

- 3076 A. A. Carter, R. J. Tapper, and K. F. Riley. Kaon-nucleon total cross sections
3077 from 0.6 to 2.65 gev/ *c. Phys. Rev.*, 168:1466–1475, Apr 1968.
- 3078 [33] W. M. Burton and B. A. Powell. Fluorescence of tetraphenyl-butadiene in the
3079 vacuum ultraviolet. *Applied Optics*, 12(1):87, jan 1973.
- 3080 [34] CAEN. Caen v1495 data sheet. Technical report, jan 2018.
- 3081 [35] CAEN. Caen v1740 data sheet. Technical report, jan 2018.
- 3082 [36] A. S. Carroll, I. H. Chiang, C. B. Dover, T. F. Kycia, K. K. Li, P. O. Mazur,
3083 D. N. Michael, P. M. Mockett, D. C. Rahm, and R. Rubinstein. Pion-nucleus
3084 total cross sections in the (3,3) resonance region. *Phys. Rev. C*, 14:635–638,
3085 Aug 1976.
- 3086 [37] D. Casper. The nuance neutrino physics simulation, and the future. *Nuclear
3087 Physics B - Proceedings Supplements*, 112(1-3):161–170, nov 2002.
- 3088 [38] F. Cavanna et al. LArIAT: Liquid Argon In A Testbeam. 2014.
- 3089 [39] A. Cervera, A. Donini, M.B. Gavela, J.J. Gomez Cádenas, P. Hernández,
3090 O. Mena, and S. Rigolin. Golden measurements at a neutrino factory. *Nu-
3091 clear Physics B*, 579(1-2):17–55, jul 2000.
- 3092 [40] E. Church. LArSoft: A Software Package for Liquid Argon Time Projection
3093 Drift Chambers. 2013.
- 3094 [41] ATLAS Collaboration. Observation of a new particle in the search for the
3095 standard model higgs boson with the ATLAS detector at the LHC. *Physics
3096 Letters B*, 716(1):1–29, sep 2012.
- 3097 [42] CMS Collaboration. Observation of a new boson at a mass of 125 gev with the
3098 cms experiment at the lhc. *Physics Letters B*, 716(1):30 – 61, 2012.

- 3099 [43] The LArIAT Collaboration. The liquid argon in a testbeam (lariat) experiment.
3100 Technical report, In Preparation 2018.
- 3101 [44] Stefano Dell’Oro, Simone Marcocci, Matteo Viel, and Francesco Vissani. Neu-
3102 trinoless double beta decay: 2015 review. *Advances in High Energy Physics*,
3103 2016:1–37, 2016.
- 3104 [45] S.E. Derenzo, A.R. Kirschbaum, P.H. Eberhard, R.R. Ross, and F.T. Solmitz.
3105 Test of a liquid argon chamber with 20 m rms resolution. *Nuclear Instruments
3106 and Methods*, 122:319 – 327, 1974.
- 3107 [46] Savas Dimopoulos, Stuart Raby, and Frank Wilczek. Proton Decay in Super-
3108 symmetric Models. *Phys. Lett.*, B112:133, 1982.
- 3109 [47] D. Drakoulakos et al. Proposal to perform a high-statistics neutrino scattering
3110 experiment using a fine-grained detector in the NuMI beam. 2004.
- 3111 [48] A Ereditato, C C Hsu, S Janos, I Kreslo, M Messina, C Rudolf von Rohr,
3112 B Rossi, T Strauss, M S Weber, and M Zeller. Design and operation of
3113 argontube: a 5 m long drift liquid argon tpc. *Journal of Instrumentation*,
3114 8(07):P07002, 2013.
- 3115 [49] Torleif Ericson and Wolfram Weise. *Pions and Nuclei (The International Series
3116 of Monographs on Physics)*. Oxford University Press, 1988.
- 3117 [50] A.A. Aguilar-Arevalo et al. The miniboone detector. *Nuclear Instruments and
3118 Methods in Physics Research Section A: Accelerators, Spectrometers, Detectors
3119 and Associated Equipment*, 599(1):28 – 46, 2009.
- 3120 [51] Antonio Bueno et al. Nucleon decay searches with large liquid argon TPC de-
3121 tectors at shallow depths: atmospheric neutrinos and cosmogenic backgrounds.
3122 *Journal of High Energy Physics*, 2007(04):041–041, apr 2007.

- 3123 [52] A.S. Clough et al. Pion-nucleus total cross sections from 88 to 860 MeV. *Nuclear*
3124 *Physics B*, 76(1):15–28, jul 1974.
- 3125 [53] B.W. Allardycce et al. Pion reaction cross sections and nuclear sizes. *Nuclear*
3126 *Physics A*, 209(1):1 – 51, 1973.
- 3127 [54] C Athanassopoulos et al. The liquid scintillator neutrino detector and LAMPF
3128 neutrino source. *Nuclear Instruments and Methods in Physics Research Section*
3129 *A: Accelerators, Spectrometers, Detectors and Associated Equipment*, 388(1-
3130 2):149–172, mar 1997.
- 3131 [55] F. Binon et al. Scattering of negative pions on carbon. *Nuclear Physics B*,
3132 17(1):168 – 188, 1970.
- 3133 [56] L. Aliaga et al. Minerva neutrino detector response measured with test beam
3134 data. *Nuclear Instruments and Methods in Physics Research Section A: Ac-*
3135 *celerators, Spectrometers, Detectors and Associated Equipment*, 789:28 – 42,
3136 2015.
- 3137 [57] M Adamowski et al. The liquid argon purity demonstrator. *Journal of Instru-*
3138 *mentation*, 9(07):P07005, 2014.
- 3139 [58] P. Vilain et al. Coherent single charged pion production by neutrinos. *Physics*
3140 *Letters B*, 313(1-2):267–275, aug 1993.
- 3141 [59] R. Acciarri et al. Convolutional neural networks applied to neutrino events
3142 in a liquid argon time projection chamber. *Journal of Instrumentation*,
3143 12(03):P03011, 2017.
- 3144 [60] R. Acciarri et al. Design and construction of the MicroBooNE detector. *Journal*
3145 *of Instrumentation*, 12(02):P02017–P02017, feb 2017.

- 3146 [61] C. E. Aalseth et al.l. DarkSide-20k: A 20 tonne two-phase LAr TPC for direct
3147 dark matter detection at LNGS. *The European Physical Journal Plus*, 133(3),
3148 mar 2018.
- 3149 [62] H Fenker. Standard beam pwc for fermilab. Technical report, Fermi National
3150 Accelerator Lab., Batavia, IL (USA), 1983.
- 3151 [63] H Fesbach. Theoretical nuclear physics: Nuclear reactions. 1992.
- 3152 [64] J. A. Formaggio and G. P. Zeller. From ev to eev: Neutrino cross sections across
3153 energy scales. *Rev. Mod. Phys.*, 84:1307–1341, Sep 2012.
- 3154 [65] E. Friedman et al. K+ nucleus reaction and total cross-sections: New analysis
3155 of transmission experiments. *Phys. Rev.*, C55:1304–1311, 1997.
- 3156 [66] V.M. Gehman, S.R. Seibert, K. Rielage, A. Hime, Y. Sun, D.-M. Mei,
3157 J. Maassen, and D. Moore. Fluorescence efficiency and visible re-emission
3158 spectrum of tetraphenyl butadiene films at extreme ultraviolet wavelengths.
3159 *Nuclear Instruments and Methods in Physics Research Section A: Accelerators,*
3160 *Spectrometers, Detectors and Associated Equipment*, 654(1):116 – 121, 2011.
- 3161 [67] H. Geiger and E. Marsden. On a diffuse reflection of the formula-particles.
3162 *Proceedings of the Royal Society A: Mathematical, Physical and Engineering*
3163 *Sciences*, 82(557):495–500, jul 1909.
- 3164 [68] Howard Georgi and S. L. Glashow. Unity of all elementary-particle forces. *Phys.*
3165 *Rev. Lett.*, 32:438–441, Feb 1974.
- 3166 [69] D.Y. Wong (editor) G.L. Shaw (Editor). *Pion-nucleon Scattering*. John Wiley
3167 & Sons Inc, 1969.
- 3168 [70] Glassman High Voltage, Inc., Precision Regulated High Voltage DC Power Sup-
3169 ply.

- 3170 [71] D S Gorbunov. Sterile neutrinos and their role in particle physics and cosmology.
3171 *Physics-Uspekhi*, 57(5):503, 2014.
- 3172 [72] C. Green, J. Kowalkowski, M. Paterno, M. Fischler, L. Garren, and Q. Lu. The
3173 Art Framework. *J. Phys. Conf. Ser.*, 396:022020, 2012.
- 3174 [73] S. Hansen, D. Jensen, G. Savage, E. Skup, and A. Soha. Fermilab test beam
3175 multi-wire proportional chamber tracking system upgrade. June 2014. Interna-
3176 tional Conference on Technology and Instrumentation in Particle Physics (TIPP
3177 2014).
- 3178 [74] J. Harada. Non-maximal θ_{23} , large θ_{13} and tri-bimaximal θ_{12} via quark-
3179 lepton complementarity at next-to-leading order. *EPL (Europhysics Letters)*,
3180 103(2):21001, 2013.
- 3181 [75] Peter W. Higgs. Broken symmetries and the masses of gauge bosons. *Physical*
3182 *Review Letters*, 13(16):508–509, oct 1964.
- 3183 [76] P.W. Higgs. Broken symmetries, massless particles and gauge fields. *Physics*
3184 *Letters*, 12(2):132–133, sep 1964.
- 3185 [77] H J Hilke. Time projection chambers. *Reports on Progress in Physics*,
3186 73(11):116201, 2010.
- 3187 [78] N. Ishida, M. Chen, T. Doke, K. Hasuike, A. Hitachi, M. Gaudreau, M. Kase,
3188 Y. Kawada, J. Kikuchi, T. Komiyama, K. Kuwahara, K. Masuda, H. Okada,
3189 Y.H. Qu, M. Suzuki, and T. Takahashi. Attenuation length measurements of
3190 scintillation light in liquid rare gases and their mixtures using an improved
3191 reflection suppresser. *Nuclear Instruments and Methods in Physics Research*
3192 *Section A: Accelerators, Spectrometers, Detectors and Associated Equipment*,
3193 384(2-3):380–386, jan 1997.

- 3194 [79] G. Pulliam J. Asaadi, E. Gramellini. Determination of the electron lifetime in
3195 lariat. Technical report, August 2017.
- 3196 [80] George Jaffé. Zur theorie der ionisation in kolonnen. *Annalen der Physik*,
3197 347(12):303–344, 1913.
- 3198 [81] C. Jarlskog. A basis independent formulation of the connection between quark
3199 mass matrices, CP violation and experiment. *Zeitschrift für Physik C Particles
3200 and Fields*, 29(3):491–497, sep 1985.
- 3201 [82] B J P Jones, C S Chiu, J M Conrad, C M Ignarra, T Katori, and M Toups. A
3202 measurement of the absorption of liquid argon scintillation light by dissolved ni-
3203 tragen at the part-per-million level. *Journal of Instrumentation*, 8(07):P07011,
3204 2013.
- 3205 [83] Benjamin J. P. Jones. *Sterile Neutrinos in Cold Climates*. PhD thesis, MIT,
3206 2015.
- 3207 [84] Cezary Juszczak, Jarosław A. Nowak, and Jan T. Sobczyk. Simulations from
3208 a new neutrino event generator. *Nuclear Physics B - Proceedings Supplements*,
3209 159:211–216, sep 2006.
- 3210 [85] D. I. Kazakov. Beyond the standard model: In search of supersymmetry. In
3211 *2000 European School of high-energy physics, Caramulo, Portugal, 20 Aug-2
3212 Sep 2000: Proceedings*, pages 125–199, 2000.
- 3213 [86] Dae-Gyu Lee, R. N. Mohapatra, M. K. Parida, and Merostar Rani. Predic-
3214 tions for the proton lifetime in minimal nonsupersymmetric $so(10)$ models: An
3215 update. *Phys. Rev. D*, 51:229–235, Jan 1995.

- 3216 [87] M A Leigui de Oliveira. Expression of Interest for a Full-Scale Detector Engi-
3217 neering Test and Test Beam Calibration of a Single-Phase LAr TPC. Technical
3218 Report CERN-SPSC-2014-027. SPSC-EOI-011, CERN, Geneva, Oct 2014.
- 3219 [88] W. H. Lippincott, K. J. Coakley, D. Gastler, A. Hime, E. Kearns, D. N. McK-
3220 insey, J. A. Nikkel, and L. C. Stonehill. Scintillation time dependence and pulse
3221 shape discrimination in liquid argon. *Phys. Rev. C*, 78:035801, Sep 2008.
- 3222 [89] Jorge L. Lopez and Dimitri V. Nanopoulos. Flipped SU(5): Origins and re-
3223 cent developments. In *15th Johns Hopkins Workshop on Current Problems*
3224 *in Particle Theory: Particle Physics from Underground to Heaven Baltimore,*
3225 *Maryland, August 26-28, 1991*, pages 277–297, 1991.
- 3226 [90] Vincent Lucas and Stuart Raby. Nucleon decay in a realistic so(10) susy gut.
3227 *Phys. Rev. D*, 55:6986–7009, Jun 1997.
- 3228 [91] Ettore Majorana. Teoria simmetrica dell'elettrone e del positrone. *Il Nuovo*
3229 *Cimento*, 14(4):171–184, apr 1937.
- 3230 [92] Hisakazu Minakata and Alexei Yu. Smirnov. Neutrino mixing and quark-lepton
3231 complementarity. *Phys. Rev. D*, 70:073009, Oct 2004.
- 3232 [93] M. Mooney. The microboone experiment and the impact of space charge effects.
3233 2015.
- 3234 [94] E. Morikawa, R. Reininger, P. Gürtler, V. Saile, and P. Laporte. Argon, kryp-
3235 ton, and xenon excimer luminescence: From the dilute gas to the condensed
3236 phase. *The Journal of Chemical Physics*, 91(3):1469–1477, aug 1989.
- 3237 [95] FM Newcomer, S Tedja, R Van Berg, J Van der Spiegel, and HH Williams.
3238 A fast, low power, amplifier-shaper-discriminator for high rate straw tracking
3239 systems. *IEEE Transactions on Nuclear Science*, 40(4):630–636, 1993.

- 3240 [96] Emmy Noether. Invariant variation problems. *Transport Theory and Statistical*
3241 *Physics*, 1(3):186–207, jan 1971.
- 3242 [97] I. Nutini. Study of charged particles interaction processes on ar in the 0.2 - 2.0
3243 GeV energy range through combined information from ionization free charge
3244 and scintillation light. Technical report, jan 2015.
- 3245 [98] D. R. Nygren. The time projection chamber: A new 4π detector for charged
3246 particles. Technical report, 1974.
- 3247 [99] L. Onsager. Initial recombination of ions. *Phys. Rev.*, 54:554–557, Oct 1938.
- 3248 [100] S. Pascoli, S.T. Petcov, and A. Riotto. Leptogenesis and low energy cp-violation
3249 in neutrino physics. *Nuclear Physics B*, 774(1):1 – 52, 2007.
- 3250 [101] C. Patrignani et al. Review of Particle Physics. *Chin. Phys.*, C40(10):100001,
3251 2016.
- 3252 [102] B. Pontecorvo. Neutrino Experiments and the Problem of Conservation of
3253 Leptonic Charge. *Sov. Phys. JETP*, 26:984–988, 1968. [Zh. Eksp. Teor.
3254 Fiz.53,1717(1967)].
- 3255 [103] T. Yang R. Acciarri. Investigation of the non-uniformity observed in the wire
3256 response to charge in lariat run 1. Technical report, February 2017.
- 3257 [104] T. Yang R. Acciarri, M. Stancari. Determination of the electron lifetime in
3258 lariat. Technical report, March 2016.
- 3259 [105] Martti Raidal. Relation between the neutrino and quark mixing angles and
3260 grand unification. *Phys. Rev. Lett.*, 93:161801, Oct 2004.
- 3261 [106] Steve Ritz et al. Building for Discovery: Strategic Plan for U.S. Particle Physics
3262 in the Global Context. 2014.

- 3263 [107] C. Rubbia. The Liquid Argon Time Projection Chamber: A New Concept for
3264 Neutrino Detectors. 1977.
- 3265 [108] L.M. Saunders. Electromagnetic production of pions from nuclei. *Nucl. Phys.*,
3266 *B7*: 293-310(1968).
- 3267 [109] Qaisar Shafi and Zurab Tavartkiladze. Neutrino democracy, fermion mass hier-
3268 archies, and proton decay from 5d su(5). *Phys. Rev. D*, 67:075007, Apr 2003.
- 3269 [110] Sigma-Aldrich, P.O. Box 14508, St. Louis, MO 63178 USA.
- 3270 [111] R. K. Teague and C. J. Pings. Refractive index and the lorentz–lorenz function
3271 for gaseous and liquid argon, including a study of the coexistence curve near the
3272 critical state. *The Journal of Chemical Physics*, 48(11):4973–4984, jun 1968.
- 3273 [112] J. Thomas and D. A. Imel. Recombination of electron-ion pairs in liquid argon
3274 and liquid xenon. *Phys. Rev. A*, 36:614–616, Jul 1987.
- 3275 [113] D.R.O. Morrison N. Rivoire V. Flaminio, W.G. Moorhead. Compilation of
3276 Cross Sections I: π^+ and π^- Induced Reactions. *CERN-HERA*, pages 83–01,
3277 1983.
- 3278 [114] D.R.O. Morrison N. Rivoire V. Flaminio, W.G. Moorhead. Compilation of
3279 Cross Sections II: K^+ and K^- Induced Reactions. *CERN-HERA*, pages 83–02,
3280 1983.
- 3281 [115] W. Walkowiak. Drift velocity of free electrons in liquid argon. *Nuclear Instru-*
3282 *ments and Methods in Physics Research Section A: Accelerators, Spectrometers,*
3283 *Detectors and Associated Equipment*, 449(1-2):288–294, jul 2000.
- 3284 [116] Hermann Weyl. Gravitation and the electron. *Proceedings of the National
3285 Academy of Sciences of the United States of America*, 15(4):323–334, 1929.

- 3286 [117] Colin et al Wilkin. A comparison of pi+ and pi- total cross-sections of light
3287 nuclei near the 3-3 resonance. *Nucl. Phys.*, B62:61–85, 1973.
- 3288 [118] D. H. Wright and M. H. Kelsey. The Geant4 Bertini Cascade. *Nucl. Instrum.*
3289 *Meth.*, A804:175–188, 2015.
- 3290 [119] C. S. Wu, E. Ambler, R. W. Hayward, D. D. Hoppes, and R. P. Hudson.
3291 Experimental test of parity conservation in beta decay. *Phys. Rev.*, 105:1413–
3292 1415, Feb 1957.
- 3293 [120] N Yahlali, L M P Fernandes, K Gonzlez, A N C Garcia, and A Soriano. Imaging
3294 with sipms in noble-gas detectors. *Journal of Instrumentation*, 8(01):C01003,
3295 2013.
- 3296 [121] T. Yanagida. Horizontal symmetry and masses of neutrinos. *Progress of Theo-*
3297 *retical Physics*, 64(3):1103–1105, sep 1980.